NONINVASIVE DETERMINATION OF TISSUE PARAMETERS IN MAGNETIC RESONANCE GUIDED HIGH INTENSITY FOCUSED ULTRASOUND FOR BREAST CANCER THERAPY

by

Yi Wang

A dissertation submitted to the faculty of
The University of Utah
in partial fulfillment of the requirements for the degree of

Doctor of Philosophy

Department of Bioengineering

The University of Utah

December 2014

The University of Utah Graduate School

STATEMENT OF DISSERTATION APPROVAL

The dissertation of **Yi Wang**

has been approved by the following supervisory committee members:

Dennis L. Parker	, Chair	**June 13, 2014** Date Approved
Douglas A. Christensen	, Member	**June 13, 2014** Date Approved
Edward DiBella	, Member	**June 13, 2014** Date Approved
Glen Morrell	, Member	**June 17, 2014** Date Approved
Yan-Ting Shiu	, Member	**June 17, 2014** Date Approved
Edward Hsu	, Member	**June 17, 2014** Date Approved

And by **Patrick A. Tresco**, Chair of

the Department of **Bioengineering**

and by David B. Kieda, Dean of the The Graduate School.

ABSTRACT

Magnetic resonance guided high intensity focused ultrasound (MRgHIFU) is a promising minimal invasive thermal therapy for the treatment of breast cancer. This study develops techniques for determining the tissue parameters — tissue types and perfusion rate — that influence the local temperature during HIFU thermotherapy procedures.

For optimal treatment planning for each individual patient, a 3D volumetric breast tissue segmentation scheme based on the hierarchical support vector machine (SVM) algorithm was developed to automatically segment breast tissues into fat, fibroglandular tissue, skin and lesions. Compared with fuzzy c-mean and conventional SVM algorithm, the presented technique offers tissue classification performance with the highest accuracy. The consistency of the segmentation results along both the sagittal and axial orientations indicates the stability of the proposed segmentation routine. Accurate knowledge of the internal anatomy of the breast can be utilized in the ultrasound beam simulation for the treatment planning of MRgHIFU therapy.

Completely noninvasive MRI techniques were developed for visualizing blood vessels and determining perfusion rate to assist in the MRgHIFU therapy. Two-point Dixon fat-water separation was achieved using a 3D dual-echo SSFP sequence for breast vessel imaging. The performances of the fat-water separation with various readout gradient designs were evaluated on a water-oil phantom, *ex vivo* pork sample and *in vivo* breast imaging. Results suggested that using a dual-echo SSFP readout with bipolar readout gradient polarity, blood vasculature could be successfully visualized through the thin-slab maximum intensity projection SSFP water-only images.

For determining the perfusion rate, we presented a novel imaging pulse sequence design consisting of a single arterial spin labeling (ASL) magnetization preparation followed by Look-Locker-like image readouts. This flow quantification technique was examined through simulation, *in vitro* and *in vivo* experiments. Experimental results from a hemodialyzer when fitted with a Bloch-equation-based model provide flow measurements that are consistent with ground truth velocities.

With these tissue properties, it is possible to compensate for the dissipative effects of the flowing blood and ultimately improve the efficacy of the MRgHIFU therapies. Complete noninvasiveness of these techniques allows multiple measurements before, during and after the treatment, without the limitation of washout of the injected contrast agent.

To my family, Feiyue, Eliana and to my parents, Jinhua and Jianguo.

TABLE OF CONTENTS

ABSTRACT iii

LIST OF TABLES ix

ACKNOWLEDGEMENTS x

CHAPTERS

1. INTRODUCTION 1

- Purpose of this dissertation 1
- Overview of this dissertation 4

2. MAGNETIC RESONANCE IMAGING 7

- Introduction 7
- NMR spin system 8
- MR signal formation 11
  - B_0 field 11
  - RF excitation 13
  - Relaxation 15
  - Bloch equation 16
- Signal acquisition 19
  - Detection 19
  - Signal localization 21
- Imaging sequences 22
  - Gradient echo 22
  - Spoiled GRE 24
  - Balanced steady state free precession 26
- Inflow effect 27
- Arterial spin labeling 28

3. 3D MULTIPARAMETRIC BREAST MRI SEGMENTATION USING HIERARCHICAL SUPPORT VECTOR MACHINE WITH COIL SENSITIVITY CORRECTION 40

- Introduction 40

Materials and methods 44
  Subjects and image acquisition 44
  Preprocessing 44
  Tissue segmentation using hierarchical SVM 48
  Statistical analysis 50
Results 51
Discussion 53
Conclusions 56

4. FLOW MEASUREMENT IN MRI USING ARTERIAL SPIN LABELING WITH CUMULATIVE READOUT PULSES – THEORY AND VALIDATION 66

Introduction 66
Theory 70
  Imaging sequence 70
  Modeling 72
Methods 74
  Simulations 74
  Hemodialyzer imaging 75
  In vivo imaging 76
Results 77
  Simulation 77
  Hemodialyzer imaging 78
  In vivo imaging 80
Discussion 81
Conclusions 84

5. BREAST MR ANGIOGRAPHY USING TWO-POINT DIXON SSFP 92

Introduction 92
Theory 94
  Two-point Dixon fat-water separation 94
  Bipolar readout gradient 97
  TR/TE selection 97
Methods 98
  Pulse sequence design 98
  Simulations 99
  Phantom imaging 100
  Ex vivo pork imaging 100
  In vivo imaging 101
Results 101
  Simulations 101
  Phantom imaging 102
  Ex vivo imaging 104
  In vivo imaging 105
Discussion 107

Summary 109

6. CONCLUSION 137

Scientific contributions 137
Future work 139

REFERENCES 141

LIST OF TABLES

2. 1 NMR properties of nuclei used in MR imaging and spectroscopy 39

3.1 Overlap ratios of various algorithms with radiologist's manual classification as ground truth 63

3.2 Tissue type analysis of dataset #1 segmentation from Radiologist #1 63

3.3 Tissue type analysis of dataset #1 segmentation from Radiologist #2 64

3.4. Tissue type analysis of segmentation for dataset #2 64

3.5. Tissue type analysis of segmentation for dataset #3 64

3.6. Tissue type analysis of segmentation for dataset #4 65

3.7. Overlap ratios of hierarchical SVM at two orientations (sagittal and axial) for each individual tissue type 65

4. 1 Flow velocity estimation 91

ACKNOWLEDGEMENTS

I would like to thank the members of my committee, Dennis Parker, Douglas Christensen, Edward DiBella, Glen Morrell, Edward Hsu and Yan-Ting Shiu for their guidance which allowed me to expand my research potential.

I thank my co-authors, Edward DiBella, Glen Morrell, Seong-Eun Kim, Marta Heibrun, Allison Payne, and Dennis Parker for their helpful suggestions and contributions for this research.

I would like to express many thanks to the students and staff at Utah Center for Advanced Imaging Research (UCAIR).

Finally, I express thanks to my family, Feiyue, Eliana and my parents, Jianguo and Jinhua who supported me in my Ph.D. study.

CHAPTER 1

INTRODUCTION

Purpose of this dissertation

Breast cancer is the most common cancer among women. About one in eight women in America will develop breast cancer during her lifetime (1). Due to early detection and improved treatment, the death rate from breast cancer has dropped over the past two decades. Studies have been shown the curative breast-conserving therapy offers an equivalent therapeutic effect compared with radical mastectomy (2).

Magnetic resonance-guided high intensity focused ultrasound (MRgHIFU) is a promising procedure that may eventually play an important role in minimal invasive thermal therapy for breast cancer treatment. In the HIFU procedure, a focused ultrasound beam is applied to destroy tumors without damaging the surrounding healthy tissue and skin, therefore providing excellent cosmetic outcomes and reducing surgery recovery time. With the guidance of magnetic resonance imaging (MRI), it allows clear delineation of tumor margin and the control of the temperature in the noninvasive thermal therapy.

This dissertation focuses on developing novel MR image acquisition schemas and image processing algorithms for determining tissue parameters that can assist in MRgHIFU therapy. Segmented tissue models with accurate anatomical distribution information are attained using a supervised classification algorithm. Moreover, various pulse sequence designs are presented to visualize blood vasculature and estimate the blood perfusion rate.

Calculation of the acoustic parameters of the ultrasound sonication to completely ablate the target tissue volume is an important pretreatment planning step in MRgHIFU procedures. Since the variation of the thermal and acoustic properties between different tissue types affects both the simulated ultrasound beam pattern and the resulting thermal models, it is essential to not only know the distribution of the lesion to be treated, but also the acoustic and thermal properties of the tissue along the proposed ultrasound trajectory. Previous studies of MRgHIFU for breast cancer utilize manual drawing of the target lesion volume based on a single or multiple slices of T_1-weighted fast flow angle shot (FLASH) (3) or T_2-weighted turbo spin echo (TSE) images (4) for pretreatment planning. The resulting hand-drawn information was then used to calculate the ultrasound acoustic parameters of the ultrasound sonication, where error can be easily introduced due to manual classification of localized target volume with a limited number of image slices and single image contrast. Several algorithms have been proposed for breast MRI segmentation (5-7), mostly focusing on localized regions (8) or certain specific tissue types (9). However, a complete volumetric breast MRI segmentation algorithm was not available but could be very helpful in interventional thermal treatments for breast cancer, which require accurate knowledge of the internal anatomy of the breast. This motivated the first project of my dissertation work, which was aimed at developing a 3D volumetric breast tissue segmentation algorithm. The algorithm does not require additional manual intervention other than giving the training data by identifying each tissue type on a training dataset. In addition to treatment planning, the proposed tissue classification technique can also be applied in MRgHIFU therapy monitoring and posttreatment evaluation.

To achieve accurate temperature evolution, precise physical modeling of heat transfer should take into account the tissue-dependent perfusion rate and the individually different structures of the vascular system. The objective of MRgHIFU therapies is to induce sufficient heating on pathological tissue while preserving surrounding healthy tissue (10). The therapeutic objective of thermal therapies can be compromised due to the dissipative effects of tissue perfusion and blood vessels. For example, tumors with higher perfusion rates result in increased heat evacuation and rapid cooling of the target tissue. This can reduce the maximal temperature increase achievable for a given deposited energy and thus results in smaller ablation zones, reducing the efficiency of the therapeutic procedure. Similarly, when the procedure is performed in the proximity of large blood vessels, convective cooling can lead to substantially different outcomes compared to tissue without large-scale flow (11). These tissue-dependent properties play an important role in temperature distribution in thermal therapies. Several methods have been proposed to estimate tissue perfusion and image breast vasculature. Positron emission tomography (PET) was used to monitor breast tumor perfusion (12,13). Tumor vascular structure has been demonstrated with digital subtraction angiography (DSA) technique (14). Estimation of the breast perfusion and vasculature imaging have been performed using dynamic contrast enhanced (DCE)-MRI (13,15). Image contrast generated from these techniques relies on either injection of the contrast agent or the use of radioisotopes. Specifically, DCE-MRI has been utilized in treatment evaluation in MRgHIFU therapy (3,4,16); however, due to unknown properties of contrast agent in the presence of ultrasound, a contrast-agent-free method would be more appropriate, especially for monitoring blood flow during MRgHIFU treatment. Therefore, in the second project of my dissertation work, MRI techniques without injecting contrast agent were developed for visualization of blood vessels in the breast and quantification of tissue perfusion to assist in MRgHIFU therapy. Compared to techniques that involve external injection of either contrast agent or radioisotopes, the developed contrast-agent-free methods do not cause allergic reactions, are much cheaper to implement, and permit repetitive measurements without limitation by the washout of the contrast agent, which is favorable in clinical examination.

Overview of this dissertation

This dissertation is composed of six chapters, including this introductory chapter. The basic principles of MRI are reviewed in Chapter 2, where detailed discussion of MR data acquisition and some commonly used fast imaging sequence, e.g., gradient echo (GRE) and steady-state free precession (SSFP) sequences are presented. Theories on multipoint Dixon fat-water separation and quantitative flow imaging are also discussed. These MR principles lay the foundation for the advanced techniques described in Chapters 3–5.

In Chapter 3, a hierarchical support vector machine (SVM) algorithm is presented to achieve accurate 3D breast MRI segmentation. The hierarchical SVM decomposes a multiclass classification problem into multiple binary-classifiers. Taking advantage of the multiparametric MRI image contrasts and a series of preprocessing procedures, superior segmentation accuracy has been demonstrated using the presented technique, compared to that from the conventional SVM and Fuzzy c-mean (FCM) algorithms. This work has been published in *Academic Radiology*. 2013, 20(2): 137–47 and is entitled "3D Multi-parametric breast MRI segmentation using hierarchical support vector machine with coil sensitivity correction" (17).

Chapter 4 presents an arterial spin labeling (ASL) based sequence design with Look-Locker-like (18) image readouts for visualizing blood vasculature and quantifying blood flow. This technique is systematically examined through theoretical simulation, *in vitro* and *in vivo* experiment. Bloch-equation-based modeling has been developed and validated using a hemodialyzer as a tissue-mimicking flow phantom. This chapter is based on the 2009 International Society of Magnetic Resonance in Medicine (ISMRM) presentation entitled "High resolution 3D MR angiography using arterial spin labeling" (19), and a paper published in *Medical Physics*. 2010, 37(11): 5801–5810, under the title of "Flow measurement in MRI using arterial spin labeling with cumulative readout pulses — theory and validation" (20).

In Chapter 5, a 3D dual-echo SSFP sequence featured with alternating bipolar readout polarity is described for breast magnetic resonance angiography (MRA) imaging. This contrast-agent-free technique allows accurate separation of the fat-only and water-only images by properly combing the in-phase and out-of-phase source images from adjacent repetition time (TR). Signal behaviors of the in-phase and out-of-phase image are simulated for both fat and fibroglandular tissue. The optimized imaging parameters are then used in the phantom, *ex vivo* and *in vivo* experiments. The breast vasculature information can be obtained from the resulting water-only images. This chapter is partially based on the 2012 ISMRM presentation entitled "Two-point Dixon fat and water separation using dual-echo SSFP sequence in breast imaging” (21).

Finally, conclusions are given in Chapter 6 summarizing the accomplishments and limitations of this dissertation, followed by suggestions for future work.

CHAPTER 2

MAGNETIC RESONANCE IMAGING

Introduction

Magnetic resonance imaging (MRI) is a tomographic imaging technique that detects the internal physical information based on signals acquired externally. In 1946, nuclear magnetic resonance (NMR) phenomenon was independently reported by both Edward Purcell (22) and Felix Bloch (23), and the researchers were awarded the Nobel Prize in 1952 for their work. After this discovery, magnetic resonance spectroscopy (MRS) quickly gained popularity because of its ability to obtain information about the chemical composition and physical structures of matter. Paul Lauterbur reported the first 2D MR image with spatial information encoding in 1973 (24). In his experiment, a magnetic field gradient, a weak magnetic field changing as a function of position, was superimposed on a stronger magnetic field to encode the physical position of nuclei within the imaged object. The spatial variation in the magnetic field causes a corresponding variation in the nuclear resonance frequency. Consequently, spatial information can be obtained from the spectral analysis of the NRM signals. In 1991, Richard Ernst (25) was granted the Nobel Prize of chemistry for his contributions in the development of pulsed NMR and MRI techniques. Following these major developments, NMR saw a rapid growth in various fields, especially in clinical applications after the 1980s. The development of NMR went from a purely experimental laboratory phase to become a widely recognized clinical diagnostic imaging tool. Its success resides in its ability to generate high resolution images with structural, metabolic, and functional information.

In this chapter, the fundamental theory of MRI is explained. Principles of an MRI system are presented from a NMR spin system, MR signal formation and reception perspectives. The associated hardware components including main magnetic field, radiofrequency (RF) field and gradient field are also described.

NMR spin system

The formation of an MRI signal could be traced down to the atomic level characterized by the quantum mechanics. Nuclei with nonzero spin numbers possess an angular momentum *J*, often called spin. An ensemble of spins forms a spin system in MRI. The angular momentum J is related to the magnetic moment $\vec{\mu}$ of nuclei by

$$\vec{\mu} = \gamma \vec{J} \qquad [2.1]$$

where γ is the gyromagnetic ratio, a constant for each type of nucleus. For example, $\bar{\gamma} = \frac{\gamma}{2\pi}$ of ^{1}H is 42.58 MHz/T. ^{1}H, the most abundant nucleus in the human body, has an atomic number of 1/2. Such a spin system is called a spin-half system. In addition to hydrogen ^{1}H, other nuclei such as ^{3}He, ^{13}C, ^{17}O, ^{19}F, ^{23}Na, ^{31}P can also be used for MR imaging and spectroscopy. Nuclear magnetic resonance (NMR) properties of these nuclei, including gyromagnetic ratio, resonance frequency, natural abundance and relative sensitivity, are listed in Table 2.1. The high abundance of ^{1}H leads to its prevalent utility in generating MRI signals clinically.

In the absence of an external magnetic field, the nuclear magnetic moments $\vec{\mu}$ are randomly oriented which results in a zero net magnetic field. When the nuclei are placed in a strong external magnetic field B_0, spins in different orientations relative to the B_0 direction will have different energy of interaction with the external magnetic field, referred as B_0 direction. According to the quantum theory,

$$E = -\vec{\mu} \cdot \vec{B}_0 = -\gamma \hbar m_I B_0 \qquad [2.2]$$

where m_I is the magnetic quantum number. For a spin-half system, two energy levels exist, i.e., for pointing-up spins ($m_I = \frac{1}{2}$),

$$E_\uparrow = -\frac{1}{2}\gamma \hbar B_0 \qquad [2.3]$$

and for pointing-down spins ($m_I = -\frac{1}{2}$),

$$E_\downarrow = \frac{1}{2}\gamma \hbar B_0 \qquad [2.4]$$

The Zeeman splitting of the energy level is illustrated in Fig. 2.1. The energy difference between the two spin states is

$$\Delta E = E_{\downarrow} - E_{\uparrow} = \gamma \hbar B_0 \qquad [2.5]$$

where $\hbar$ is the Plank's constant divided by 2π. The energy $E_{\uparrow}$ and $E_{\downarrow}$ represent the lower-energy and the higher-energy states for the spin-up and spin-down state, respectively (26). According to the Boltzmann relationship, the spin population difference between the two energy levels can be expressed as

$$\frac{N_{\uparrow}}{N_{\downarrow}} = \exp\left(\frac{\Delta E}{KT_s}\right) \qquad [2.6]$$

where K=1.38×10^{-23} J/K is Boltzmann constant, T_s is the absolute temperature of the spin system. A bulk magnetization $\vec{M}$ reflecting the collective behavior of a spin system can be defined as

$$\vec{M} = \sum_{n=1}^{N_s} \vec{\mu}_n \qquad [2.7]$$

where N_s is the total number of spins. The magnitude of the bulk magnetization for a spin-half system with two spin states is

$$\left|\vec{M}\right| = \frac{\gamma^2 \hbar^2 B_0 N_s}{4KT_s} \qquad [2.8]$$

It is apparent that the magnitude of the bulk magnetization is proportional to the strength of the main magnetic field and the absolute temperature. Since temperature in a living system cannot usually be changed dramatically, the magnitude of the main magnetic field thus becomes a key factor affecting the bulk magnetization.

MR signal formation

B_0 field

The main magnetic field B_0 is one of the key components for any MRI system. Ranging from 0.1–11T, the magnets can be resistive, permanent, or superconducting. These magnets are the most expensive part of an MR system and are used to generate the strong, uniform, and static main magnetic field. Classically, the motion of the moment vector $\vec{\mu}$ of the spins could be described by the equation of motion

$$\frac{d\vec{\mu}}{dt} = \gamma\vec{\mu} \times B_0\vec{k} \qquad [2.9]$$

when assuming the B_0 field is applied in the z-direction $\vec{k}$. Solving the equation, the following magnetic moments are obtained

$$\begin{aligned} \mu_{xy}(t) &= \mu_{xy}(0)e^{-i\gamma B_0 t} \\ \mu_z(t) &= \mu_z(0) \end{aligned} \qquad [2.10]$$

indicating that the nuclear spins precess around the main magnetic field, i.e., the direction of the B_0 field. The process is called precession, as illustrated in Fig. 2.2. The angular precession frequency ω is called the Larmor frequency. It is related to the main B_0 field by the relationship

$$\omega = \gamma B_0 \qquad [2.11]$$

Since the gyromagnetic ratio γ is nuclei dependent, different nuclei precesses at different frequencies in a given B_0 field.

Ideally, the B_0 field should have a constant magnetic field throughout the whole imaging volume. However, two factors can contribute to field inhomogeneity — susceptibility-induced field variation and the chemical shift. Different bulk magnetic susceptibility within the sample can cause B_0 variation. This sample-induced field inhomogeneity depends on the susceptibility difference and the geometry of the object being imaged. The resultant inhomogeneity is most severe near the boundaries between two materials with distinct susceptibilities (26). The imperfection of the field can be partially alleviated by applying shimming, where spatially varying field patterns are generated by a set of shim coils to compensate for the field inhomogeneity.

Due to the high abundance of ^{1}H, signals from hydrogen nuclei residing on water molecules and fat molecules are the major sources of signal contribution in MRI. Because different shielding of the nuclei created by the orbital motion of the surrounding electrons in response to the main B_0 field, protons attached to water and fat resonate at slightly different frequencies. This displacement of the resonance frequency is called the chemical shift, and can be expressed the following relationship

$$\omega = \omega_0(1-\sigma) \qquad [2.12]$$

where σ is the shielding constant that is dependent on the chemical environment. An example of the ^{1}H NMR spectrum is demonstrated in Fig. 2.3, with horizontal axis being the resonant frequency presented in parts per million (ppm). The spectrum peaks appear at different frequencies corresponding to different chemical shifts. In Fig. 2.3, it is shown that the fat peak is shifted downfield by approximately 3.5 ppm relative to the water peak. At B_0 = 3T, the chemical shift frequency difference between fat and water, Δf_{cs}, is around 420 Hz. To achieve the desired image contrast, fat signal usually needs to be either suppressed or separated from the water signal. Details on the fat suppression/separation techniques are reviewed in Chapter 5.

RF excitation

Spins precess around the longitudinal axis, as described in Eq. [2.10]. The ensemble of magnetic moments μ_z forms the longitudinal magnetization, directly related to B_0, whereas the net in-plane moment μ_{xy} is zero at thermal equilibrium because the spins are randomly distributed in the *x*-*y* plane with random phases. In order to collect signal from the transverse plane, an additional field B_1, also referred as RF pulse, is required to establish phase coherence among the spins.

According to the Planck's Law, electromagnetic radiation of frequency, ω_{rf}, carries energy

$$E_{rf} = \hbar\omega_{rf} \qquad [2.13]$$

In quantum mechanics, to induce a coherent transition of spins from one energy state to another, the quanta of energy provided by the field must be equal to the energy difference between the adjacent spin states (26),

$$E_{rf} = \Delta E = \gamma\hbar B_0 \qquad [2.14]$$

Referring to Eq. [2.12], we have

$$\omega_{rf} = \omega_0 \qquad [2.15]$$

indicating that the B_1 field rotates at the Larmor frequency. This condition is known as the resonance condition. Generally, B_1 field oscillates in the RF range and its amplitude is significantly smaller than the main magnetic field B_0. Typical form of the B_1 field can be written as

$$B_1(t) = B_1^e(t)e^{-i(\omega_{rf}t+\varphi)} \qquad [2.16]$$

where B_1^e is the envelope function, ω_{rf} is the excitation carrier frequency and φ is the initial phase. The spin is said to be on resonance when ω_{rf} is the same as the Larmor frequency ω_0.

The standard method to carry out an NMR experiment is to apply a short pulse of RF field at the Larmor frequency. The RF pulse is characterized by the flip angle (FA) — the angle between the direction of the main magnetic field and the magnetization vector immediately after the excitation pulse is terminated. For a small flip angle, the slice profile can be obtained by taking the Fourier transform of the temporal envelope of the RF pulses (27). The frequency range of the slice profile determines the bandwidth of the RF excitation pulses.

Relaxation

When a magnetization is perturbed from its equilibrium state by B_1 field, the magnetized spins tend to return to the equilibrium state. The recovery of magnetization along the *z*-direction and the decrease of the magnetization in the *x*-*y* plane are due to random thermal motion, and can be described by a longitudinal and a transverse relaxation, respectively. Experimentally, the governing equations of the bulk magnetization evolution over time are expressed as

$$\begin{aligned} \frac{dM_z}{dt} &= -\frac{M_z - M_z^0}{T_1} \\ \frac{dM_{xy}}{dt} &= -\frac{M_{xy}}{T_2} \end{aligned} \qquad [2.17]$$

Solving the equations, the bulk magnetization signal can be obtained

$$\begin{aligned} M_{xy}(t) &= M_{xy}(0_+)e^{-t/T_2} \\ M_z(t) &= M_z^0(1 - e^{-t/T_1}) + M_z(0_+)e^{-t/T_1} \end{aligned} \qquad [2.18]$$

where M_z^0 is the thermal equilibrium magnetization, $M_{xy}(0_+)$ and $M_z(0_+)$ are the magnetization in the transverse plane and along the longitudinal direction immediately after an RF pulse. The transverse magnetization, M_{xy}, decays exponentially and its signal is characterized by T_2 — the transverse or spin-spin relaxation time constant, see Fig. 2.4 (a). The longitudinal magnetization M_z exponentially recovers back to the equilibrium state and its signal is characterized by T_1 — the longitudinal or spin-lattice relaxation time constant, see Fig. 2.4 (b). T_1 is determined by the rate of energy transfer between the spin system and its surroundings.

The two relaxation times T_1, T_2, along with proton density (PD) are three essential parameters in MRI. The signal intensities result from a combination of the spin density, longitudinal and transverse relaxation times, and the parameters of the imaging sequence used. Changing the imaging parameters, such as TR, echo time (TE), and FA etc., different signal weightings are generated in the images. This makes MRI a very powerful imaging modality providing superior soft tissue contrasts compared to other imaging modalities.

Bloch equation

The equation that describes the interaction of the magnetization with the external magnetic field is commonly referred to as the Bloch equation (28),

$$\frac{d\vec{M}}{dt} = \gamma \vec{M} \times \vec{B} - \frac{M_x \vec{i} + M_y \vec{j}}{T_2} - \frac{(M_z - M_z^0)\vec{k}}{T_1} \qquad [2.19]$$

where $\vec{i}$, $\vec{j}$, and $\vec{k}$ are unit vectors along the x, y and z-axes, respectively, and M_z^0 is the magnetization at equilibrium.

The external fields include the static magnetic field B_0 along the z-axis and the time varying magnetic field B_1 which oscillates at the radiofrequency ω perpendicular to the main field, as given in Eq. [2.16]. The amplitude of the RF field is significantly smaller than the main magnetic field. Using this magnetic field combination, $B = B_1\cos(\omega_0 t)\vec{i} - B_1\sin(\omega_0 t)\vec{j} + B_0\vec{k}$, the Bloch equations can be rewritten as

$$\frac{dM_x}{dt} = \gamma(M_y B_0 + M_z B_1\sin(\omega_0 t)) - \frac{M_x}{T_2}$$

$$\frac{dM_y}{dt} = \gamma(-M_x B_0 + M_z B_1\cos(\omega_0 t)) - \frac{M_y}{T_2} \qquad [2.20]$$

$$\frac{dM_z}{dt} = -\gamma(M_x B_1\sin(\omega_0 t) + M_y B_1\cos(\omega_0 t)) - \frac{M_z - M_0}{T_1}$$

These equations can be simplified by adopting the rotating frame of reference — a coordinate system whose transverse plane rotates clockwise at the frequency of the B_1 field. In this rotating frame, the external field becomes

$$\vec{B}_{eff} = B_1\vec{i}' + (B_0 - \omega_{rf}/\gamma)\vec{k}' \qquad [2.21]$$

The unit directional vectors $\vec{i}'$, $\vec{j}'$ and $\vec{k}'$ in the rotating frame are related to that of the stationary frame by

$$\begin{aligned} \vec{i}' &= \cos(\omega t)\vec{i} - \sin(\omega t)\vec{j} \\ \vec{j}' &= \sin(\omega t)\vec{i} + \cos(\omega t)\vec{j} \\ \vec{k}' &= k' \end{aligned} \qquad [2.22]$$

When the frequency, ω_{rf}, of the oscillating RF field equals the Larmor frequency ω_0, called on resonance condition, Eq. [2.21] is simplified to

$$\vec{B}_{eff} = B_1\vec{i}\,' \qquad [2.23]$$

If the relaxation processes are negligible, the Bloch equations in the rotating frame can be written as

$$\begin{aligned} \frac{dM_{x'}}{dt} &= 0 \\ \frac{dM_{y'}}{dt} &= \gamma B_1 M_{z'} \\ \frac{dM_{z'}}{dt} &= -\gamma B_1 M_{y'} \end{aligned} \qquad [2.24]$$

Under the initial conditions of $M_{x'}(0) = M_{y'}(0) = 0$, and $M_{z'}(0) = M_{z'}^0$, the solutions to Eq. [2.24] in the rotating frame are

$$\begin{aligned} M_{x'}(t) &= 0 \\ M_{y'}(t) &= M_0 \sin(\omega_1 t) \\ M_{z'}(t) &= M_0 \cos(\omega_1 t) \end{aligned} \qquad [2.25]$$

Eq. [2.25] suggests that in the rotating frame, $\vec{M}$ precesses about the i' axis with the precession frequency $\omega_1 = \gamma B_1$ when an on-resonant RF pulse is applied along the *i’* axis.

Signal acquisition

Detection

To obtain a signal that can be processed, it is necessary to convert the rotating transverse magnetization into measurable signal. Precession of the magnetization $\vec{M}(\vec{r},t)$ induces a voltage in the RF receiver coil tuned at the Larmor frequency of the spin system. The receiver coil is used to detect the changes of the magnetization in the *x*-*y* plane, as illustrated in Fig. 2.5. The voltage signal $V(t)$ detected by the receiver coil is

$$V(t) = -\frac{\partial \Phi(t)}{\partial t} = -\frac{\partial}{\partial t}\int_{\text{object}} \vec{B}_r(\vec{r}) \cdot \vec{M}(\vec{r},t)d\vec{r} \qquad [2.26]$$

where $\Phi(t)$ is the magnetic flux through the coil, $\vec{B}_r(\vec{r})$ is the magnetic field at location $\vec{r}$. Using the vector decomposition $\vec{B}_r(\vec{r}) = B_{r,x}\vec{i} + B_{r,y}\vec{j} + B_{r,z}\vec{k}$, the voltage signal can be expressed as

$$V(t) = -\int_{\text{object}} \omega_0(\vec{r})\left|\vec{B}_{r,xy}(\vec{r})\right|\left|M_{xy}(\vec{r},0)\right|e^{-t/T_2(\vec{r})}\sin[-\omega_0(\vec{r})t + \phi_e(\vec{r}) - \phi_r(\vec{r})]d\vec{r} \qquad [2.27]$$

where $\omega_0(\vec{r})$ is the free precession frequency, $M_{xy}(\vec{r},0)$ is the transverse magnetization at time 0, $\phi_r(\vec{r})$ and $\phi_e(\vec{r})$ are the phase angles introduced by the receiver magnetic field and the RF excitation, respectively.

$V(t)$ is a high-frequency signal which rapidly oscillates with frequency ω_0. It can be demodulated by multiplying the voltage with a reference signal with frequency $\omega_0 + \delta\omega$. The high frequency component of the signal is then removed by applying a low-pass filter. Usually, $\delta\omega$ is very small and is referred to as the offset frequency from the Larmor frequency. The reference signal can be sinusoid or a cosinusoid, corresponding to detection of the rotating magnetization with two detectors orthogonal to each other. A quadrature detection of the signal demodulation process using two detectors is demonstrated in Fig. 2.6, and is called phase-sensitive detection (PSD). The two outputs are often combined together in a complex form, with one output being the real part and the other as the imaginary part of the signal. The detected complex signal after combining data from both channels is finally given by

$$s(t) = \omega_0 e^{-t/T_2(\vec{r})} \int_{\text{object}} B^*_{r,xy}(\vec{r}) M_{xy}(\vec{r},0) e^{-i\Delta\omega(\vec{r})t} d\vec{r} \qquad [2.28]$$

where $B^*_{r,xy}(\vec{r})$ is the complex conjugate of $B_{r,xy}(\vec{r})$, $M_{xy}(\vec{r},0) = |M_{xy}(\vec{r}\ ,0)| e^{i\phi_e(\vec{r})}$ and $B_{r,xy}(\vec{r}) = |B_{r,xy}(\vec{r})| e^{i\phi_r(\vec{r})}$. This signal is called the free induction decay (FID). Its amplitude is determined by the RF excitation pulses and the density of the spins presented in the object being imaged. The maximum amplitude of the received signal is achieved right at the time the FID is formed, and its amplitude decays exponentially with relaxation time T_2 in a homogeneous magnetic field. When field inhomogeneity presents, the decay rate is replaced by T_2^*, a faster rate due to the interactions of the spins with the inhomogeneous magnetic field (29).

$$\frac{1}{T_2^*} = \frac{1}{T_2} + \gamma \Delta B_0 \qquad [2.29]$$

Signal localization

A linearly varying field is added to the main field B_0 to make the *z*-component of the magnetic field vary spatially as

$$B(\vec{r}) = (B_0 + \vec{G} \cdot \vec{r})\vec{k} \qquad [2.30]$$

where $G = G_x\vec{i} + G_y\vec{j} + G_z\vec{k}$ stands for the gradient field spatially varying in all three directions. Because the frequency of the imaging nuclei is proportional to the field strength, the resonance frequency of the nuclei thus becomes a function of position *r*,

$$\omega(\vec{r}) = \gamma(B_0 + \vec{G} \cdot \vec{r}) = \omega_0 + \gamma \vec{G} \cdot \vec{r} \qquad [2.31]$$

Ignoring the relaxation effect, the FID signal after the excitation as given in Eq. [2.28] can subsequently be expressed as

$$S(t) = \int \rho(\vec{r}) e^{-i\omega_0 t} e^{-i\gamma \vec{G} \cdot \vec{r} t} d\vec{r} \qquad [2.32]$$

where $\rho(\vec{r}) \propto \omega_0 B^*_{r,xy}(\vec{r}) M_{xy}(\vec{r},0)$ is introduced as the effective spin density determined by the bulk magnetization. After passing through the PSD, the resulting low frequency signal becomes

$$S(t) = \int \rho(\vec{r}) e^{-i\gamma \vec{G}\cdot\vec{r}t} d\vec{r} \qquad [2.33]$$

A Fourier relationship can be established between the MR signal and the spin density by rewriting $S(t)$ as

$$S(t) = \int \rho(\vec{r}) e^{-i2\pi\vec{k}\cdot\vec{r}} d\vec{r} \qquad [2.34]$$

where $\vec{k} = \frac{\gamma \vec{G} t}{2\pi}$ is the position in the spatial frequency space, often called *k*-space. The signal can be interpreted as the Fourier transform of $\rho(\vec{r})$ at spatial frequency *k*, which is a function of the gradient field $\vec{G}$. The acquisition of MR signal therefore requires filling of the *k*-space.

Imaging sequences

Gradient echo

Gradient echo (GRE) is a type of signal frequently used in MRI. The echo is generated using time-varying gradient magnetic fields. Basic principle of the formation of the GRE is demonstrated through a timing diagram, shown in Fig. 2.7. Timing diagram is a graphic illustration of the waveforms of the gradients and the sequence of RF pulses, which are used to determine the manner in which *k*-space is scanned and the path of the *k*-space trajectory. First, a gradient G_z is applied concomitantly with the RF pulse to excite a 2D slice of an object. As demonstrated in Fig. 2.8, the location and the thickness of the slice to be excited can be determined by the RF pulse frequency and the slice-selective gradient G_z, according to the relationships

$$\begin{aligned} \omega &= \gamma G_z z \\ \Delta\omega &= \gamma G_z \Delta z \end{aligned} \qquad [2.35]$$

Assuming there is no local inhomogeneity, immediately after the imaging slice being excited with slice selection in the *z* direction, all the spins in the selected slice have the same precession frequency. Following a slice-selective excitation, a gradient G_y is turned on for a time interval τ_y. Spins along the *y*-direction will precess at a different frequency because of the different field strength experienced. Using Eq. [2.35], the accumulated phase of the spins after the time interval τ_y should be $\gamma G_y \tau_y y$. The application of the G_y gradient allows spatial phase encoding of spins, with the amount of phase encoding being determined by the amplitude of G_y and the interval τ_y. After the phase encoding, the frequency-encoding gradient G_x is applied to encode the *x* position of the spins. Preceding the readout gradient, a prephasing lobe of duration τ is applied during the phase encoding gradient to make sure the peak of the echo is formed at the center of the readout gradient. Specifically, after time interval τ, the phase dispersion caused by the gradient reaches a maximum. At this time the gradient is switched to its opposite polarity. During the second τ period, the application of the opposite gradient rephases the spins that were dephased during the first τ interval. The phase coherence is achieved when the amount of dephasing and rephasing are equal. The analog digital convertor (ADC) is turned on for a sampling period of 2τ to readout the GRE signal.

The play out of the RF pulses and the gradients in the slice selection, phase encoding and frequency encoding directions ensure the coverage of the *k*-space. MR signal performance and other complex contrasts can be obtained by more complicated pulse sequences with different imaging gradients, RF and imaging parameters.

The excitation pulse used in GRE is typically less than 90°, resulting in a small portion of the longitudinal magnetization being disturbed. Therefore the T_1 recovery of the longitudinal magnetization does not take long. As a result, GRE sequence is commonly used for rapid imaging with relatively short TR.

In a GRE sequence, the spins usually experience a series of identical excitation RF pulses, evenly spaced by TR. The magnetization is said to reach a dynamic equilibrium steady state when the magnetization reaches the same magnitude at the end of each TR. Steady state can be established in both longitudinal and transverse magnetization. Depending on whether the transverse magnetization component contributes to the steady state magnetization or not, the GRE sequence can be further classified into two categories — spoiled GRE and steady state free precession (SSFP).

Spoiled GRE

In spoiled GRE, both gradient spoiling and RF spoiling are employed to achieve spatially uniform crushing of the transverse magnetization. Applying the spoiling gradient and varying the phase of RF pulses effectively destroys the transverse magnetization before the next RF pulse — a key condition in the derivation of the spoiled GRE steady state signal expression. A schematic illustration of the longitudinal magnetization approaching the steady state in a spoiled GRE sequence is shown in Fig. 2.9. Assuming the longitudinal magnetization right before the nth α pulse is M_n^-. After the α pulse excitation, it becomes

$$M_n^+ = M_n^- \cos\alpha \qquad [2.36]$$

In the rest of the TR interval, the longitudinal magnetization experiences the T_1 relaxation

$$M_{n+1}^- = M_n^+ E_1 + M_0(1 - E_1) \qquad [2.37]$$

where $E_1 = e^{-TR/T_1}$. Substituting Eq. [2.36] into Eq. [2.37],

$$M_{n+1}^- = M_n^- E_1 \cos\alpha + M_0(1 - E_1) \qquad [2.38]$$

The condition of steady state is satisfied when the longitudinal components prior to the nth and $(n+1)$th pulses are equal, i.e., $M_{n+1}^- = M_n^- = M_{ss}$. Therefore, at steady state,

$$M_{ss} = M_{ss} E_1 \cos\alpha + M_0(1 - E_1) \qquad [2.39]$$

Solving the equation, the steady state signal M_{ss} becomes (26)

$$M_{ss} = \frac{M_0(1-E_1)}{1-E_1\cos\alpha} \qquad [2.40]$$

Balanced steady state free precession

Steady state free precession (SSFP) is another category of GRE sequence with steady states being established in both longitudinal and transverse magnetization. The formation of the SSFP signal requires the fixed gradient area on all three directions within each TR, in order to maintain the same phase accumulation by the transverse magnetization in each TR interval. This ensures the establishment of the transverse magnetization steady state. When a more stringent condition — the total zero gradient area on any axis during each TR — is met, as shown in Fig. 2.10, the balanced SSFP signal is formed. The transverse steady state signal $M_{\mathrm{SSFP}\perp}$ for the balanced SSFP can be expressed as (30)

$$M_{\mathrm{SSFP}\perp} = M_0 \sin\alpha \frac{1-E_1}{1-(E_1-E_2)\cos\alpha - E_1E_2} e^{-TR/T_2} \qquad [2.41]$$

where $E_2 = e^{-TR/T_2}$. TR used in the SSFP imaging is usually less than or on the order of T_2. For short *TR*, $E_1 \approx 1-TR/T_1$, and $E_2 \approx 1-TR/T_2$. Eq. [2.41] can thus be simplified to

$$M_{\mathrm{SSFP}\perp} = \frac{M_0 \sin\alpha}{(T_1/T_2)(1-\cos\alpha)+(1+\cos\alpha)} e^{-TR/T_2} \qquad [2.42]$$

when $\mathrm{TR} \ll T$. Because T_1/T_2 is in the denominator of the equation above, balanced SSFP signal is said to have T_2/T_1 contrast weighting. Fat and fluid oftentimes appear hyperintense in balanced SSFP images due to their high T_2/T_1 ratio. Additionally, the SSFP signal can suffer from artifacts caused by off-resonances. The phase accumulated during each *TR* in the presence of field inhomogeneity is

$$\phi = \gamma \Delta B_0 \cdot TR \qquad [2.43]$$

In voxels where this field inhomogeneity causes a π phase shift within a TR, the signal in the magnitude responses drops significantly. This signal loss appears as dark bands in the SSFP images, usually referred to as the banding artifacts. Since the off-resonances from susceptibilities are directly proportional to the field strength and *TR*, as shown in Eq. [2.43], SSFP imaging at higher field strength and longer TR tend to be affected more by the banding artifacts. Comparing with the spoiled GRE, balanced SSFP provides higher signal, but at the cost of reduced image contrast (27). SSFP is the base imaging sequence used in Chapter 5 for flow-independent breast MRA imaging.

Inflow effect

The inflow effect plays an important role in the flow-dependent MRA technique. High contrast between the inflowing blood and the background stationary tissue allows successful visualization of the blood vessels. Flow information encoded in the MR image can be uncovered using the GRE sequence with short *TR*. Specifically, an imaging slice with thickness *TH* can be modeled as *N* subslices, and *N* can be determined using the relation

$$N = \frac{TH}{v \cdot TR} \qquad [2.44]$$

where v is the flow velocity. As the flowing spins passing through the slice, flowing spins with different velocities sees different numbers of RF pulses. A schematic illustration of the inflow effect is given in Fig. 2.11, with the shaded area indicating the flowing spins. Fig. 2.11 (a) shows an example of an imaging slice composed of five sub-slices. After a TR, blood in the subslice *E* moves out of the imaging slice and is replaced by the incoming blood, see Fig. 2.11 (b). Similarly in Fig. 2.11 (c), fresh blood continues to enter the imaging slice, resulting in the replacement of the blood in the *D* subslice before the third RF excitation.

Hence, as image acquisition progresses, magnetizations of the spins in each sub-region are perturbed by different number of RF pulses due to the position and the speed of the flow. This provides a way to quantify the flow velocity, which is the topic of Chapter 4.

Arterial spin labeling

Perfusion is by definition the delivery of oxygen and nutrients to tissues through blood flow (31). Homeostasis and the survival of the organ depend heavily on perfusion.

Perfusion can be measured using MRI either by tracking the bolus of injected exogenous endovascular tracer, or taking the magnetically labeled water of arterial blood itself as endogenous tracer. The latter completely noninvasive approach is known as arterial spin labeling (ASL). Perfusion imaging using ASL has been demonstrated as biomarker in patients with acute stroke and chronic cerebrovascular disease (31).

Perfusion contrasts comes from the signal difference of two successively acquired images: one with (label image) and one without (control image) the labeling of the inflowing arterial water spins. The very first implementation of ASL was the continuous ASL (CASL) (32), where long RF (2–4 seconds) pulses and a slice-selective gradient were applied to adiabatically invert the arterial blood magnetization. Such implementation can potentially induce signal difference, reflecting the magnetization transfer (MT) effect, instead of perfusion. Even though a second local RF coil can be used to alleviate the MT effect, the complexity in implementation and limitation to single-slice imaging hinders the broad application of the CASL technique.

Another category of ASL technique is pulsed ASL (PASL), which labels the inflowing arterial blood with a much thicker inversion slab at a more proximal distance relative to the imaging volume. MT effect are counterbalanced between the label and control images through various designs of the labeling strategies, e.g., flow-sensitive alternating inversion recovery (FAIR), uninverted flow-sensitive alternating inversion recovery (UNFAIR), echo-planar imaging with signal targeting by alternating radiofrequency pulse (EPISTAR), proximal inversion with control of off-resonance effects (PICORE), etc. In general, MT effect is less prominent in PASL comparing to CASL because of the reduced RF power involved.

For absolute quantification of cerebral blood flow (CBF) using ASL, the Bloch equation for the longitudinal magnetization in the presence of perfusion can be modified to incorporate the magnetization exchange between static tissue and inflowing arterial blood:

$$\frac{dM}{dt} = \frac{M_0 - M}{T_1} + fM_b - \frac{f}{\lambda}M \qquad [2.45]$$

where M is the longitudinal magnetization of the tissue with an equilibrium value of M_0. M_b is the longitudinal magnetization of the inflowing arterial blood, f is the perfusion rate, and λ is the partition coefficient of water molecules between tissue and blood. Under the assumption of labeled water being completely and spontaneously extracted from the intravascular space as it enters the tissue, general solution for PASL can be written as:

$$\Delta M(t) = \begin{cases} 0 & 0 \le t < t_a \\ 2\alpha\left(\frac{M_0}{\lambda}\right)(t - t_a) f e^{-\frac{t}{T_{1b}}}\vartheta(t) & t_a \le t < t_a + \delta \\ 2\alpha\left(\frac{M_0}{\lambda}\right)\delta f e^{-\frac{t}{T_{1b}}}\vartheta(t) & t_a + \delta \le t \end{cases} \qquad [2.46]$$

where α is the labeling efficiency, t_a is the arrival time of the leading edge of the tagged spins, and $\vartheta(t)$ is a dimensionless term that depends on t_a, δ, T_1, and T_{1b}.

In a typical ASL experiment, about 1–2 second is required for the magnetically labeled blood to perfuse into the tissue. The resulting perfusion signal is only about 1% of the total tissue signal (33). This small percentage contributes to the intrinsic low signal-to-noise ratio (SNR) of ASL signals. Multiple measurements of the tagging and control images and signal averaging are thus commonly used to overcome the issue. Therefore, imaging sequence design with improved signal efficiency as presented in Chapter 4 is desirable, where images are acquired at multiple delay time after each arterial labeling magnetization preparation.

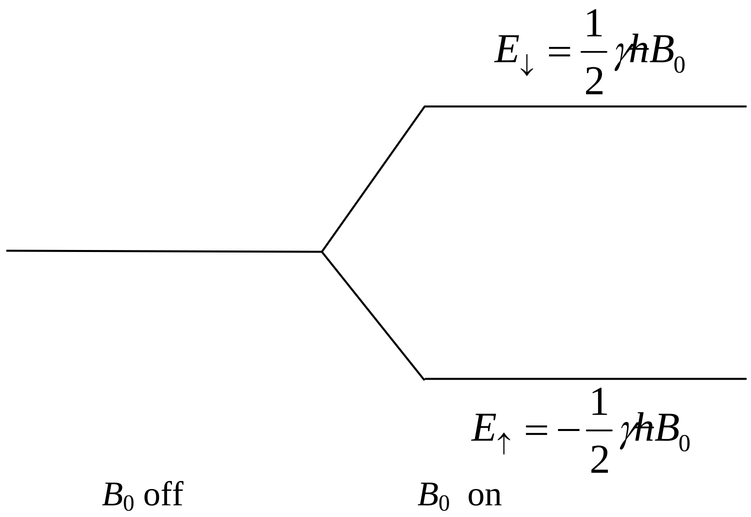

Figure 2.1. Zeeman splitting for a spin-half system in the B_0 field. $E_{\uparrow}$ and $E_{\downarrow}$ are the energy levels for spin up and spin down protons.

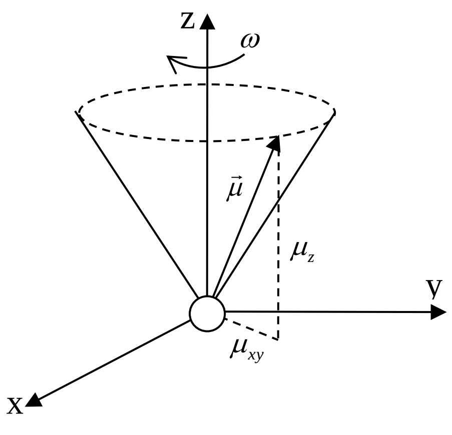

Figure 2.2. The clockwise precession of the magnetic moment vector about the direction of the main magnetic field B_0.

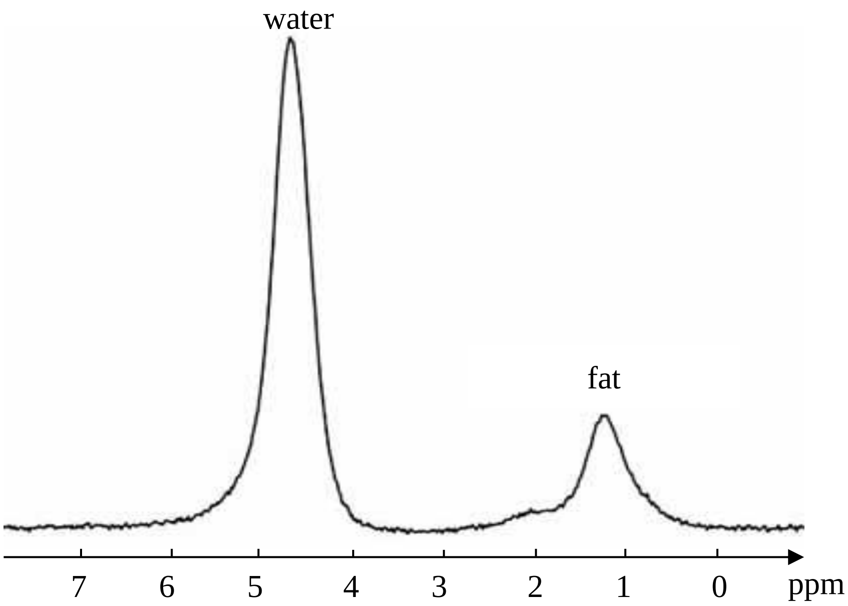

Figure 2.3. ^{1}H NMR spectrum.

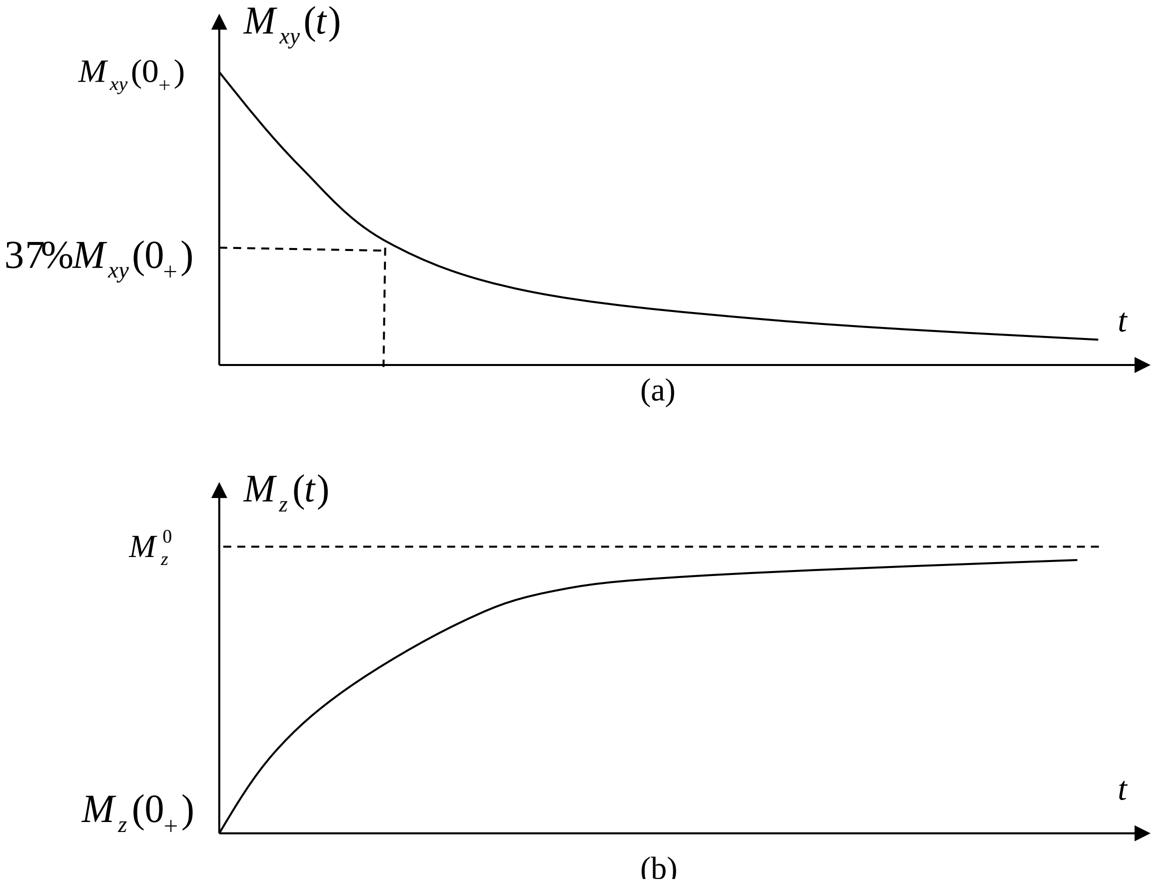

Figure 2.4. Relaxation of the transverse and longitudinal magnetization. (a) The exponential decay of the transverse magnetization characterized by T_2. (b) The recovery of the longitudinal magnetization characterized by T_1.

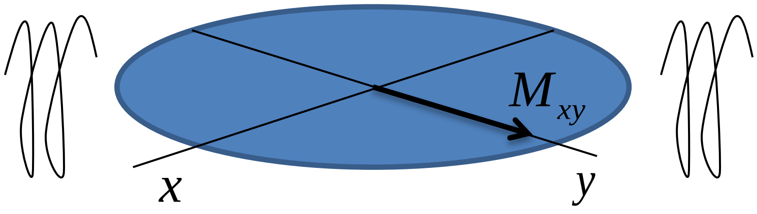

Figure 2.5. The rotating transverse magnetization $\vec{M}_{xy}$ induces an electromotive force signal in an RF receiver coil oriented to detect changes of magnetization in the x-y plane.

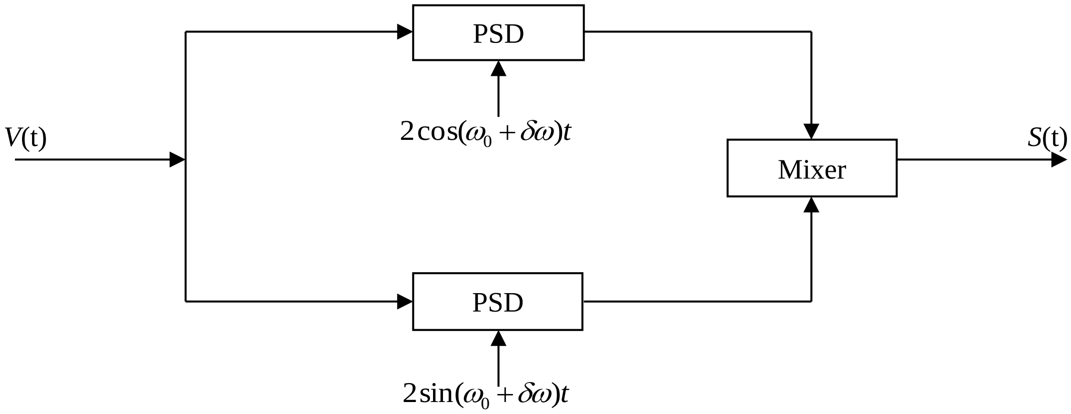

Figure 2.6. Phase senstivie detection.

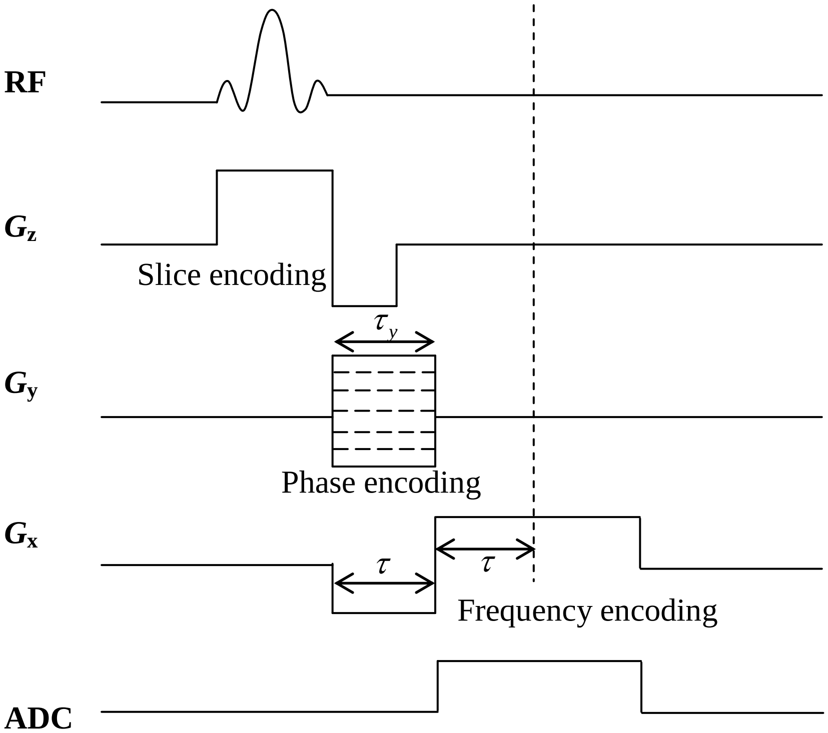

Figure 2.7. Timing diagram of a typical 2D GRE sequence.

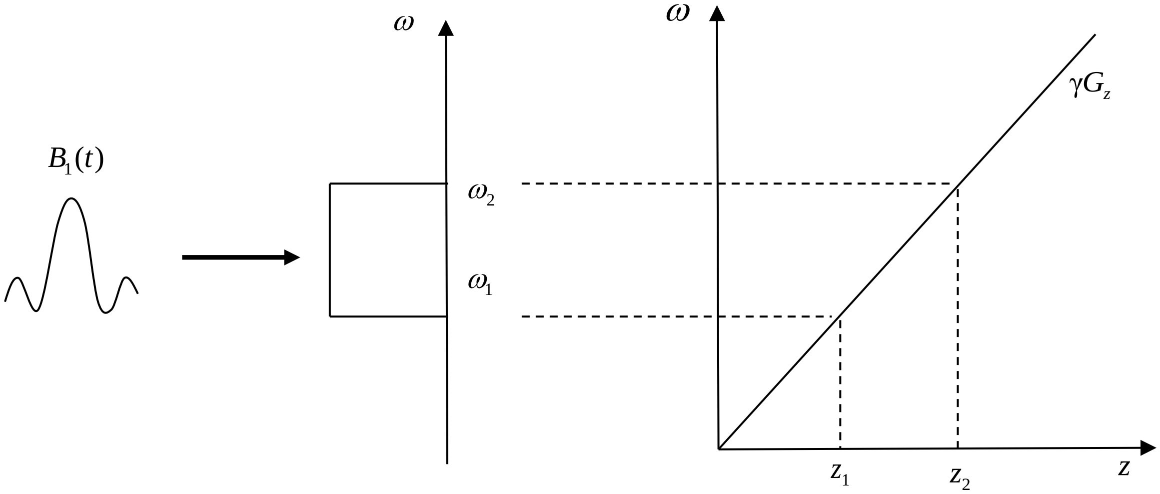

Figure 2.8. Slice selective excitation. Fourier transform of the envelope of B_1(t) leads to the slice profile of the RF pulse, with a bandwidth of $\omega_2 - \omega_1$. B_1(t) pulse selectively excite spins between z_1 and z_2 in the presence of slice-selective gradient G_z.

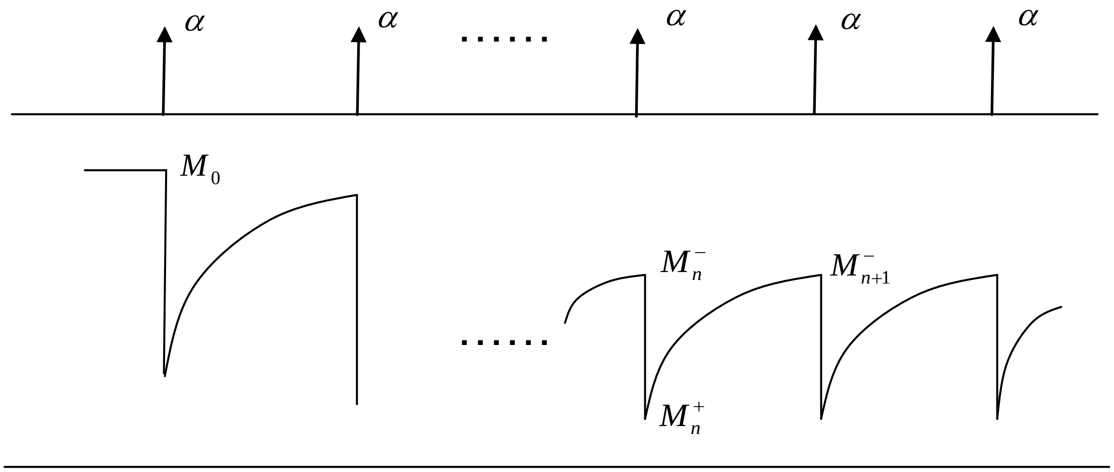

Figure 2.9. Longitudinal magnetization approaching the steady state in a spoiled GRE sequence.

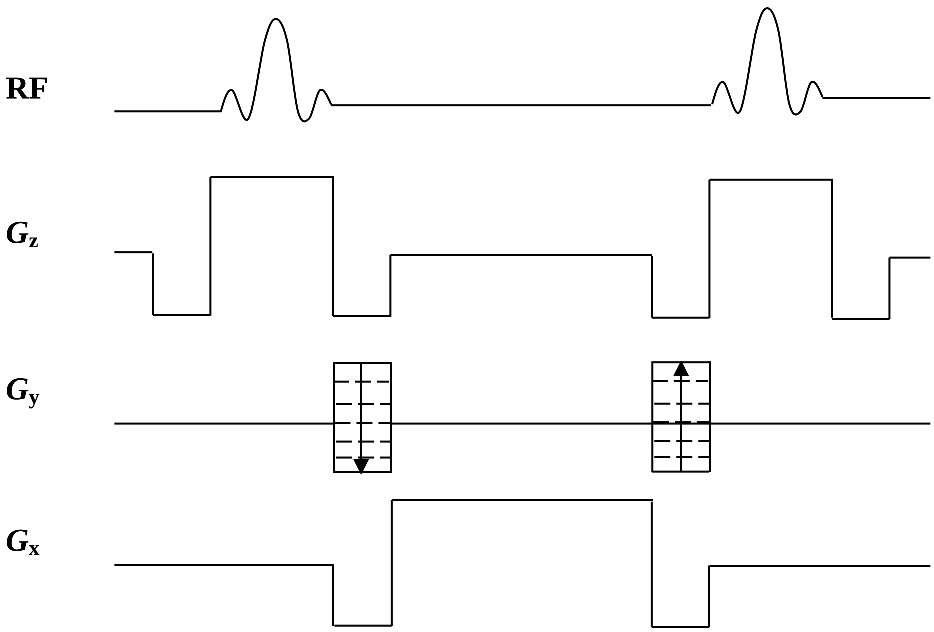

Figure 2.10. Pulse sequence diagram of a balanced SSFP sequence. All the gradients are balanced to maintain steady state of longitudinal and transverse magnetization.

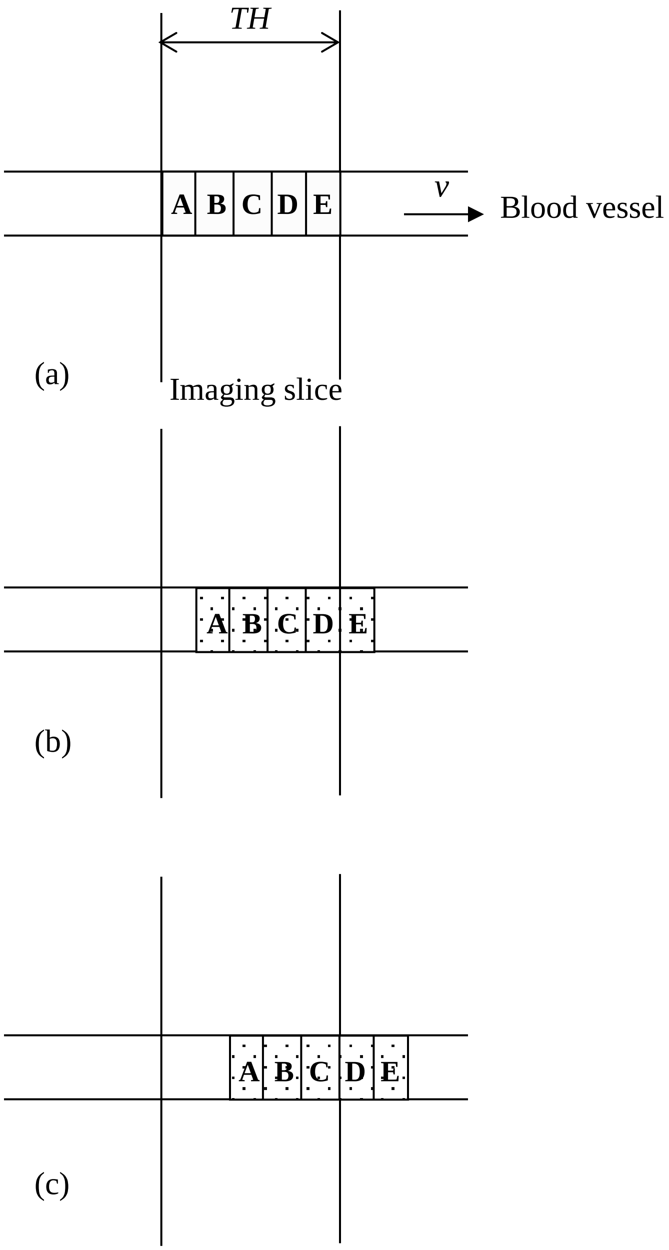

Figure 2.11. Illustration of the inflow effect. An imaging slice is divided into five subslices (a) for demonstration purpose. The incoming fresh blood replace subslice *E* (b) and *D* (c) in the first and second *TR*. Relation between the MR signal affected by the number of RF excitations seen by the moving spins and the velocity allows quantification of the flow.

Table 2. 1 NMR properties of nuclei used in MR imaging and spectroscopy

Nucleus	Gyromagnetic Ratio (10^8 rad/T/s)	Resonance Frequency at 1T (MHz/T)	Natural Abundance (%)	Relative Sensitivity
^1H	2.675	42.577	99.985	1.0000
^3He	-2.038	32.433	0.00014	0.4423
^{13}C	0.673	10.705	1.108	0.0159
^{17}O	-0.365	5.772	0.037	0.0290
^{19}F	2.517	40.055	100	0.8340
^{23}Na	0.708	11.271	100	0.0925
^{31}P	1.081	17.235	100	0.0663

CHAPTER 3

3D MULTIPARAMETRIC BREAST MRI SEGMENTATION USING HIERARCHICAL SUPPORT VECTOR MACHINE WITH COIL SENSITIVITY CORRECTION

Reprinted from Academic Radiology, 20/2, Y. Wang, G. Morrell, M. Heibrun, A. Payne and D. L. Parker, 3D multi-parametric breast MRI segmentation using hierarchical support vector machine with coil sensitivity correction, 137–47, Copyright (2013), with permission from Elsevier.

Introduction

Breast magnetic resonance (MR) imaging has become a very useful imaging modality for breast cancer screening and diagnosis (34). It has been shown that 17–34 % of cancer foci visible on breast MRI are not detected by mammography (35). Not only does breast MRI offer higher sensitivity for detection of breast cancer than x-ray mammography, ultrasound, clinical examination, or any combination of these, it also has a superior ability to delineate fatty and fibroglandular tissue (36).

Although lesions can be detected by visual inspection of breast MRI images, including dynamic contrast enhanced (DCE) studies, there is evidence that quantitative measurements of different structures in the breast with and without contrast can assist not only in the detection of abnormal tissues, but also in the discrimination between fibroadenomas, cysts, and various types of malignancies (34,37). In an attempt to improve the performance of breast computer-aided diagnosis (CAD) systems that are designed to supplement visual inspection and interpretation of breast MRI, methods for fully- and semi-automatic segmentation of lesion mass based on DCE-MR images have been developed (38,39). Efforts have also been made to discriminate between benign and malignant lesions using quantitative morphological and feature analyses (40,41). In addition to automatic lesion detection and discrimination, breast tissue segmentation could also be used to determine the percentage of fibroglandular tissue present in the breast, which is directly linked to breast parenchymal patterns (42,43), where the parenchymal pattern characterization parameters are taken as risk factors of developing breast cancer (36).

Breast tissue classification is an essential initial step for breast MRI qualitative and quantitative analyses. In addition, segmentation of breast tissue can also be useful in interventional treatments that require accurate knowledge of the internal anatomy of the breast, such as magnetic resonance guided high-intensity focused ultrasound (MRgHIFU) therapy. For this treatment modality, pretreatment planning, real-time control of treatment, and posttreatment evaluation can be improved with accurate segmentation of fatty tissue, fibroglandular tissue, lesion and skin. A primary motivation for this paper is to improve the accuracy of segmented models that are used to predict ultrasound field distributions in the breast and thus assist in planning focused ultrasound procedures to treat breast lesions. Since the variation of the thermal and acoustic properties between different tissue types affects both the simulated ultrasound beam pattern and the resulting thermal models, it is essential to not only know the distribution of the lesion to be treated, but also the acoustic and thermal properties of the tissue along the proposed ultrasound trajectory. Additionally, segmentation of fatty and glandular tissue is essential for MRI based temperature measurements because phase-based MRI thermometry works in glandular tissue but not in fat (11).

Multiparametric inputs to tissue segmentation routines have previously included T_1, T_2 and proton density (PD) weighted images (5,44). T_1-weighted (T_1-w) and PD-weighted (PD-w) images generally show clear contrast between fatty and fibroglandular tissue; fat-suppressed (FS) T_2-weighted (T_2-w) images provide good delineation of fluid (water)-containing structures, such as cysts, necrosis and fibroadenomas (45). In our methodology, to emphasize the fatty-fibroglandular tissue contrast, three-point Dixon water-only and fat-only contrasts are also included in the multiparametric inputs, which are then input into the subsequent preprocessing and segmentation routines. Our hypothesis is that image pixels each represented by a five-element vector in the multidimensional feature space composed of T_1, T_2, PD, three-point Dixon water-only and fat-only contrasts can be accurately classified using the presented segmentation schemes.

Prior to performing intensity-based tissue classification it may be necessary to correct for intensity inhomogeneity—often times called ‘bias field’—across the imaging field of view (FOV), which is very common in MR imaging because of the nonuniform coil sensitivity distribution, especially when surface coils are used. Meyer (46) estimates that the intensity variation across the image FOV can be as much as 30% of image amplitudes. Although this effect of coil sensitivity on MR images can sometimes be disregarded when viewed by an expert radiologist making qualitative diagnosis, the intensity variation can be especially challenging to computerized MR segmentation (47). The inhomogeneity results in broadening of the signal intensity distribution for each particular tissue type, which results in further ambiguity and inaccuracy when classifying different tissue types. Based on whether the coil sensitivity map is obtained during or after the scan, bias field correction algorithms can be categorized as prospective (48,49) or retrospective (43,47).

Various algorithms have been applied for breast tissue segmentation in MR images. Fuzzy c-mean (FCM) (50), an iterative algorithm that assigns voxels into groups according to their distance measured in a feature space, has been used in lesion detection (51) and fibroglandular tissue density quantification (42). Iterative self-organizing data (ISODATA) (5), as a derivation from k-mean clustering with additional features of splitting and merging steps to adjust the number of clusters, were investigated for differentiating benign and malignant lesions. A hierarchical k-mean clustering procedure (52) was employed for lesion tissue detection in a murine model. Spectral signature detection approaches (53,54) and conventional SVM (44) have also been studied for the classification of breast tissues.

In this work, we present a hierarchical SVM-based 3D breast tissue classification workflow and evaluate the utility of each preprocessing and final segmentation steps. The importance of incorporating three-point Dixon water-only and fat-only images in the multiparametric inputs and the implementation of intensity inhomogeneity correction are demonstrated. The performance of the presented hierarchical SVM in segmenting breast tissue into fatty, fibroglandular, lesion and skin components is compared with that of conventional SVM and FCM. A measure of algorithm stability is made by comparing the tissue classification obtained from different orientations of the 3D volumes. Statistical analysis shows that the segmentation performance of the proposed methodology is repeatable and exceeds that of conventional algorithms.

Materials and methods

Subjects and image acquisition

Imaging was performed on a Siemens MAGNETOM TIM Trio 3T MRI scanner (Siemens, Erlangen, Germany) using a four-channel breast coil. With informed consent obtained from the volunteers, four subjects (three normal subjects and one subject with confirmed fibroadenoma) were examined using the following protocol: unilateral imaging of 88–100 sagittal slices with a FOV=192x192 mm^2, matrix size = 192x192 and slice thickness = 1 mm, resulting in the 1 mm^3 isotropic resolution. T_1-w three-point Dixon was performed using a 3D gradient echo (GRE) sequence with TR/TE1/TE2/TE3=11/4.7/5.75/6.8 ms; T_2-w and PD-w images were acquired using a 2D turbo spin echo (TSE) sequence with bandwidth (BW) = 789 Hz/Px, echo trains per slice = 15, TR/TE = 13s/91ms and 13s/8.2ms, respectively. All together, multiparametric combination of T_1-w, FS T_2-w, PD-w and three-point Dixon water-only and fat-only MR images were obtained.

Preprocessing

The multistage preprocessing routine is comprised of six steps, including co-registration, zero-filled interpolation (ZFI), three-point Dixon reconstruction, skin extraction, coil sensitivity estimation, and optimal SNR reconstruction with bias field correction, as detailed in the following descriptions. All the data analyses were performed using Matlab (The MathWorks, Natick, MA, USA).

Coregistration

The total image acquisition time for a subject using the protocol mentioned above is 20–30 minutes. During the course of the data acquisition, motion may occur due to subject movement and other physiological activities, such as respiratory and cardiac movement. Coregistration was therefore performed by manually adjusting the displacement to correct for the misalignment between different scans. All the images from the five MR multiparametric inputs needed to be coregistered, and a T_1-weighted image was selected as the reference sequence. Specifically, since the water-only and fat-only are derived from the T_1-weighted images, the only registration needed for the Dixon images was to correct for the relative fat-water shift due to the chemical shift. The amount of the shift could be calculated using the readout bandwidth and the 420 Hz frequency shift between fat and water at 3T. Further, T_2-w and PD-w images were registered to the T_1 sequence, where a single slice from each volumetric data were overlaid on the T_1-w image with the same slice location. The same amount of adjustment was then applied to the whole image volume.

Zero filled interpolation

ZFI creates reduced voxel spacing by filling zeros surrounding the original k-space measurements. Even though this processing does not change the spatial resolution of the original data, the denser imaging grid smoothes out the images and alleviates the partial volume effects (55). To study the impact of ZFI on segmentation, a factor of two ZFI was applied and the segmentation performance with ZFI was compared to the performance without ZFI.

Three-point Dixon reconstruction

In three-point Dixon (56), the small frequency difference between the fat and water signal, and the resulting phase difference as a function of TE, make it possible to separate the fat and water signal by acquiring images at different values of TE. In our technique, images were acquired with fat and water in phase at TE = 4.7 and 6.8ms, and with fat and water 180° out of phase at TE=5.75ms. The phase difference between the two in-phase images was used to obtain the phase evolution due to other factors, such as the magnetic field inhomogeneity. Furthermore, by averaging the magnitude signal from the two in-phase images, the signal approximates the same effective T_2* decay as that of the opposed-phase images because of the sequential acquisition of in-phase (TE = 4.7ms), out-of-phase (TE = 5.75ms), and again in-phase (TE = 6.8ms) images (57). Water-only and fat-only images can thus be obtained based on the opposed-phase and averaged in-phase images. To overcome any phase wrap that appeared in the phase images, an unwrapping algorithm based on a solution of the Poisson equation (58) was used. The separated water-only and fat-only images guarantee a clear separation of fibroglandular and fatty tissues. Moreover, three-point Dixon reconstruction provides excellent delineation of skin facilitating skin extraction in the multistage preprocessing procedure, as explained following.

Skin extraction

In breast MRI, skin and fibroglandular tissue commonly share similar signal intensities. The impact of skin segmentation on quantitative measurement of breast density was studied by Nie *et al.* (59). Due to the overlap of the signal intensity from skin and that from fibroglandular tissue in the multispectral feature space, we separate out the skin segmentation from the SVM process. Based on three-point Dixon water-only images, where the bright signal of skin is sharply delineated from the surrounding background and breast tissues, a Canny filter (60) was used as an edge detector and pixels in between the boundaries were assigned as skin component.

Coil sensitivity estimation

To correct for the intensity inhomogeneity, the sensitivity for each individual coil was estimated retrospectively using the algorithm developed by P. Vemuri *et al.* (61). The algorithm does not require an increase in imaging time and eliminates the possible discrepancies between the estimated and true coil sensitivity profiles. Assuming that the sensitivity varies slowly as a function of position, sensitivity magnitude profiles of the individual coil elements were obtained by fitting a lower order polynomial function to the image intensity occupied by a dominant tissue type. In our application, depending on whether fatty or fibroglandular tissue was the dominant tissue in the breast, three-point Dixon fat-only or water-only images were used to determine the pixels for the polynomial fitting.

Optimal SNR reconstruction

With the estimated coil sensitivity map, the optimal SNR images were calculated where each coil was reconstructed separately and combined with weights that are a function of voxel location (62). Mathematically, optimal SNR reconstructed image I_{opt} can be calculated by:

$$I_{opt}(\mathbf{r}) = \frac{\mathbf{R}(\mathbf{r})\boldsymbol{\Psi}^{-1}\mathbf{S}^{T}(\mathbf{r})}{\mathbf{S}(\mathbf{r})\boldsymbol{\Psi}^{-1}\mathbf{S}^{T}(\mathbf{r})} \qquad [3.1]$$

where **r** denotes the position in the image space; $\mathbf{R}(\mathbf{r}) = [R_1(\mathbf{r}), R_2(\mathbf{r}), \ldots, R_L(\mathbf{r})]$ is the row vector of coil images; $\mathbf{S}(\mathbf{r}) = [S_1(\mathbf{r}), S_2(\mathbf{r}), \ldots, S_L(\mathbf{r})]$ is the row vector of coil sensitivities estimated from above step; $\boldsymbol{\Psi}$ is an L by L matrix which describes the coupling and noise correlations between the coil elements. The noise matrix was assumed to be an identity matrix in the actual calculation for simplicity, and it was shown by Roemer *et al.* (62) that there was only a 10% SNR loss when assuming there is no noise correlation.

Tissue segmentation using hierarchical SVM

The supervised learning algorithm, SVM (63,64), uses training data to construct hyper-planes to minimize the margin between classes. The program learns behavior by using a small amount of the input data to train the SVM algorithm and then applies this learned behavior to the rest of the dataset. Instead of segmenting breast tissue into a specified number of target tissues types by applying SVM once as in the conventional manner, the SVM processing was divided into hierarchical stages where in each stage only two tissue types were classified. We decompose the one-time multiclass segmentation into hierarchical binary-class segmentation. Fig. 3.1 shows the schematic structure of the hierarchical SVM with corresponding multiparametric inputs and target output tissue types. Different combinations of multiparametric images were assigned at each level of SVM. In the first stage (level), the entire dataset was classified into background vs. breast tissue using the PD-w images. After excluding the background pixels, the second stage of SVM was applied to the tissue pixels only. T_1-w and three-point Dixon fat-only and water-only images were selected as the input features to segment out fatty tissue from the nonfatty tissues, including fibroglandular tissue, skin and lesion (if present). In the third stage, lesion vs. nonlesion pixels (i.e., fibroglandular tissue and skin) were classified with inputs being T_1-w, T_2-w and PD-w images. In the final step, outputs from all three stages were combined and presented in a final color map with each color representing a single tissue type. The multiclass classification problem was decomposed into multiple binary-class classification problems. Better performance is expected because designing a classifier for separating two classes is easier than designing a classifier to separate multiple classes simultaneously (65). For comparison, we evaluated segmentation using conventional SVM and one of the most widely used unsupervised learning algorithms — fuzzy c-mean clustering with identical multi-parametric input. All the human volunteer studies were approved by the local institutional review board.

Statistical analysis

The performance of the proposed hierarchical SVM along with conventional SVM and FCM were evaluated by comparing with the manual classification performed by an experienced breast radiologist blinded to the segmentation results. Specifically, about 100 points were selected on each slice in a spatially random manner to which the radiologist assigned different tissue types. Even though random sampling results in unbalanced sampling points for different tissue types, complete randomness avoids any potential bias in the interpretation of radiologists who are blinded to the segmentation results. The classification accuracy of the algorithms on the 3D volumetric datasets was evaluated by measuring the overlap ratio of segmentation results with the manual classification as the gold standard. The overlap ratio is defined as the ratio of the points that are correctly classified by the computer program based on the radiologist's classification to the total number of pixels that are randomly chosen for the radiologist to classify. The impacts of the preprocessing steps, including coregistration, ZFI and coil sensitivity correction, were quantitatively accessed by comparing the overlap ratio from segmentation with and without these procedures. Additionally, consensus reading is attained on one subject by adding a second breast radiologist, to quantify the expected interobserver variability of manual segmentation. Lastly, a measure of algorithm stability was made by comparing the segmentation obtained using sagittal and axial views of the 3D volumes.

Results

Fig. 3.2 (a) shows an example slice from a 3D multiparametric input of a subject with a confirmed fibroadenoma (circled). Image contrasts of T_1-w, T_2-w, PD-w, three-point Dixon fat-only and water-only are shown from left to right. In Fig. 3.2 (b), image intensities from region of interest on fatty tissue, fibroglandular tissue, skin, fibroadenoma and background are plotted in a 3D feature space composed of T_1, T_2 and PD contrast. It is noticeable in Fig. 3.2 (b) that the signal of skin overlaps with that of the fibroglandular tissue, which makes the classification problem non-separable. Therefore, we take skin extraction as an independent step from the final tissue classification.

To show the range of the datasets included in this study, the central slice of T_1-w images from each dataset is displayed in Fig. 3.3. The scaling is included in the figure to indicate the relative size of the breasts. These four datasets represent a wide range of breast volumes, shapes and densities.

The necessity of coregistration is illustrated in Fig. 3.4. Due to the motion, PD-w image in the multiparametric input was off to the right by two pixels relative to the rest of the dataset. After the translational shift was manually corrected, the one-side misclassification at the tissue boundary of the fibroglandular tissue island and the surrounding fatty tissue (see Fig. 3.4 (a)) is reduced, as shown in Fig. 3.4 (b).

Fig. 3.5 (a, b) shows an example sagittal slice of three-point Dixon water-only image and the edge detection results after applying a Canny filter. Pixels between the inner and outer boundary of the skin were assigned as skin component, presented in Fig. 3.5 (c).

A slice of PD-w images from a healthy subject is displayed in Fig. 3.6 (a) with clear bias field inhomogeneity across the imaging FOV. The signal intensity varies as the proximity of breast to the phased-array coils changes. Fig. 3.6 (b) and (c) show the estimated coil sensitivity and the optimal SNR reconstructed image with corrected bias field, respectively. The corrected image shows good intensity uniformity, which improves the accuracy of the breast tissue segmentation.

Histograms of breast tissue signal intensity of the example shown in Fig. 3.6 are plotted in Fig. 3.7. The narrowing of the histogram after coil sensitivity correction indicates the importance of intensity inhomogeneity correction in computerized tissue segmentation, because the histogram width depends greatly on image intensities.

Lateral projection through the 3D volumetric segmentation output of the hierarchical SVM for the subject with confirmed fibroadenoma is demonstrated in Fig. 3.8. A slice of segmentation output from hierarchical SVM, conventional SVM and FCM with identical multiparametric input is displayed in Fig. 3.9. It is evident that hierarchical SVM outperforms the conventional SVM and FCM in terms of the least misclassification error, referring to the anatomical input shown in Fig. 3.2 (a). The observation is further confirmed by the statistical analysis performed based on the complete 3D volumes, where the overlap ratios were calculated for each algorithm in comparison to radiologist’s manual classification, as listed in Table 3.1.

To get more insight into the statistics given in Table 3.1, the performances of segmentation for each individual tissue type are presented in Tables 3.2–3.6. Specifically, for each tissue type that was manually classified by the radiologist, the corresponding classification outputs from the hierarchical SVM are listed. Pixels that were correctly classified, incorrectly classified and the resulting overlap ratios for dataset #1–4 are presented in Tables 3.2–3.6, respectively.

To further understand the performance of segmentation from hierarchical SVM along axial and sagittal directions, the tissue specific overlap ratios from the two orientations are calculated based on the combined data from subject #1 and #2, as listed in Table 3.7.

Discussion

A 3D hierarchical SVM-based segmentation algorithm was proposed for breast MRI tissue segmentation, with special emphasis on the inclusion of three-point Dixon images in the multiparametric MR inputs and coil sensitivity correction as one of the critical preprocessing steps. The segmentation output from hierarchical SVM was compared with other algorithms —conventional SVM and FCM. It was shown that the proposed breast MRI classification workflow segments tissue with the highest accuracy.

In our technique, the binary hierarchical SVM decomposes the four-class classification problem into three subproblems, each separating two classes, as illustrated in Fig. 3.1. Since each classifier is simpler, better classification performance is expected, as confirmed by the statistics from Table 3.1. The average computational time for a complete 3D volume was 6 minutes on a desktop PC with Intel Core 2 Duo CPU and 2.98GB of RAM.

The primary motivation of the presented methodology is to provide a segmented breast tissue model as input to ultrasound beam simulations in MRgHIFU treatments. However, this technique may also be useful for other purposes such as diagnostic evaluation. Segmentation of tissue types does not remove information from the images, but rather classifies by tissue type. Segmentation of skin may be helpful for clinical evaluation; a segmented image depicting the skin alone might make abnormal skin thickening more easily visible.

The unsupervised learning algorithm FCM has been used for lesion segmentation on localized areas successfully (51). However, for larger FOV data sets, one tissue type could end up being classified into multiple clusters. When a predetermined number of tissue types are specified in FCM, as in the presented case, the dominant tissue is likely to be classified into more than one cluster, while a tissue type with fewer pixels could be overlooked in the clustering process. Therefore, while the FCM algorithm is completely data driven, human intervention is required during postprocessing to assign the misclassified voxels to the desired target tissue type.

The importance of the three preprocessing steps on the accuracy of segmentation was evaluated as shown in Table 3.1. Performance degradation is clearly seen when the image intensity inhomogeneity caused by the coil sensitivity is not considered. However, ZFI did not provide significant improvement in the classification output statistically. This may be because, due to the complete randomness in choosing the sampling points, the calculated overlap ratios may not fully represent the advantage of ZFI, because one would expect the improvement from ZFI to appear mostly on the tissue boundaries. Based on the overlap ratios with and without coregistration, improved accuracy by applying coregistration can be seen from dataset #1 and 4, but not dataset #2 and 3. This could possibly be explained by the different degree of motion associated with different datasets. In dataset #1 for example, the PD-w images need to be shifted four pixels relative to the T1-w due to movement of the subject between image acquisitions, as compared to one pixel in dataset #2. Therefore, more significant improvement is anticipated from applying coregistration on these datasets.

The statistics for individual tissue type suggest that for certain tissue types, such as skin and lesion, the overlap ratios are lower in comparison to other tissue types, as shown in Tables 3.2–3.6. Spatially, the misclassified pixels mostly appear at the tissue boundary. For example, the fibroadenoma in dataset #1 is surrounded by fibroglandular tissue, and the misclassified fibroadenoma pixels were all incorrectly assigned as fibroglandular tissue in Table 3.2. Based on the manual classification from the two radiologists, individual tissue segmentation of dataset #1 was evaluated in Tables 3.2 and 3.3. A good correlation is found between the two radiologists' segmentation because of a reasonably consistent overlap ratios across various tissue type. The correlation coefficient between the two readers is 90.23%. Detection of lesions and delineation from normal fibroglandular tissue is difficult, and in clinical practice requires administration of intravenous contrast. Therefore, it is not surprising that any method using only noncontrast images, whether automated or manual, is less effective at classifying fibroglandular tissue vs. solid breast lesions. Future work will investigate the potential improvement of tissue classification accuracy with the incorporation of contrast-enhanced scans as an input to the algorithm.

The consistency of the presented results in both the sagittal and axial orientations, shown in Tables 3.1 and 3.7, indicates the stability of the proposed segmentation routine and also implies the robustness to the possible variations in the generation of training data. This suggests that the proposed algorithm could be applied in longitudinal follow-up studies to detect changes, e.g., the change of breast density evaluation for risk assessment, and for posttreatment evaluation of neoadjuvant chemotherapy.

Currently, the targeted segmentation tissue types include only fatty tissue, fibroglandular tissue, skin, and lesions. Components such as blood vessels were not considered. Efforts are being made to visualize blood vessel while suppressing the fibroglandular tissue so that the segmentation could be further improved by incorporating more tissue types. Investigation into this improvement is ongoing and will be evaluated in both normal subjects and those with confirmed breast lesions.

Conclusions

Breast tissue classification of MRI data may be useful to aid in the diagnosis of breast cancers and to assess breast cancer risk based on breast density. In this work, a hierarchical SVM algorithm along with a series of preprocessing schemes was presented to automatically segment breast tissues using 3D multiparametric breast MRI. The importance of multiparametric MRI contrasts and coil sensitivity correction was investigated. Results show that more accurate breast MRI segmentation can be obtained using the hierarchical SVM with proper preprocessing compared to other available algorithms.

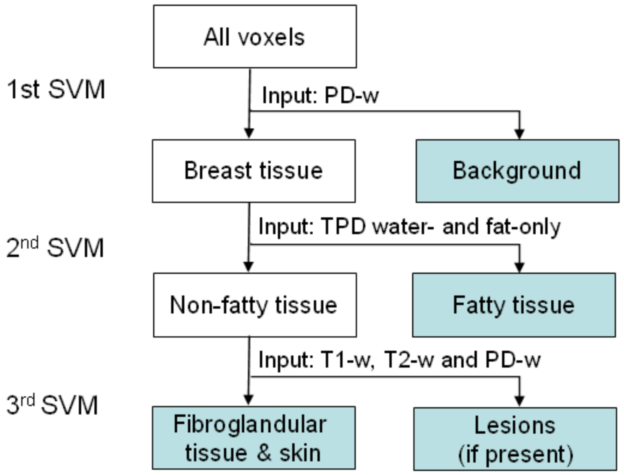

Figure 3.1. Schematic structure of hierarchical SVM process with corresponding input feature and output segmented tissue type.

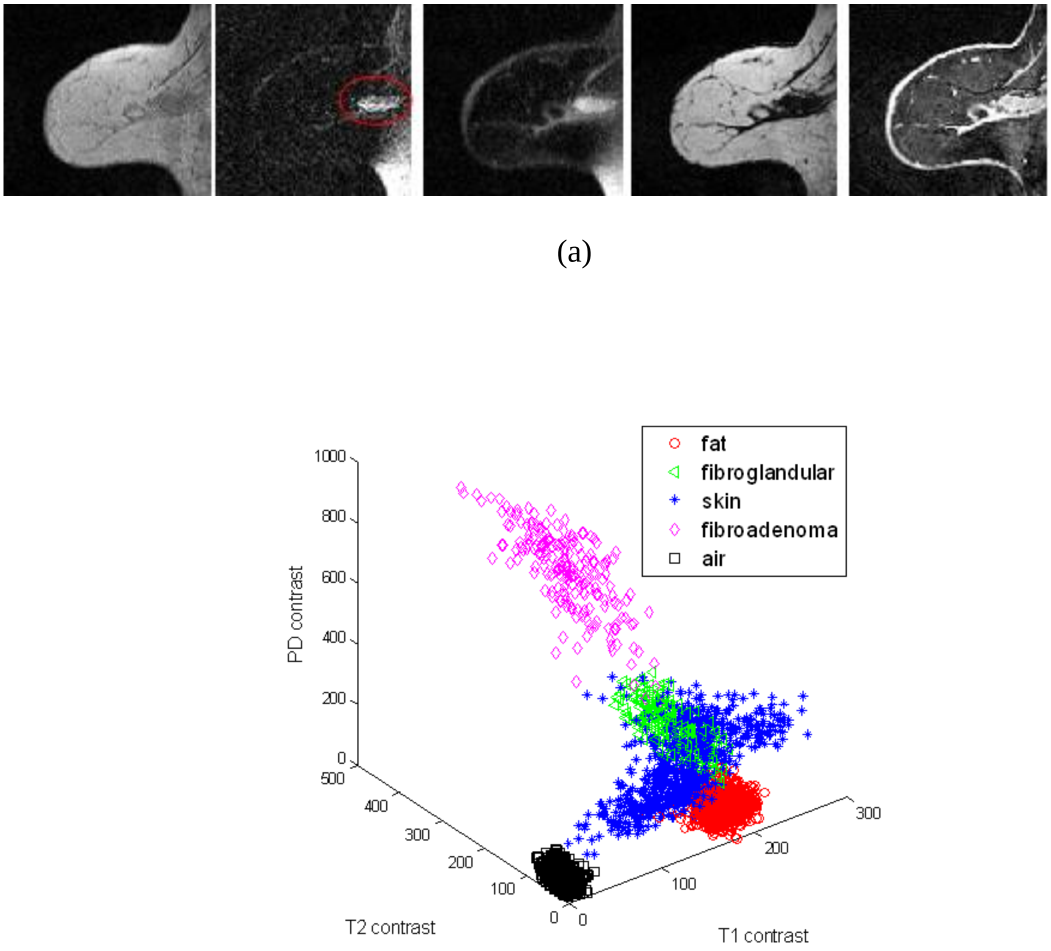

(a)

(b)

Figure 3.2. Multiparametric input of a subject with confirmed fibroadenoma (circled). (a) An example sagittal slice from the multiparametric input. Contrasts displayed from left to right: T_1, FS T_2, PD, three-point Dixon fat-only and water-only images. (b) Region of interest based image intensities from fatty tissue, fibroglandular tissue, skin, fibroadenoma and background are plotted in a 3D feature space composed of T_1, T_2 and PD contrast.

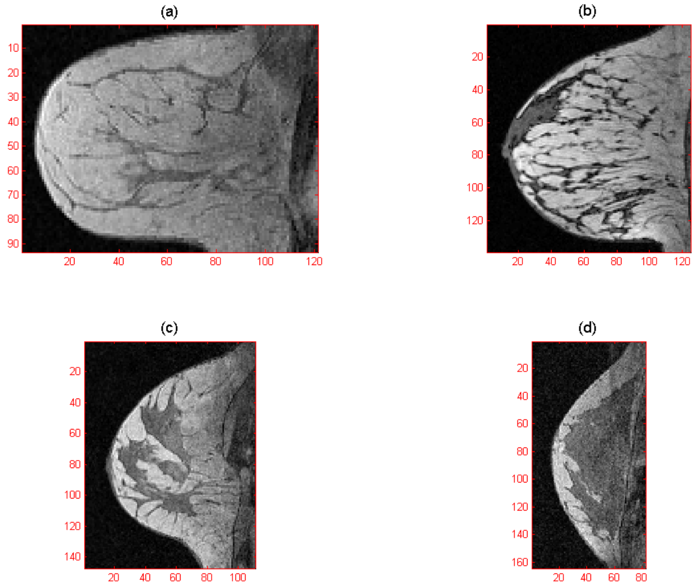

Figure 3.3. The central slice of T_1-w images from dataset 1–4 is displayed in (a)–(d), respectively. The axes units are in mm. The four datasets in this study represent a wide range of breast volumes, shapes and densities.

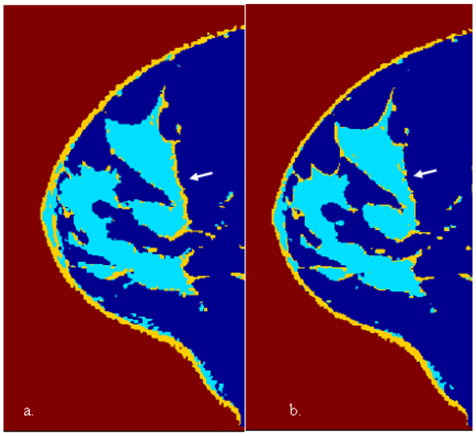

Figure 3.4. Segmentation output (a) without and (b) with coregistration. Fatty tissue, fibroglandular tissue, skin and fibroadenoma are presented in dark blue, light blue, yellow and red, respectively. The misclassification appears on the border of the fibroglandular tissue island (light blue) and the surrounding fatty tissue (dark blue) drops considerably after coregistration, as pointed by the arrow.

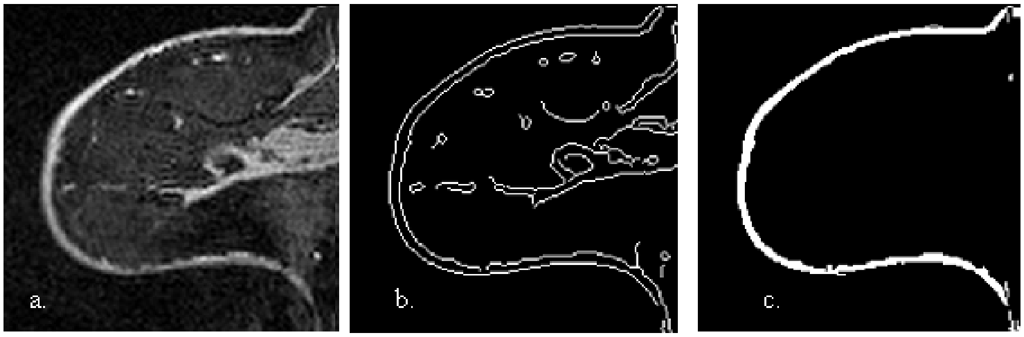

Figure 3.5. Skin extraction using (a) three-point Dixon water-only image; (b) Canny filtering output; (c) final skin pixels extracted from the water-only image.

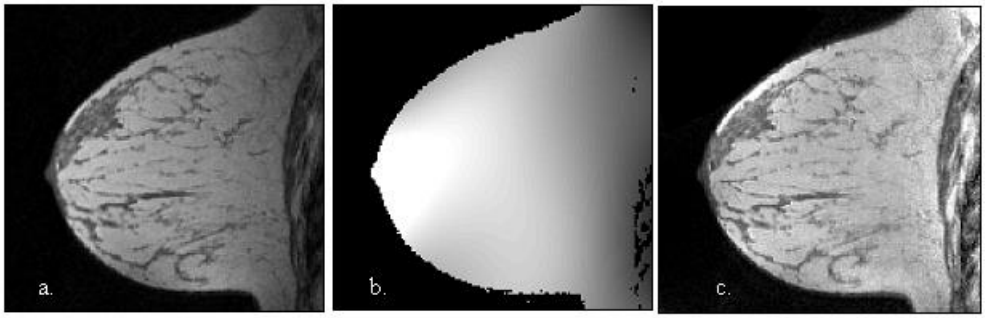

Figure 3.6. Coil sensitivity correction on an example PD-w sagittal image of a healthy subject. (a) Original image, (b) estimated coil sensitivity, and (c) optimal SNR reconstructed image with coil sensitivity correction.

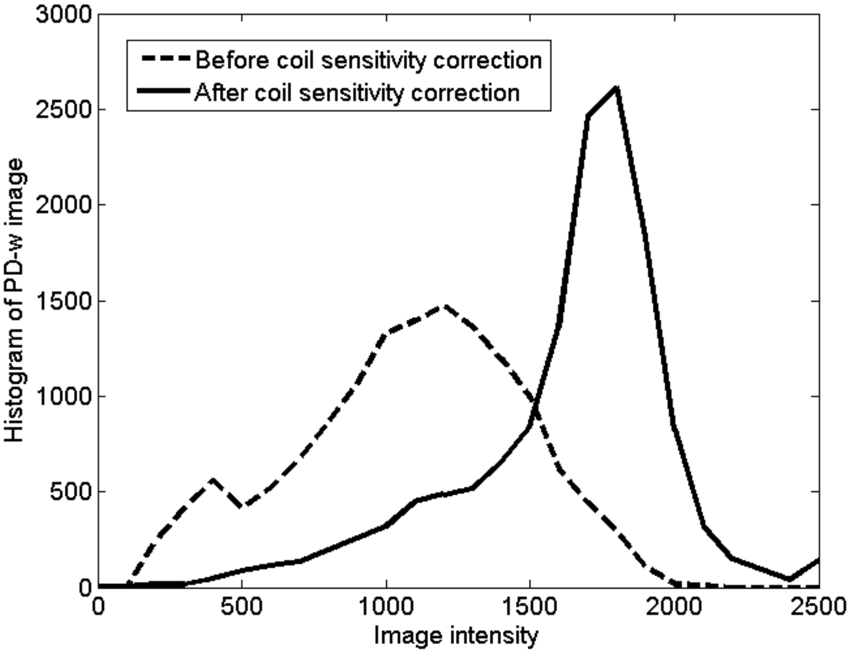

Figure 3.7. Line plot of histograms of image intensity before and after coil sensitivity correction, based on the example from Fig. 3.6.

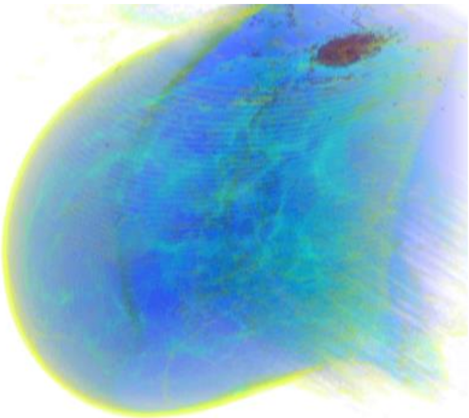

Figure 3.8. Lateral projection through the 3D volumetric segmentation output of the hierarchical SVM algorithm for the subject with confirmed fibroadenoma. Fatty tissue, fibroglandular tissue, skin and fibroadenoma are presented in blue, green, yellow, and red, respectively.

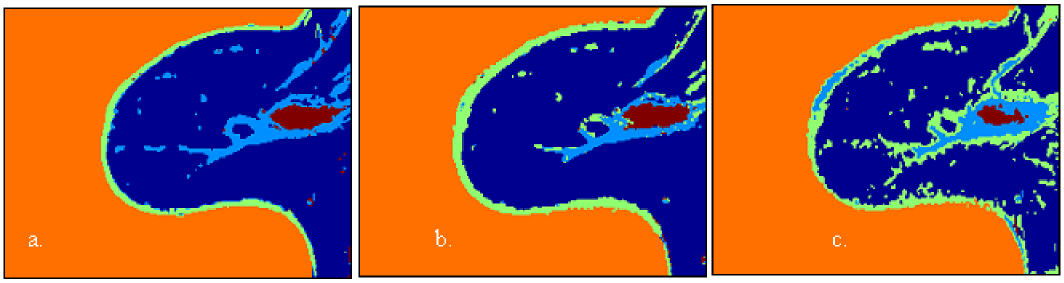

Figure 3.9. Segmentation output of (a) hierarchical SVM, (b) conventional SVM, and (c) FCM from the subject with a confirmed fibroadenoma. Fatty tissue, fibroglandular tissue, skin and fibroadenoma are presented in dark blue, light blue, green and red, respectively. The corresponding multiparametric input was shown in Fig. 3.2.

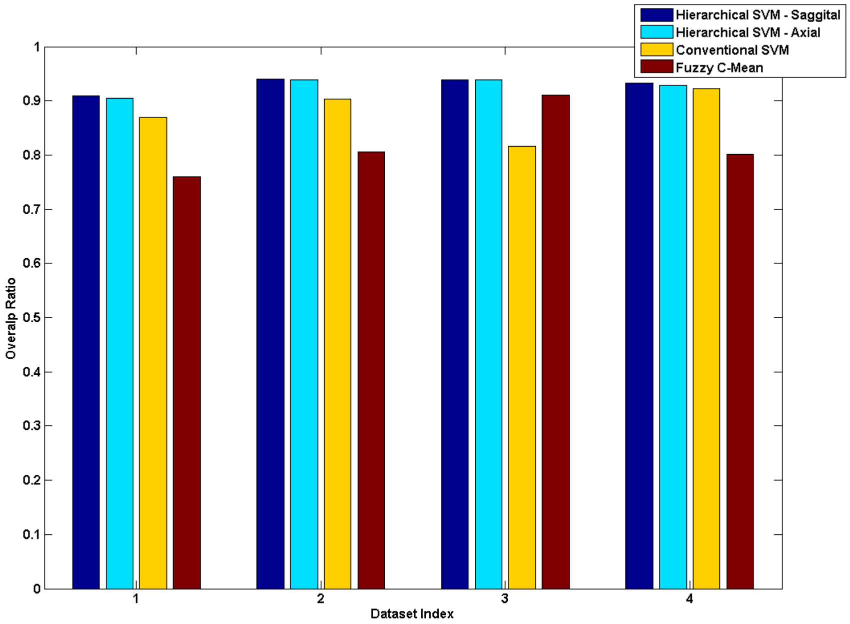

Figure 3.10. Bar diagram illustration of the overlap ratios from hierarchical SVM along saggital and axial directions, conventional SVM, and fuzzy c-mean algorithms for four datasets, according to Table 3.1. The overlap ratios are calculated by comparing the performance of the methods to manual segmentation by radiologist. Consistently higher overlap ratios from the hierarchical SVM along both directions indicate the superior performance and stability of the hierarchical SVM than other algorithms.

Table 3.1 Overlap ratios of various algorithms with radiologist's manual classification as ground truth

Overlap Ratio	h-SVM (saggital)	h-SVM (axial)	c-SVM	FCM	h-SVM w/o CSC	h-SVM w/o ZFI	h-SVM w/o co-registration
dataset #1	90.94%	90.47%	86.97%	75.96%	82.09%	90.69%	88.81%
dataset #2	94.08%	93.92%	90.30%	80.58%	83.42%	94.50%	93.67%
dataset #3	93.90%	93.90%	81.68%	91.02%	95.45%	94.41%	95.38%
dataset #4	93.25%	92.79%	92.28%	80.06%	81.39%	92.76%	81.12%

Hierarchical SVM (h-SVM) offers highest overlap ratio than the conventional SVM (c-SVM) and the FCM algorithm. Three preprocessing steps, coil sensitivity correction (CSC), zero-filled interpolation (ZFI), and coregistration are also evaluated.

Table 3.2 Tissue type analysis of dataset #1 segmentation from Radiologist #1

Hierarchical SVM Radiologist	Fat	Fibroglandular	Skin	Lesion	Air	Overlap Ratio
Fat	**3877**	165	45	4	116	92.16%
Fibroglandular	222	**467**	17	2	1	65.87%
Skin	8	37	**180**	2	91	56.60%
Lesion	0	8	0	**8**	0	50.00%
Air	6	30	14	0	**3401**	98.55%

Correctly classified, incorrectly classified and overlap ratios of hierarchical SVM for each individual tissue type, comparing to the manual classification from Radiologist #1.

Table 3.3 Tissue type analysis of dataset #1 segmentation from Radiologist #2

Hierarchical SVM / Radiologist	Fat	Fibroglandular	Skin	Lesion	Air	Overlap Ratio
Fat	**3483**	122	22	0	112	93.15%
Fibroglandular	445	**467**	211	1	0	50.00%
Skin	73	40	**200**	2	15	46.51%
Lesion	0	1	0	**7**	0	87.50%
Air	19	33	14	0	**3378**	98.08%

Correctly classified, incorrectly classified and overlap ratios of hierarchical SVM for each individual tissue type, comparing to the manual classification from Radiologist #2.

Table 3.4. Tissue type analysis of segmentation for dataset #2

Hierarchical SVM / Radiologist	Fat	Fibroglandular	Skin	Air	Overlap Ratio
Fat	**3279**	180	33	45	92.71%
Fibroglandular	142	**632**	9	3	80.41%
Skin	6	83	**143**	56	49.65%
Air	2	7	12	**5443**	99.62%

Correctly classified, incorrectly classified and overlap ratios of hierarchical SVM in sagittal orientation for each individual tissue type in dataset #2.

Table 3.5. Tissue type analysis of segmentation for dataset #3

Hierarchical SVM / Radiologist	Fat	Fibroglandular	Skin	Air	Overlap Ratio
Fat	**3006**	40	0	28	97.79%
Fibroglandular	115	**379**	0	2	76.41%
Skin	27	85	**110**	39	42.15%
Air	123	4	2	**4046**	96.91%

Correctly classified, incorrectly classified and overlap ratios of hierarchical SVM in sagittal orientation for each individual tissue type in dataset #3.

Table 3.6. Tissue type analysis of segmentation for dataset #4

Hierarchical SVM Radiologist	Fat	Fibroglandular	Skin	Air	Overlap Ratio
Fat	**1223**	52	12	180	83.37%
Fibroglandular	26	**1340**	1	57	94.10%
Skin	9	78	**145**	38	53.70%
Air	3	22	29	**4517**	98.82%

Correctly classified, incorrectly classified and overlap ratios of hierarchical SVM in sagittal orientation for each individual tissue type in dataset #4.

Table 3.7. Overlap ratios of hierarchical SVM at two orientations (sagittal and axial) for each individual tissue type

Saggital SVM Axial SVM	Fat	Fibroglan-dular	Skin	Lesion	Air	Total Points	Overlap Ratio
Fat	**4,532,681**	156,116	3,926	967	19,280	4,712,970	96.17%
Fibroglandular	50,442	**1,027,900**	0	1,178	7,192	1,086,712	94.59%
Skin	1,629	0	**268,830**	252	1,330	272,041	98.82%
Lesion	18	994	110	**4,123**	18	5,263	78.34%
Air	6,807	8,440	52	0	**5,482,907**	5,498,206	99.72%

CHAPTER 4

FLOW MEASUREMENT IN MRI USING ARTERIAL SPIN LABELING WITH CUMULATIVE READOUT PULSES – THEORY AND VALIDATION

This chapter is based on a paper entitled “Flow measurement in MRI using arterial spin labeling with cumulative readout pulses — theory and validation” written by Y. Wang, S-E. Kim, E. DiBella and D. L. Parker, published in Medical Physics. 2010, 37(11): 5801–5810.

Introduction

Arterial spin labeling (ASL) is a perfusion magnetic resonance imaging (MRI) technique that generates flow-sensitive signal by manipulating the endogenous water spins in the flowing arterial blood (66). The flow contrast in ASL flow-sensitive signal is usually created by a relative inversion between inflowing spins and stationary in-slice nonflowing spins. For example, by acquiring tag and control images, preceded by inflow-magnetization-inversion and inflow-magnetization-noninversion preparation, respectively, the difference between the two reflects only the signal from inflowing magnetization with static magnetization being subtracted out.

Since the flow contrast comes from the freely diffusible water without any contrast agent administration, ASL techniques are safe and repeatable. This property allows multiple (repeated) flow assessments, which could be especially useful for procedures such as thermal therapy treatment where tissue perfusion affects the procedure and may change due to the procedure. For MRI guided high intensity focused ultrasound (MRgHIFU) in particular, the widely used Pennes' bioheat transfer equation (BHTE) is used as the fundamental governing equation to model the effects of heat deposition and dissipation in tissues. The formulation includes terms for thermal conductivity and an effective perfusion, which represents the rate at which blood flow removes heat from a local tissue region. However, tissue properties, particularly perfusion, are known to change over the course of a thermal therapy treatment (67,68). Detecting perfusion changes during a thermal therapy treatment would enable adjustment of treatment parameters to achieve a more efficacious therapy.

After the initial introduction of ASL by Detre and William (66,69), various techniques (70-74) have been developed over the past decade to improve the performance, including pulsed ASL (pASL) which employs short pulses proximal to the imaging slice to label the blood magnetization in the feeding artery. Of the different pASL techniques, flow-sensitive alternating inversion recovery (FAIR) (75) is one of the most frequently used tagging strategies. A FAIR flow-sensitive image is obtained by performing an inversion-recovery sequence twice — once with and once without a slice-selection gradient to label the arterial spins. As a derivative of FAIR, uninverted flow-sensitive alternating inversion recovery (UNFAIR) (76) keeps static signal noninverted in the volume of interest by applying an additional inversion pulse right after the first inversion pulse. A similar technique, called in-plane slice-selective double inversion (IDOL)-prepared ASL, was proposed recently by Jahng *et al.* (77) to minimize the flow-sensitive signal contamination from residual static signal and compensate for potential magnetization transfer (MT) effects. Generally, multiple signal averages are needed to overcome the intrinsic low signal-to-noise ratio (SNR), which has been the major limiting factor that hampers the extensive application of ASL. To overcome this issue, methods involving a Look-Locker-like acquisition following the labeling magnetization preparation to monitor the temporal dynamics of blood inflow have been proposed (78,79). In inflow turbo-sampling (ITS)-FAIR (78), FAIR preparation was combined with Look-Locker image readout by acquiring a series of images after each labeling pulse using echo planar imaging (EPI) readouts. Quantitatively, images at multiple inversion times are required to improve the accuracy of the perfusion quantification, especially for patients with atherosclerosis where the distribution of transit times varies greatly in brain (79). Blood volume could also be estimated using LL-EPI readout as reported by Brookes *et al.* [26].

EPI is the most widely used imaging pulse-sequence to measure cerebral blood flow (CBF) in ASL due to its ability to perform single-shot fast image acquisition and its high SNR for a given imaging time (77). However, artifacts, including susceptibility and Nyquist ghosting, limit its application in imaging other tissues. Other fast imaging sequences such as balanced steady-state free precession (SSFP) and partial-Fourier fast spin echo (FSE) have also been implemented in conjunction with ASL (80). In addition, centric-ordered turbo-FLASH (TFL) imaging readout (77,81,82) has been investigated because of its insensitivity to susceptibility effects and reasonably fast imaging time. Centric-ordered readout has been used (81-83) to obtain the highest weighting in the reconstructed image on the data points at the beginning of the acquisition. In this work, instead of centric ordering, a linear phase encoding scheme (center of k-space being acquired in the midway) is employed to estimate flow velocity.

In addition to obtaining cerebral perfusion parameters for the study of vascular related diseases and functional MRI, the flow-sensitive signal from ASL can also be modeled to obtain quantities that indicate the flow velocity in the tissue of interest (80). The quantification results from various ASL magnetization preparation and modeling schemes should yield, in principle, the same perfusion values because perfusion is a biological parameter. However, as recently reported by Cavusoglu *et al.* (84), the different tagging strategies can result in perfusion measurement variations by as much as 18%. The correspondence between measured and actual perfusion can be limited by several confounding factors, such as transit delay, fluid spin-lattice relaxation time, and flow-sensitive difference signals (85). Moreover, the flow-sensitive difference signals acquired using different imaging parameters or imaging sequences can lead to greater errors if conventional, but inappropriate, flow models are used. Conversely, the quantification process should avoid dependence on imaging sequences or parameters by incorporating the characteristic of the sequences and parameters in the modeling.

ASL has been mostly demonstrated in the brain (73-79), where localized changes in CBF are estimated to study the physiological status of brain tissue. Other *in vivo* applications include cardiac (86), lung (87) and kidney (88) perfusion imaging. Although ASL techniques have been validated extensively in human studies, and some animal studies (81), application to a tissue-mimicking flow phantom with varying flow rates has rarely been performed. To our knowledge, only one paper was published on analytical validation of perfusion imaging on a phantom composed of a syringe filled with plastic beads and small plastic tubes using the Q2TIPS sequence and a kinetic model (89).

In this work, we present a new pulse sequence design that combines TFL imaging and Look-Locker-like (78,79) readout at multiple inversion times in a single scan, and validate the measurements using a hemodialyzer as a tissue-mimicking flow phantom. Taking advantage of multiple images along the inversion recovery curve and using a linear phase-encoding acquisition order for each image, the rate at which flow passes through a point can be determined. The general low SNR of the ASL images will be improved by the higher time-efficiency of the Look-Locker readout strategy. A matching result is found between simulation and flow distribution in the hemodialyzer at varying flowing conditions. A human brain flow velocity mapping was obtained as well.

Theory

Imaging sequence

ASL magnetization preparation is performed using IDOL (77). Specifically, two slice-selective inversion pulses centered on the imaged slice are utilized to invert the spins in the inflowing blood while leaving spins in the slice noninverted. These pulses consist of a global inversion followed by a slice-selective inversion over the imaging slice to achieve spin tagging, see Fig. 4.1(a). For the control scan, two equivalent slice-selective inversion pulses are applied on the imaging slice to compensate for potential MT effects and to leave the static spins noninverted for both tagging and control. The contamination of residual static signal in the resulting difference signal is therefore minimized. As the tagged spins flow into the imaging slice, a sequence of TFL images are acquired separated by a fixed time delay (*TD*). For each TFL image, the k-space phase-encoding lines are acquired with excitation by a train of α excitation pulses. The delay, *TD* is selected as the wait time between each image to allow the washout of the tagged spins that have experienced the excitation pulses from the previous image readout. However, for ultra-slow flow, the *TD* required for complete washout is too long, such that the ASL contrast is diminished by the T_1-recovery process. In this ultra-slow-flow case, the memory from prior pulses needs to be considered for later readouts.

The schematic diagram of (a) the imaging pulse sequence along with (b) the corresponding signal evolution of longitudinal magnetization from both tag and control inflow fluid is presented in Fig. 4.1. In Fig. 4.1 (b), the signal plotted is the normalized longitudinal magnetization at velocities of 10, 20 and 40 mm/s obtained using the simulation parameters: imaging slice thickness = 5mm, *TD* = 200ms, T_1 = 1450ms and flip angle (α) = 15°. After tagging, images are acquired while the inverted flowing magnetization recovers towards the fully relaxed state. Similarly, the control signal evolution due to the excitation RF pulses is demonstrated in Fig. 4.1 (b) as well, with the initial magnetization being fully relaxed. Flow signal differs as a function of velocity because signal saturation depends upon the number of excitation pulses experienced as the magnetization passes through the slice, which in turn depends upon the flow velocity. Fast flow (40mm/s in Fig. 4.1 (b)) guarantees that the initial magnetization originates from the inversion recovery curve; whereas the initial magnetization of ultra-slow flow (10mm/s in Fig. 4.1 (b)) is determined by signal evolution from previous readouts. Under this particular condition, 20mm/s appears to be the critical velocity, above which the memory from the RF pulses from the previous readout need not be considered. The flow information encoded in the train of readout excitation pulses is captured by linear k-space ordering. In Fig. 4.1 (b), a marker is placed in the center of each image readout, at the point where the signal from the center of k-space is acquired with linear phase encoding ordering.

Modeling

With TFL imaging readout, the theoretical expression of the magnetization evolution of the inflowing ASL control and tagging signals are derived based on the Bloch equations. The fluid signal behavior can be modeled by considering the impact of a varying number of α excitation pulses on the freshly inflowing magnetization as a function of flow velocity. Since the number of α excitation pulses experienced by the fluid changes with different flow velocities, the derivation of an expression for the inflow signal provides a model to estimate velocity quantitatively. Mathematically, the effects of excitation pulses on the flow signal in each repetition time (*TR)* are modeled by three processes: excitation, longitudinal magnetization recovery and flow shifting. In the modeling, each slice is subdivided into *K* partitions, where $K = \frac{D}{v \cdot TR}$, *D* is the slice thickness, *v* is the estimated flow velocity, and *TR* is the time interval between the excitation pulses. *K* is therefore the number of RF pulses seen by the spins passing through the slice. For each *TR*, starting with the initial magnetization $M_{z_j}(t_0)$, $j = 1, 2, ..., K,$ the fluid magnetization goes through the following processes:

- At jth excitation

$$M_{z_j}(t_0^+) = M_{z_j}(t_0)\cos\alpha \qquad [4.1]$$

- Magnetization recovery and flow shifting after jth excitation

$$M_{z_{j+1}}(t_0 + TR) = M_{z_j}(t_0^+)E_1 + M_0(1 - E_1) \text{ for j = 2,…,}K \qquad [4.2]$$

$$M_{z_1}(t_0 + TR) = M_{z\_blood}(t_0 + TR)\,,$$

where $E_1 = \exp(-TR/T_{1blood})$, M_0 is the fully relaxed longitudinal magnetization, and $M_{z\_blood}(t)$ is the flow(blood) magnetization outside imaging slice but within the global inversion region, and j is the spatial index of the number of subslices. The routine is then iterated N_y times until all the phase encoding k-space lines are acquired, with image readout time of $N_y \cdot TR$ for each image. The difference between tagging and control signals lies in the expression for the initial magnetization $M_{z_j}(t_0)$, i.e.,

$$M_{z_j}(t_0)\Big|_{tag} = M_0(1 - 2e^{-\frac{t_0}{T1}}) \text{ (tagging)} \qquad [4.3]$$

$$M_{z_j}(t_0)\Big|_{control} = M_0 \text{ (control)} \qquad [4.4]$$

Flow-sensitive signal is obtained by taking the difference of control and tag images, where each signal is formed by averaging from all K subslices.

Because of the existence of fluid exchange between intra- and extra-fiber compartments in a hemodialyzer, which is demonstrated in the simulation, a two-compartment model that provides estimation of the two velocities in the hemodialyzer is developed. Mathematically,

$$S_{ASL} = [S_{\mathrm{intra}}(v_{\mathrm{intra}}) \cdot (1-\eta) + S_{\mathrm{extra}}(v_{\mathrm{extra}}) \cdot \eta] \cdot \sin(\alpha) \qquad [4.5]$$

where S_{intra} and S_{extra} represent the signal of intra- and extra-fiber, respectively, v_{intra} and v_{intra} are the flow velocities in the intra- and extra-fiber, respectively, η is the relative proportion of the extra-fiber compartment, and α is the flip angle.

Methods

Simulations

All the simulations were made and displayed using algorithms developed in Matlab (The MathWorks, Natick, MA, USA). Simulations were performed to assess the behavior of the flow-dependent ASL signal as a function of varying imaging parameters. First of all, the impact of varying flow rates, i.e., K in Eq. [4.1-2], on inflowing tag and control signals was studied. Signal evolution of longitudinal magnetization of flowing spins were simulated at three flow rates ranging from 20 mm/s to 60 mm/s. The simulation imaging parameter were TR = 3 ms, α = 15°, TD = 200 ms, N_y = 64, $T_{1blood}\big|_{3T}$ = 1.45 s, slice thickness = 5 mm, number of images along the curve = 8. The ASL signal was then obtained as the difference between control and tag signals. The impacts of different parameters, such as α in Eq. [4.1] and T_1 in Eq. [4.2] on resulting flow-sensitive signals were explored. To determine the effects of α, signals corresponding to four α *'s* varying from 5° to 20° were simulated at the flow velocity of 40mm/s and 120mm/s. The remaining parameters were kept the same as the previous simulation. Similarly, the flow-sensitive signal evolutions were simulated at four T_1 ranging from 500ms to 2000ms. Furthermore, the sensitivity of the flow-sensitive ASL signal to varying flow velocity was further visualized as a function of inversion time (*TI*), and a comparison to the actual hemodialyzer experimental results was presented. Based on the simulations, optimal parameters can be selected to maximize the flow signals of the hemodialyzer and *in vivo* experiments.

Hemodialyzer imaging

A hemodialyzer, which has thousands of fibers, each with a diameter on the order of hundreds of microns, has properties that may be useful in mimicking human tissue flow and can be tested with a wide range of flow rates. In this study, all images were acquired on a Siemens MAGNETOM TIM Trio 3 T MRI scanner with 40 mT/m gradients and a slew rate of 200 mT/m/ms. A commercially available hemodialyzer (Baxter Xenium-190) with Gd-BOPTA water pumped through the fibers unidirectionally was imaged using a 12-channel head coil (Siemens, Erlangen, Germany). To validate the complete cancellation of static signal between tag and control, a static water phantom was set next to the dialyzer and imaged in the same field of view. A nonpulsatile pump circulated doped water (T_1 = 1.45 s) at pumping rates of [45, 90, 135, 180] cc/min through the semipermeable fibers in the hemodialyzer. Using the proposed imaging sequence, single-slice 2D transversal images of the hemodialyzer were acquired at a series of *TI* = [200, 600, 1000, 1400, 1800, 2200, 2600, 3000] ms in one scan with the following parameters: TR = 3 ms, α =15°, TD = 200ms, voxel size = 3.1x3.1x5 mm^3. Tagging and control scans were interleaved. Furthermore, a leading edge method was used to estimate the flow rates within the hemodialyzer by measuring the leading edge of the fluid as a function of *TI*. A single coronal slice was acquired using the same pulse sequence to validate the quantification result. Two 180° hyperbolic-secant adiabatic inversion pulses with duration of 20 ms were used for tagging and control preparation. To avoid any contamination from imperfection in the inversion pulse slice profile, 4.5 mm extra inversion thickness on each side was applied on the imaging slice in the IDOL preparation. A region of interest (ROI) was drawn over the hemodialyzer cross-sectional flow-sensitive image at each *TI* to obtain an averaged ASL signal.

The resulting flow-sensitive ASL time series data were input into a nonlinear least-squares fitting routine written in Matlab. The model could provide simultaneous estimation of both flow velocities for the intra- and extra-fiber compartments in a single measurement. A comparison of simulation and experiment was made to indicate that the flow velocities in the two compartments are different. It was shown that the hemodialyzer cross-section is composed of 30% intrafiber area and 70% extrafiber area. Therefore, an averaged velocity can be determined based on the estimated intra- and extra-fiber velocities.

In vivo imaging

This study was approved by the institutional review board. One healthy subject was imaged using the same pulse sequence at a series of *TI* = [700, 1000, 1300, 1600, 1900, 2200]ms in a single scan. Single-slice 2D transversal images of the brain were scanned with the following imaging parameters: TR = 3ms, α = 15°, matrix size = 128x128, pixel size = 2x2x3.5 mm^3, BW = 490 Hz/Px, tagging thickness = 10mm. The imaging slice was located at the corpus callosum while the tagging of the inflow was centered on the neck so that the heart was included in the inversion region. An 8 second time interval was introduced between the interleaved tag/control scans to avoid any impact from previous pulses. Altogether, four measurements of tag/control pairs were acquired in 1 minute. Pair-wise subtraction between tagging and control images was performed to obtain the averaged flow-sensitive images. In addition, a nonlinear least-squares fitting routine was applied to the measured data series of difference signals to estimate flow velocities. An estimate of fully relaxed magnetization of arterial blood M_0 is obtained by acquiring a proton density-weighted (PD-w) gradient echo sequence with TR = 3000ms and TE = 8ms, and a correction for proton density and relaxation rate of gray matter was applied (19). A literature T_1 value of blood 1684ms (19) is used in the modeling.

Results

Simulation

Fig. 4.2 illustrates the normalized longitudinal magnetization evolution of inflowing tag and control signals at three flow velocities with the assumption of the lowest velocity being fast enough that each time the imaging starts with freshly inflowing spins. It is clear that the inversion recovery of tagging magnetization and the non-inverted control magnetization are the source of the contrast. As the flow rate changes, the impact of the series of α excitation pulses on the inflowing spins is visualized as different trajectories corresponding to different velocities. The tag signal of the lower velocity tends to deviate further from the inversion recovery curve, while the tag signal of the faster velocity tends to eventually stay closer to the inversion recovery curve. In other words, spins with higher flow rate are less affected by the excitation pulse train than those with a slower flow rate since fast moving spins experience fewer excitation pulses. A similar situation is found for the control signals. This flow-dependency property of the signal is the principal foundation of the proposed technique.

The effect of α on flow-sensitive signal is demonstrated in Fig. 4.3. At extra-fiber velocities of 40 mm/s and 120 mm/s, the maximum ASL signal is achieved at α of 10° and 15°, respectively. It is evident that the optimal α varies as a function of velocity. In Fig. 4.4, normalized flow-sensitive signal with different T_1 are shown. The normalized flow-sensitive signal increases as T_1 increases accordingly, which demonstrates that the ASL signal gains as T_1 lengthens. This indicates that the ASL signal could benefit from a higher magnetic field.

Hemodialyzer imaging

Images from a transverse slice of the hemodialyzer and static water phantom acquired at TI = [200, 600, 1000, 1400, 1800, 2200, 2600, 3000]ms are shown in Fig. 4.5. Tag, control and difference images are represented in the top, middle and bottom rows, respectively. Within each image, the largest area corresponds to the cross-section of the static water phantom; the cross-section of the hemodialyzer with flow into the magnet bore is located at the upper left corner, while the cross-section of the thin tubing with fluid flowing out of the magnet bore appears in the upper right of each image. The complete cancellation of static signal shown in the bottom row indicates that the ASL signal shown is purely flow-dependent. The general signal drop off within the hemodialyzer indicates that the flow direction in the hemodialyzer is from left to right in the figure. The flow is in the opposite direction in the thin tubing.

To estimate flow velocity, the ROI-based averaged signal intensities from the cross-section of the hemodialyzer were evaluated and are shown in Fig. 4.6 as solid lines. The signals show an approximately proportional relationship to the corresponding pumping rates. Compared to the simulated ASL signal (dashed lines), the simulations agree reasonably well with the experimental results except for the initial signal increment. Since a distance was introduced between the tagging and imaging regions to minimize the effect of imperfect inversion near the edges, the signal drop in the initial period is believed to be caused by the incomplete inflow of tagged spins.

In Fig. 4.7, curve fitting on the experimental signals plotted in Fig. 4.8 are presented. The initial three data points were excluded from the fitting to avoid the influence from incomplete inflow. Corresponding to the four pumping rates [45, 90, 135, 180] cc/min, the estimated flow velocities for the intra- and extra-compartment are [5.00, 11.36, 17.90, 22.68] mm/s and [0.13, 0.23, 0.47, 0.80] mm/s, respectively. Therefore, the averaged flow velocities are [1.59, 3.57, 5.69, 7.36] mm/s.

To validate the results, images from a coronal slice of the hemodialyzer and static water phantom acquired at TI = [500, 1000, 1500, 2000, 2500, 3000, 5000] ms are shown in Fig. 4.8. Tag, control and difference images are represented in the top, middle and bottom rows, respectively. Within each image, the largest area corresponds to the coronal view of the static water phantom; the coronal views of the hemodialyzer and thin tube are located to the left and right of the static water phantom, respectively. A linear curve fitting of the progression of the front edge of fluid in the hemodialyzer as a function of *TI* provide a way to estimate the flow velocity.

The calculated values using the two methods, transverse slice with Bloch-equation-based modeling and coronal slice with leading edge velocity modeling, are listed in Table 4.1. A matched estimation on averaged velocities at four flow rates is found between the two methods. The greater deviation in matches at comparatively lower flow rates could be caused by the invalid assumption of plug flow in the hemodialyzer and the saturation of Look-locker readouts.

In vivo imaging

Flow-sensitive images at one slice location acquired at *TI* of [700, 1000, 1300, 1600, 1900, 2200] ms are shown in Fig. 4.9. The wash-out of bolus is visible as *TI* increases. The large vein located at the bottom (red circle) appears bright because the venous blood is labeled in IDOL tagging schemes.

The fitted velocity mapping is shown in Fig. 4.10. A higher velocity is found in the superior sagittal sinus (SS) and slower velocities can be seen in gray matters. The flow mapping in Fig. 4.10 is scaled to the range of 0–5 to emphasize the signal at lower flow rates. The ROI based flow rates estimation of gray matter, white matter and sagittal sinus are 2.04, 0.89 and 22.09 mm/s, respectively. The flow velocity in the SS is lower than the velocity reported by others (27). This is because IDOL preparation was used where both artery and venous blood were tagged. The accuracy of flow quantification in the veins drops due to the fact that the tagged blood passing through the imaging slice has time to enter the SS and pass again through the imaging slice during the ASL measurements. The signal from this twice-imaged blood is saturated and results in an error in the flow measurement.

Discussion

In this paper, we have presented the theory as well as simulation and experimental verification of a quantitative method to measure through-slice flow velocity using multiple TFL image readouts after IDOL preparation of a single slice. By using linear k-space ordering in the TFL images, the image intensities are a function of the local flow dynamics coupled with the IDOL tagging or control magnetization preparation. Through-plane flow assessment is achieved through Bloch equation modeling. Fitting the signal intensities in these multiple images provides an intrinsic decrease in measurement noise.

Computer simulations based on the Bloch equations, designed to model the situation of unidirectional flow in a hemodialyzer, demonstrated that the ASL signals are sequence parameter-dependent. The characteristic of the sequences and parameters were incorporated in the quantification modeling. Flow experiments were performed with the hemodialyzer and consistently matched values were found between the simulation and the hemodialyzer experiments.

The hemodialyzer and human brain MR images acquired using the proposed novel TFL-based imaging pulse sequence suggest that our technique could yield fairly accurate through-plane fluid flow estimation. De to the two-compartment flow distribution in the hemodialyzer, phase contrast (PC) flow velocity measurement was not considered to be a feasible flow quantification technique in our study scenario. It is therefore, not likely that PC flow measurements would be accurate, but would instead be biased by partial volume artifacts.

Certain assumptions and limitations apply to the quantification process involved in this study. Only the flow passing into and out of the imaged slice could provide measurable signal. Thus, for the case where flowing magnetization remains in the imaging slice, the method could possibly introduce errors by underestimating the flow. In addition, the net fluid passing through the thin slice in the hemodialyzer is assumed to be plug flow instead of laminar flow. This could explain the imperfect match between the two methods at slower flow rates of 45cc/min and 90cc/min as listed in Table 4.1. Other potential error sources include deviations between the desired and actual flip angle, imperfections at the edges of the inversion pulses, and the general variation in the tag and control signals during image acquisition.

Although only single-slice imaging was used in this study, the fact that multiple acquisitions of the single slice are acquired during a single tagging (or control) makes the technique relatively efficient. This could easily be extended to multiple slices by serial acquisitions. At the same time, SNR can be improved by increasing the number of pairs of tag-control image sequences acquired. For example, the brain images shown were based on averages over four repetitions, and more repetitions will lead to a higher SNR.

As implemented, this technique was designed to assess all flow passing through the slice, including vessels of all sizes down to capillary beds unlike other techniques that use a preacquisition spoiler gradient pulse to suppress the flow signal from large vessels. By including all types of flow through the slice, the perfusion value obtained with this technique should match the perfusion term used in the Pennes' BHTE. It is possible that thermal therapy techniques, such as MRgHIFU could use measurements from this newly developed imaging technique in thermal modeling based on the Pennes' equation. Since the goal is to estimate the Pennes' perfusion term which depends on what carries heat outside the heated volume, the flow assessment on the feeding arteries and veins are desirable in this scenario. This method is independent of MR thermometry, decoupling the blood flow measurement from the MR temperature maps, allowing the perfusion changes to be monitored throughout the thermal therapy session. Currently, we are only showing blood flow in brain. The existence of the blood brain barrier makes the blood transfer time between the vasculature and the tissue longer. In other words, the flow could be captured before the tagged spins in the tissue become saturated by the excitation pulse trains. This application might become limited when extending to flow assessment in other tissues, e.g., kidney, liver etc.

Further investigation including more subjects is necessary. The tradeoff between the image acquisition time and the accuracy of flow rate quantification needs to be optimized such that the scan could be interleaved in an actual MRgHIFU study. When dealing with flow quantification and modeling, the distribution of static and flowing spins within each voxel and how flow-sensitive signal changes as velocity varies are two important aspects that need to be addressed. In this work, velocity dependence of flow signal is obtained with linear phase encoding ordering. In the future, by modifying the timing of the acquisition of k-space center to be centric-ordering, the blood flow distribution of perfusion signal can be obtained.

Conclusions

Multiple-image readout after a single ASL preparation, along with the linear acquisition ordering in the phase encoding direction in TFL imaging enable estimation of through-plane flow. The experiments provide evidence that the proposed pulse sequence design is able to measure the average velocity of fluid flowing through the image plane. Accuracy is decreased for venous blood that passes through and returns to the imaging slice during the time between tagging and signal readout. This measurement provides an estimate of total fluid flow when the voxel fraction of static magnetization is known.

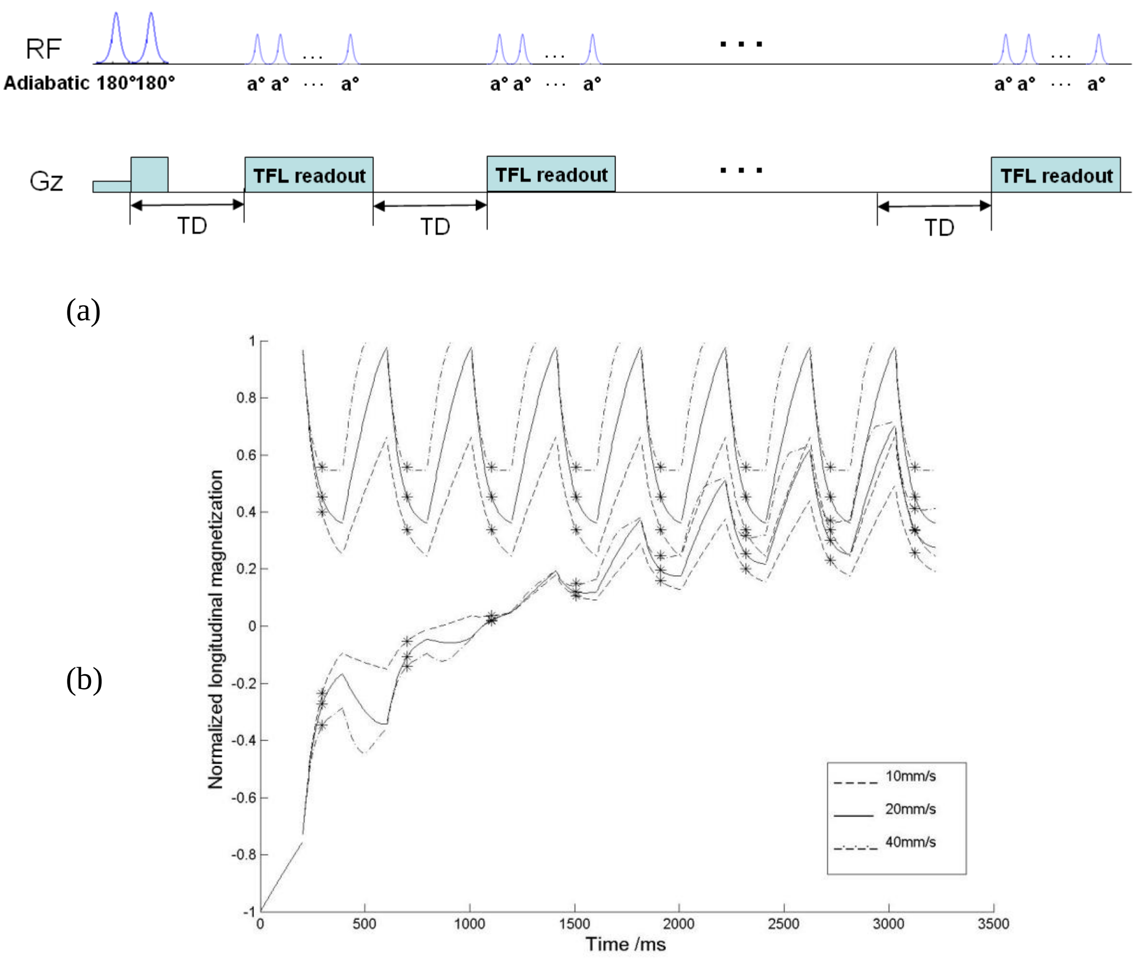

Figure 4.1. Schematic diagrams of the tagging imaging pulse sequence along with the evolution of the longitudinal magnetization of tag and control inflowing fluid. (a) IDOL tagging inversion is followed by a series of TFL image readouts. Depending on the fluid (blood) T_1, *TD* and the number of images acquired along the curve can be adjusted. (b) Longitudinal magnetization of tag (bottom lines) and control (top lines) inflowing fluid. With the simulation parameters: imaging slice thickness = 5mm, Time Delay (TD) = 200ms, T_1 = 1450ms and flip angle = 15°, fast flow 40mm/s (dash dotted line) guarantees the initial magnetization originates from the inversion recovery curve; whereas the initial magnetization of slow flow 10 mm/s (dashed line) must incorporate the signal evolution from previous readouts. For these parameters, 20 mm/s (solid line) seems to be the critical velocity below which the impact of preceding readout pulses needs to be taken into account. Eight images are acquired after each single ASL preparation. A marker is indicated at the point where the signal from the center of k-space is acquired with linear phase encoding ordering.

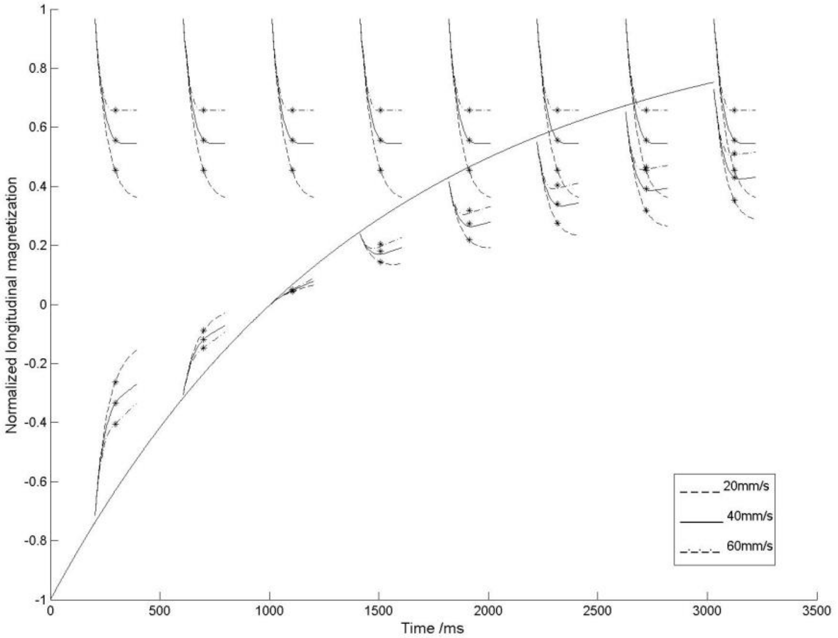

Figure 4.2. Evolution of longitudinal magnetization for tagging (bottom lines) and control (top lines) scans, respectively. The simulation parameters were TR=3ms, α=15°, TD=200ms, Ny=64, T_1=1.45s, slice thickness=5mm, matrix size=64x64, number of images along the curve=8. At each TI, three velocities, [20, 40, 60] mm/s were simulated. The case with highest velocity stays closest to the main magnetization curve, while the flow with the lowest velocity deviates further away from the main magnetization curve. It is assumed that the lowest velocity being fast enough, that each time the imaging starts with freshly inflowing spins.

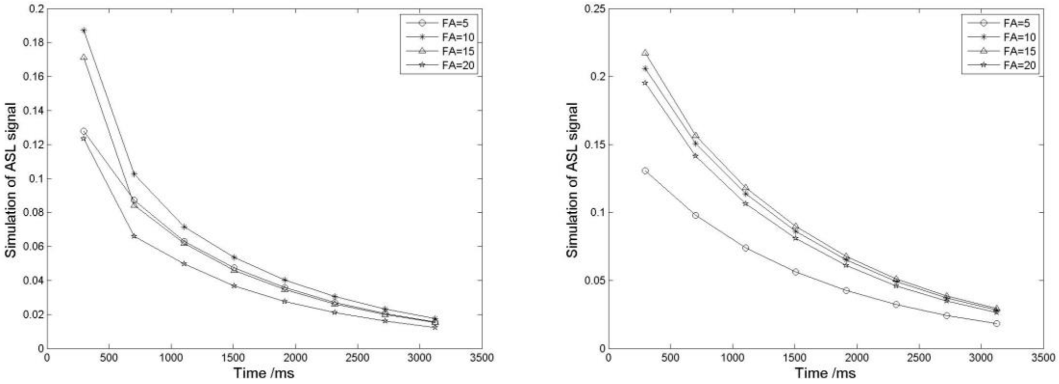

(a) (b)

Figure 4.3. Simulation of normalized flow-sensitive signals at an extra-fiber velocity of (a) 40mm/s and (b) 120mm/s. The maximum flow signal is achieved at α of 10° and 15°, respectively. The rest of the parameters were kept the same as in Fig. 4.2. At different flow velocities, α can be adjusted to obtain the maximum flow-sensitive signal.

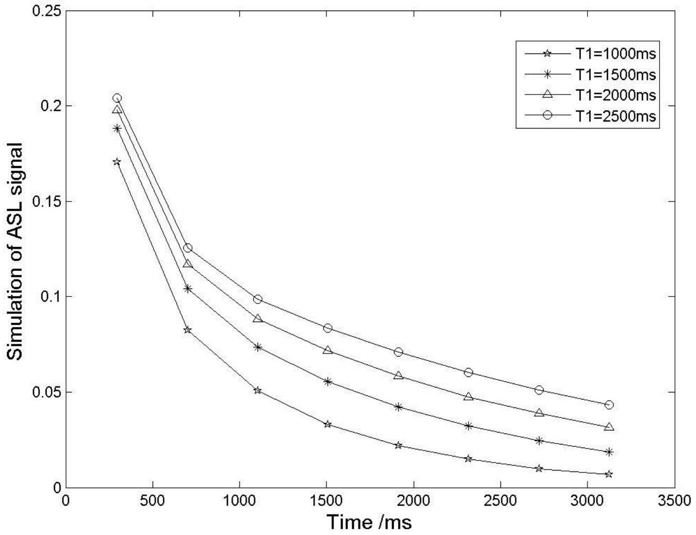

Figure 4.4. Simulated flow-sensitive signals as a function of fluid spin-lattice relaxation time T_1 = [1000, 1500, 2000, 2500]ms. Using the same parameters, maximum flow-sensitive signal for an extra-fiber flow velocity of 40mm/s & 4mm/s , α =10° is achieved at T_1 of 1450ms.

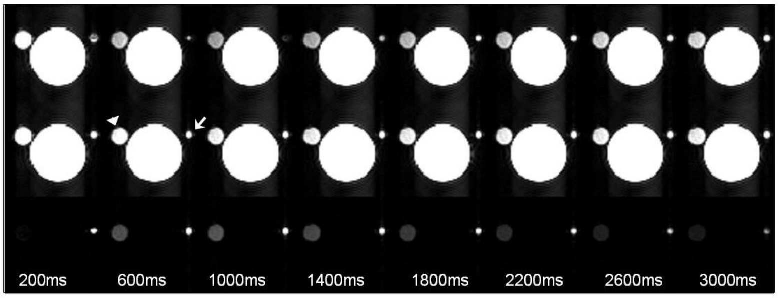

Figure 4.5. Representative eight single-slice images acquired at [200, 600, 1000, 1400, 1800, 2200, 2600, 3000]ms after the ASL magnetization inversion with a pumping rate of 200cc/min. Three rows correspond to tag (upper row), control (middle row), and difference (lower row) images. Within each image, cross-sections of a Siemens water phantom (biggest cross-section), the hemodialyzer (arrow head) and thin tube (arrow) are depicted. Static water signals cancel out completely in the flow-sensitive difference images. The dialyzer signal cancels in the first image because it took longer than 200ms for the tagged flow to enter the imaged slice.

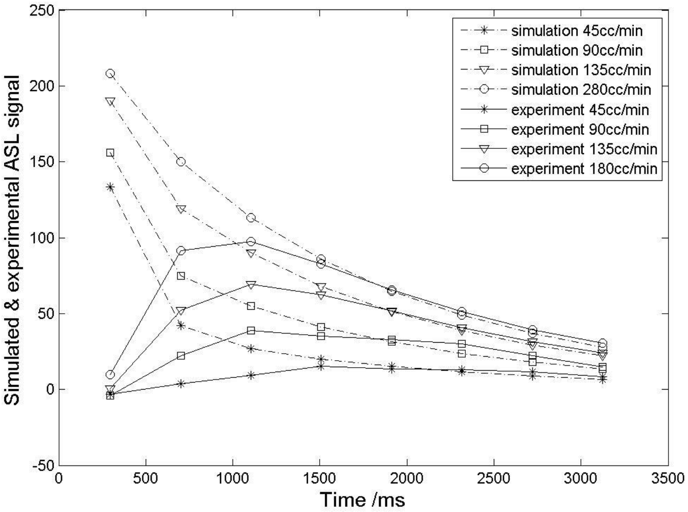

Figure 4.6. Comparison of simulated ASL signal (dashed lines) and experimental results (solid lines). Experimental flow-sensitive signals were averaged over the cross-sections of hemodialyzer at four pumping rates [45, 90, 135, 180] cc/min at a *TD* of 200ms and α of 15°. Simulated flow-sensitive signal is calculated as the difference of control and tagging signal (see Fig. 4.2) using the same parameters as in the experiment. Overall there is a reasonably good agreement between the two and the only discrepancy lies in the initial signal increment which is due to the incomplete inflow of tagged spins.

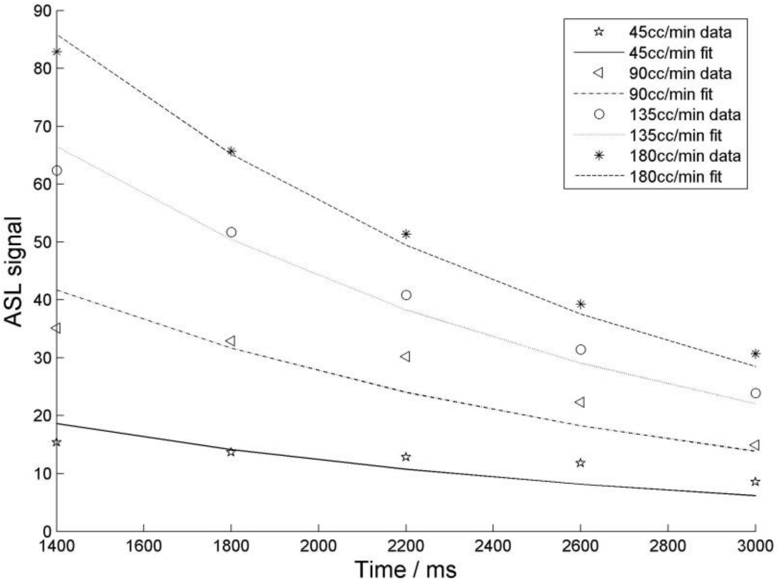

Figure 4.7. Curve fittings at four pumping rates [45, 90, 135, 180] cc/min from two-compartment fitting. The resulting averaged velocities are [1.59, 3.57, 5.69, 7.36] mm/s, respectively. The calculated correlation coefficient between the data and the fitting does decrease as the flow rates decrease.

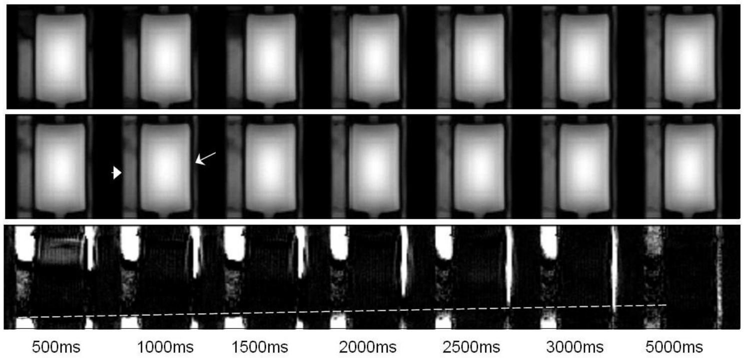

Figure 4.8. Representative coronal single-slice images acquired at [500, 1000, 1500, 2000, 2500, 3000, 5000]ms after the ASL magnetization inversion at a pumping rate of 180cc/min. Three rows correspond to tag (upper row), control (middle row), and difference (lower row) images. Within each image, coronal views of a Siemens water phantom (largest area), the hemodialyzer (arrow head) and thin tube (arrow) are depicted. The progression of the front edge of fluid in hemodialyzer as *TI* increases (dashed line) provides a way to estimate the flow velocity, as presented by the dotted line.

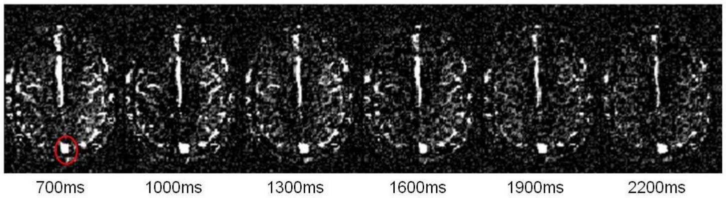

Figure 4.9. Flow-sensitive images acquired at *TI* of [700, 1000, 1300, 1600, 1900, 2200]ms. Bolus wash-out is visible as *TI* increases. The superior sagittal sinus located at the bottom (red circle) appears bright because the venous blood is labeled in IDOL tagging schemes.

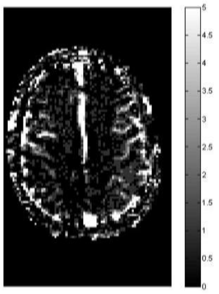

Figure 4.10. Brain velocity mapping (unit: mm/s). A high velocity is found in the superior sagittal sinus and slower velocities can be seen in gray matter.

Table 4. 1 Flow velocity estimation

Flow rate	Intra-fiber velocity	Extra-fiber velocity	Fitting correlation coefficient	**Average velocity**	**Leading edge velocity**
45cc/min	5.00	0.13	0.863	1.59	1.3
90cc/min	11.36	0.23	0.834	3.57	1.7
135cc/min	17.90	0.47	0.990	5.69	5.0
180cc/min	22.68	0.80	0.998	7.36	7.5

Estimated flow velocity at four pumping rates [45, 90, 135, 180] cc/min from two-compartment fitting using Bloch equation and leading edge velocity modeling. (Unit: mm/s)

CHAPTER 5

BREAST MR ANGIOGRAPHY USING TWO-POINT DIXON SSFP

Introduction

Magnetic resonance angiography (MRA) is a noninvasive imaging technique for visualizing the blood vascular system (90,91). It has been applied throughout the body by identifying vessel abnormalities and assisting in the diagnosis of the vascular diseases. In addition, information on blood vessel anatomy, such as locations and flow rates, can also be important for thermal therapy. The association of increasing vascularity and the development of breast cancer has been demonstrated using breast dynamic contrast enhanced (DCE)-MRA studies (92,93). However, there have been limited studies on noncontrast-enhanced (NCE) breast MRA (94,95). This chapter focuses on developing a NCE MRA technique for visualizing blood vessel in the breast to assist in magnetic resonance guided high-intensity focused ultrasound (MRgHIFU) therapy for the breast.

Breast MRA can be achieved with and without the injection of contrast agent. Clinically, intravenous injection of T_1-shortening contrast agent is commonly used to help boost MR signal of blood (96). Concerns about nephrogenic systemic fibrosis associated with contrast agent injection, especially for patients in renal failure, has led to increased attention in developing NCE MRA techniques (80). Because blood vessels in the breast, like other peripheral vessels, are characterized by lower flow rates and thinner blood vessels (97), flow-independent peripheral imaging technique (98,99) that use intrinsic MR properties becomes an appropriate option for the breast MRA.

Initial results on NCE breast MRA have been reported by Miyasaki (94) and Saranathan *et al.* (95). In the work of Miyasaki *et al.*, a peripheral pulse triggered inversion prepared half-Fourier turbo spin echo (TSE) sequence is used to image blood vessels in the breast. The progression of blood inflow as a function of inversion time was shown using chemical selective pulses for fat suppression. Saranathan *et al.* (95) compared breast MIP images using a dual-echo balanced steady state free precession (SSFP) sequence to those obtained using TSE sequences. In the same imaging time, more blood vessel details were found from SSFP images because of its greater acquisition efficiency.

Fat suppression/separation plays an important role in visualizing blood vessel in breast MRA. The unique T_2/T_1 contrast of SSFP causes tissue with high T_2/T_1, e.g., blood and fat, to appear hyper-intense. High blood signal is favorable in blood vessel visualization; however, bright fat signal needs to be suppressed to uncover information that might otherwise be obscured by fat, e.g., breast lesions and blood vessels. Taking advantage of the in-phase and out-of-phase signal characteristics at various echo times (TE), fat and water signal can be separated using multipoint Dixon techniques (100-102). Compared to other fat suppression techniques, Dixon methods not only offer robust water-only images in the presence of B_0 and B_1 inhomogeneity, quantified information on fat also has diagnostic value for diseases, such as diabetes and obesity (103).

In this chapter, fat-water separation using 3D dual-echo SSFP sequences are broadly investigated. Simulation of the in-phase and out-of-phase signal for both fat and fibroglandular tissues are performed, from which imaging parameters are obtained and applied to phantom, *ex vivo* pork and *in vivo* breast imaging. In particular, 3D dual-echo SSFP sequence designs with variations in the readout gradients are examined. Comparisons among results from the two-point Dixon fat-water separation are made for all the pulse sequences. Issues including the *k*-space misalignment, bidirectional chemical shift induced misregistration, motion created by the imaging sequence and the image acquisition time are considered.

Theory

In this section, the two-point Dixon method for fat water separation is reviewed. Details on the three-point method can be found elsewhere (102). Various methods for implementing the two-point Dixon method in an SSFP sequence are also presented.

Two-point Dixon fat-water separation

Relying on the phase shifts created by fat-water resonance frequency differences, the two-point Dixon technique separates water from fat in the presence of field inhomogeneity. Specifically, two acquisitions, one with TE chosen to have fat and water in-phase (0-image) and another with *TE* chosen to have fat and water out-of-phase (π-image), are performed and combined to obtain water-only and fat-only images. Supposedly, the only phase difference accumulated between the two acquisitions is due to the chemical shift. However, in reality, many other sources can also contribute to the phase shifts. These factors include the inhomogeneous penetration of the RF pulses, unknown spatial dependent phase shifts associated with the magnetic field inhomogeneity and other system imperfection (100). Mathematically, the in-phase I_1 and out-of-phase I_2 signal can be expressed as:

$$\begin{aligned} I_1 &= (W + Fe^{-2\pi\Delta f_{cs}t_1})e^{-i\phi_0} \\ I_2 &= (W + Fe^{-2\pi\Delta f_{cs}t_2})e^{-\frac{t_2-t_1}{T_2^{'}}}e^{-i(\phi_0+\phi\ )} \end{aligned} \qquad [5.1]$$

where ϕ_0 is a constant spatially dependent phase error due to the RF field inhomogeneity and other system imperfections, ϕ is the phase shift for a pixel caused by the local field inhomogeneity, and $T_2^{'}$ is the field inhomogeneity loss component of T_2^* (see Eq. [2.29]). Ignoring T_2^* decay and choosing the timing of the image acquisition following the relationships

$$\begin{aligned} 2\pi\Delta f_{cs}t_1 &= 2n \cdot \pi \\ 2\pi\Delta f_{cs}t_2 &= (2m+1) \cdot \pi \end{aligned} \qquad n,m = 1,2,\ldots \qquad [5.2]$$

allows for simplification of Eq. [5.1]:

$$\begin{aligned} I_1 &= (W + F)e^{-i\phi_0} \\ I_2 &= (W - F)e^{-i(\phi_0+\phi)} \end{aligned} \qquad [5.3]$$

In Eq. [5.3], the four unknowns *W*, *F*, ϕ_0 and ϕ can be solved based on the two complex measurements I_1 and I_2. Specifically, the phase term ϕ can be calculated by the following relationship

$$\phi = \frac{1}{2} Arg[(I_1^* I_2)^2] \qquad [5.4]$$

Even though the prediction of whether a pixel is water or fat dominant is usually difficult, the ambiguity in the sign of I_2 can be resolved by squaring $I_1^* I_2$, as given in Eq. [5.4]. Further, because the phase shift ϕ is not restricted to the interval of 2π, a phase unwrapping procedure is therefore necessary to correct for 2π phase jumps. A method based on Poisson equation proposed by Moon-Ho Song *et al.* (104) was used in our reconstruction algorithm. This phase unwrapping strategy has the advantages of robust performance and no initial seed point is required. After the phase unwrapping step, followed by halving by two, the estimated phase map ϕ can be used to simplify Eq. [5.3]:

$$\begin{aligned} I_1 &= (W + F)e^{-i\phi_0} \\ I_2 e^{i\phi} &= (W - F)e^{-i\phi_0} \end{aligned} \qquad [5.5]$$

Rearranging Eq. [5.5], expressions for *W* and *F* are obtained:

$$\begin{aligned} W &= \left| \frac{I_1 + I_2 e^{i\phi}}{2} \right| \\ F &= \left| \frac{I_1 - I_2 e^{i\phi}}{2} \right| \end{aligned} \qquad [5.6]$$

Bipolar readout gradient

Multi-echo acquisition in a single *TR* is an efficient image readout method for Dixon-based fat-water separation. Two echoes required for the two-point Dixon fat-water separation can be acquired using a bipolar gradient — switching gradient polarity between the multi-echo readout in each *TR*. Advantages of the bipolar gradient include shorter scan time, higher SNR efficiency, more robust field map estimation and reduced motion-induced artifacts (105).

Challenges associated with the bipolar readout gradient include *k*-space misalignment and bidirectional chemical shift. Specifically, *k*-space misalignment between the two echoes causes a linear phase error in the in-phase and out-of-phase difference image, which affects the field map estimation and fat-water separation (106). In addition, in the two echoes acquired using the bipolar gradient, the opposite polarity of the readout gradients leads to chemical shift in opposite directions, as graphically demonstrated in Fig. 5.1.

TR/TE selection

The amplitude of SSFP signal varies periodically as a function of offset frequency, with a period of 1/TR. To successfully separate fat from water signal, reasonable amount of signals from both chemical components are required in the Dixon source images. The criteria for choosing TR should follows the relationship

$$TR = n / \Delta f_{cs} \qquad [5.7]$$

where n is an integer greater than zero. Given $\Delta f_{cs} = 420$Hz at 3T, TR of 2.3, 4.5, 6.8, …ms guarantee that both fat and water signal are acquired at its maximum signal amplitude. The magnitude and phase of SSFP signal depend on the phase accumulated during each TR due to magnetic field inhomogeneity. As discussed in Section 2.5.3, a prolonged TR can aggravate the banding artifacts.

Criteria for selection of TE are obtained by rearranging Eq. [5.2]:

$$\begin{aligned} TE_1 &= \frac{n}{\Delta f_{cs}} \\ TE_2 &= \frac{2n+1}{\Delta f_{cs}} \end{aligned} \qquad [5.8]$$

The in-phase and out-of-phase signals can be acquired at TE_1 and TE_2, respectively. Given $\Delta f_{cs} = 420$Hz at 3T, TE_1 = 0, 2.3, 4.6, 6.9, …ms, and TE_2 = 1.2, 3.5, 5.8, 8.1, …ms.

Methods

Pulse sequence design

As discussed in Section 5.2.2, higher signal efficiency can be achieved with bipolar readout gradient in the multi-echo acquisitions. However, issues associated with the bipolar readout, such as *k*-space misalignment and chemical shift induced misregistration, need to be addressed. In this study, four variations of the 3D SSFP sequence for two-point Dixon are designed, and their performances in fat-water separation are examined. First is single-echo readout in each TR. The in-phase and out-of-phase images are acquired in two separate scans at different TEs. A pulse sequence diagram is demonstrated in Fig. 2.10. Second is dual-echo readout with a bipolar gradient polarity. The in-phase and out-of-phase images are acquired at different TEs in a single TR, as illustrated in Fig. 5.2. Third is dual-echo readout with alternating bipolar gradient polarity in adjacent TR, as shown in Fig. 5.3. Two sets of in-phase and out-of-phase images are acquired in total. To reconstruct fat-only and water-only images, in-phase images from one TR are combined with out-of-phase images from the adjacent TR. Finally is a complete acquisition with dual-echo bipolar readout gradients, followed by a complete acquisition with dual-echo bipolar readout bipolar gradients with the opposite polarity. Similar to sequence 3, two sets of in-phase and out-of-phase images are acquired in total. The only difference between sequence 3 and 4 resides in whether the bipolar readout gradients with opposite polarities are interleaved or not.

Simulations

In-phase and out-of-phase SSFP signals for both fat and fibroglandular tissues were simulated. Specifically, the amplitude of the SSFP signal was simulated at TR = 5.7 and 6.8ms, and FA = [10°, 30°, 50°, 70°, 90°] to study how sensitive the steady state signal is to TR and FA. In addition, the phase of the SSFP signal at $TE_1/TE_2 = 2.3/3.4$ms was also simulated to confirm the in-phase and out-of-phase condition required in the two-point Dixon reconstruction. In the simulation, T_1/T_2 for fat and fibroglandular tissue was set to be 423/154 and 1680/71ms, respectively (107). Imaging parameters yielding the highest water signal were chosen for the following phantom, *ex vivo* and *in vivo* imaging experiments.

Phantom imaging

All the phantom, *ex vivo*, and *in vivo* imaging were performed on a 3T TIM Trio MRI scanner (Siemens Ag, Erlangen, Germany). First, as shown in Fig. 5.4 (a), two bottles each filled with pure vegetable oil and water were used to investigate the effect of *k*-space misalignment and chemical-shift induced misregistration of a bipolar readout. The phantoms were imaged in the same field of view (FOV) using sequences 2 and 3. Further, five vials with varying concentration of mayonnaises were mixed in water to obtain concentrations of 20%, 40%, 60%, 80% and 100% mayonnaises. The sixth vial was filled with pure vegetable oil. All the vials were then placed in a pure water bath, as demonstrated in Fig. 5.4 (b). All four sequence designs were tested on this phantom with the following imaging parameters: TR = 6.8ms, TE_1/TE_2 = 2.3/3.4ms, FA =30°, FOV = 200x200 mm, matrix size = 192x192, 16 slices, slice thickness = 2mm, and BW = 800Hz/Px.

Ex vivo pork imaging

Sequences 1, 2 and 4 were examined on an *ex vivo* pork sample, imaged using a 11-channel RF coil (108) designed for the breast MRgHIFU treatment (109). The effects of FA and the acceleration factor, generalized autocalibrating partially parallel acquisition (GRAPPA), were studied by imaging at FA = [10°, 30°, 50°, 70°] and GRAPPA factor = [1, 2, 3, 4]. Further, the performances of fat-water separation from SSFP-based two-point Dixon and GRE-based three-point Dixon were compared. In SSFP, TR = 6.8ms, and TE_1/TE_2 = 2.3/3.4ms; for GRE imaging, TR = 11ms, and $TE_1/TE_2/TE_3$ = 4.7/5.75/6.8ms. Other common imaging parameters are FOV = 160x160 mm, matrix size

= 128x128, 32 slices, slice thickness = 1mm, leading to a voxel size of 0.9x0.9.x1mm^3.

In vivo imaging

With informed consent obtained from the volunteers, four subjects (three healthy subjects and one subject with fibroadenoma) were examined in air or water using the Siemens 4-channel breast coil or the 11-channel RF coil designed specifically for breast MRgHIFU. Images from all four subjects were acquired using sequence 2 (Fig. 5.2). In addition, sequences 1, 3, and 4 were also applied on one healthy volunteer. The unilateral imaging protocols were as follows: $TR/TE_1/TE_2$ = 6.8/2.3/3.4 ms, FA=30°, matrix size = 192x192x72–192x192x104, FOV = 168x168x108–287x287x120 mm^3, BW = 766–1530 Hz/Px, giving an in plane pixel size of 0.9x0.9x1.5–1.5x1.5x1.5 mm^2. The image acquisition time was 2–4 minutes without any acceleration, and the asymmetric echo was turned on for partial readout acquisition to achieve the desired TE. Thin-slab MIP of the water-only images was used for blood vessels visualization. To improve the image visual appearance, zero filled interpolation (ZFI) by a factor of two was performed on all the images before the two-point Dixon reconstruction, resulting in a voxel spacing of 0.45x0.45x0.75mm^3 – 0.75x0.75x0.75mm^3.

Results

Simulations

Fig. 5.5 (a) and Fig. 5.5 (b) show the simulated SSFP magnitude signal at TR = 5.7 and 6.8ms, respectively, for both fat and fibroglandular tissue. It is observed that, at TR = 5.7ms, the signal of fibroglandular tissue reaches maximum when fat is at its minimum. On the other hand, at TR = 6.8ms, both fat and fibroglandular tissue reaches their maxima at the same time. Referring to Eq. [5.6], to satisfy the condition of both fat and water signal being acquired at their maximum signal intensities for correction fat-water separation, possible *TR*s are 2.3ms, 4.6ms, 6.8ms. Also taking into account the matrix size for the desired image resolution, and TE for the required Dixon in-phase and out-of-phase images, TR of 6.8ms is selected for this study.

The effect of FA on SSFP signal is demonstrated in Fig. 5.6, where the amplitudes of fat and fibroglandular tissue are plotted as a function of offset frequency. The maximum signals for fibroglandular tissue and fat are achieved at 30° and 70°, respectively. FA of 30° is used in the following experiments, since high water signal is desirable. In Fig. 5.7, the simulated phase signals at echo center as a function of offset frequency for both fat and fibroglandular tissue are presented at TE_1=2.3ms (Fig. 5.7 (a)) and TE_2 = 3.4ms (Fig. 5.7 (b)). The signals follow the expected in-phase and out-of-phase characteristics between fat and glandular tissue.

Phantom imaging

An example image of the water and oil phantom (Fig. 5.4), acquired using sequence 2, 3D SSFP sequence with dual-echo bipolar readout, is shown in Fig. 5.8. The magnitude and phase images of in-phase and out-of-phase signals are acquired at TE_1 = 2.3ms (Fig. 5.8 (a, b)) and TE_2 = 3.4ms (Fig. 5.8 (c, d)), respectively.

Fig. 5.9 demonstrates the calculated phase map, fat-only and water-only image, without phase unwrapping. It is noted that the fat and water signals are separated incorrectly due to the phase discrepancy appeared in the calculated phase map, see Fig.

5.9 (a). To better understand the source of the large phase difference seen in Fig. 5.9 (a), a line passing through the center of *k*-space from the two echoes is plotted in Fig. 5.10 (a). A three-pixel shift between the two echoes is clearly observed which is believed to be related to the delays in the acquisitions of the two echoes. Fig. 5.11 shows the results of fat-water separation after correcting the *k*-space misalignment (Fig. 5.10 (b)). From the fat-only images, as illustrated in Fig. 5.11 (b), the edges of the water bottle are clearly visible, especially along the readout direction (left to right), as indicated by the arrows. This can be explained by the misregistration from the bidirectional chemical shift due to the opposite polarity in the bipolar readout gradient. Since the imaging (receiver) frequency is centered on fat, no misregistration error is observed from the bottle filled with the oil. Similarly, the separated fat-only and water-only images using sequence 2 with imaging frequency centered on water is displayed in Fig. 5.12. The edge of the bottle filled with oil is visible in the water-only image (Fig. 5.12 (c)). Fat-water separation performance from sequence 3, 3D dual-echo SSFP sequence with alternating bipolar readout gradient polarity in adjacent TR, is illustrated in Fig. 5.13. In the fat-only (Fig. 5.13 (b)) and the water-only (Fig. 5.13 (c)) images, no visible error appears on the edges of the phantom. This is because the images acquired with the same polarity from adjacent TR are used for two-point Dixon reconstruction; therefore, there is no presence of the chemical shift induced misregistration errors.

The fat-water separation using the four sequence designs are further tested on vials filled with varying fat/water concentration (Fig. 5.4 (b)). An example image slice acquired using sequences 1–4 are displayed in Fig. 5.14 – Fig. 5.17, respectively. In each figure, magnitude and phase images acquired at TE_1 = 2.3ms (a, b) and TE_2 = 3.4ms (c,

d) for in-phase and out-of-phase images are displayed. Based on these source images, the resulting two-point Dixon fat-water separated images are shown in Fig. 5.18 (a–d), respectively.

Ex vivo imaging

An example image of a piece of pork acquired using sequence 1 is demonstrated in Fig. 5.19. The magnitude and phase images acquired at TE_1 = 2.3ms (Fig. 5.19 (a, b)) and TE_2 = 3.4ms (Fig. 5.19 (c, d)) are shown for the in-phase and out-of-phase cases, respectively. Fig. 5.20 illustrates the results of fat-water separation from sequences 1, 2 and 4. Excellent fat-only and water-only images are reconstructed from the three sequences.

The effect of FA is explored by implementing two-point Dixon fat-water separation at FA of 10°, 30°, 50°, and 70°. As shown in Fig. 5.21, FA 30º and 50º offer higher water signal compared with that from FA 10º and 70º. Because of the linear relationship between FA of the RF pulses and the energy deposited into the imaged object, FA 30 º is the best of the series of FA tested. This finding is consistent with the simulation study, as illustrated in Fig. 5.6.

The acceleration imaging ability of the 11-channel RF coil is accessed by imaging at various GRAPPA factors, ranging from one to four. The results of the separated fat-only and water-only images are shown in Fig. 5.22 (a–d) correspondingly. It appears that the performance of the fat-water separation is acceptable with a GRAPPA factor of two, or even three.

Comparisons of the fat-water separation using the GRE-based three-point Dixon and the SSFP-based two-point Dixon are demonstrated in Fig. 5.23 (a, b). Comparable fat-only and water-only images are obtained from the two techniques.

Fig. 5.24 illustrates SSFP image acquired with and without chemical selective fat saturation pulses. Compared with the water-only images obtained from Dixon methods, fat saturation pulses are less effective in fat suppression, as shown in Fig. 5.24 (b).

In vivo imaging

The four sequences were applied on a healthy volunteer, imaged in air using the Siemens 4-channel breast coil. Due to the restriction of the specific absorption rate (SAR), the highest image resolution for the four sequences was achieved with a FOV of 247 mm, 287 mm, 267 mm, and 274 mm, resulting in a pixel size of 1.3 mm, 1.5mm, 1.4mm, and 1.4mm, respectively. An example image from sequences 1–4 is demonstrated in Fig. 5.25–5.28. Banding artifacts are observed, especially around the regions that are close to the tissue/air interface. A large signal intensity variation across the object imaged is seen from images acquired using sequence 3 (Fig. 5.27). The banding artifacts appeared in Fig. 5.25–5.28 directly affect fat-water separation, as demonstrated in Fig. 5.29 (a–d). Moreover, Fig. 5.29 (c) indicates that incorrect fat-only and water-only images are obtained due to the severe image artifact in the source images acquired by sequence 3 (Fig. 5.27). The findings can be further confirmed by the thin-slab MIP of the water-only images, as shown in Fig. 5.30. Due to the erroneous fat-water separation (Fig. 5.29 (c)), little blood vessel information is available in Fig. 5.30 (c). On the other hand, images acquired using sequences 1, 2 and 4 present comparable amount the details for the blood vessels, as shown in Fig. 5.30 (a, b, d).

Because the total image acquisition time for sequence 2 is half of that from sequences 1 and 4, the motion occurs during the image acquisition can thus be minimized by using sequence 2. Also due to the imperceptible error of chemical shift induced misregistration, sequence 2 becomes the optimal sequence for *in vivo* imaging application. Sequence 2 is validated on three more subjects, each with different experimental setup. Fig. 5.31–5.32 show results from a healthy subject, imaged in a water bath using the MRgHIFU system without heating. An example sagittal slice of the magnitude and phase for the in-phase and out-of-phase signal is demonstrated in Fig. 5.31. Fig. 5.32 (a–c) represents the sagittal slice of the water-only image, fat-only image, and thin-slab MIP, respectively. Despite the banding and motion-induced artifact at the water/air interface, fibroglandular tissues and blood vessels (arrow) are clearly visualized in the thin-slab MIP image, as shown in Fig. 5.32 (c). Fig. 5.33 and Fig. 5.34 show results from another healthy subject, imaged in air using the Siemens 4-channel coil. An example sagittal slice of the magnitude and phase image for the in-phase and out-of-phase signal is demonstrated in Fig. 5.33. The reconstructed sagittal slice of the water-only image, fat-only image, and thin-slab MIP is given in Fig. 5.34 (a–c), respectively. Blood vessels (arrow) are clearly visible in the thin-slab MIP image (Fig. 5.34 (c)). The fourth subject with fibroadenoma was imaged in the air using the 11-channel coil. Fig. 5.35 shows an example sagittal slice of the magnitude and phase images for the in-phase and out-of-phase signal. The reconstructed sagittal slice of the water-only image, fat-only image, and thin-slab MIP is shown in Fig. 5.36 (a–c), respectively. Details of the blood vessels are seen in the thin-slab MIP image (Fig. 5.36 (c)). It is noticeable that, in Fig. 5.36, signal from fat (arrow) shows up in the water-only image. This is because the phase unwrapping fails at the dark banding artifact, referring to the sources images shown in Fig. 5.35.

Discussion

In this chapter, a comprehensive examination of the two-point Dixon fat-water separation technique using 3D SSFP sequence is presented. The advantages and disadvantages of various sequence designs with variations in the readout gradients are investigated through a series of phantom, *ex vivo* and *in vivo* experiments. The MIP of the reconstructed water-only breast images shows details of the blood vessels that would otherwise be obscured by fat. Overall, the potential of two-point Dixon fat-water separation based on 3D dual-echo SSFP sequence for breast MRA imaging is demonstrated.

Signal characteristics of the four pulse sequence designs have been studied in this work. Particularly, results from both phantoms (Fig. 5.16) and subjects (Fig. 5.27) suggest that the images acquired using sequence 3 — dual-echo readout with alternating bipolar gradient polarity in adjacent TR — suffer from severe artifacts, possibly due to the motion caused by the interleaved alternating polarity in the readout gradient design. Sequence 2 — dual-echo readout with a bipolar gradient polarity — is associated with intrinsic chemical-shift-induced misregistration error between the in-phase and out-of-phase images, as explained in Fig. 5.1. This error can be resolved by the design in sequence 4 — complete dual-echo readout with a bipolar gradient polarity, followed by the dual-echo readout with an opposite bipolar gradient polarity. However, the doubled image acquisition time in the sequences 1 and 4 make them prone to motion artifacts due to breathing motion from the subjects, and the water movement in the MRgHIFU system. Further, because of the high readout BW used in our experiments, the bidirectional chemical shift from the bipolar readout gradient is generally less than the size of a pixel. In the results presented in Section 5.4, the chemical shift induced misregistration is only identified from the phantom composed of the water and the vegetable oil (Fig. 5.4 (a)). *In vivo* results show that dual-echo SSFP with a bipolar readout is the most consistent imaging sequence of the four sequences tested for the breast MRA application.

It is noticeable that the *in vivo* water-only images given in Section 5.4.4 show residual fat signal, as only two chemical species with unique Larmor frequencies can be separated using the two-point Dixon. In reality, fatty tissue may appear in multiple peaks in an NMR spectrum. In this case, extra images acquired at additional TE (110) are needed for the separation among fat with different frequencies. For breast MRA application, the residual fat signal in the water-only images is not very problematic, as long as there is good contrast between blood and the background tissue.

Compared to the phantom and *ex vivo* experiments, image quality from the *in vivo* studies suffers more from the banding artifacts, resulting in intensity variations in the fat-only and water-only images. In the presence of these artifacts, the visibility of the vasculature can be degraded. For example, in Fig. 5.25–5.30, the banding artifacts are clearly seen. This can be explained by the improper shimming during the image acquisition. Moreover, the stability of the phase unwrapping can also be affected by the dark band, as shown in Fig. 5.36 (b, c).

In the future, approaches can be undertaken to reduce or alleviate the banding artifacts. One effective strategy is to reduce the field inhomogeneity across the region of imaged object, by applying local shimming and second order shimming. Another way is to introduce extra scans with different phase cycling strategy to spatially move the bands around (111). The images are further combined to reduce the signal inhomogeneity induced by the banding artifact. In addition, the performance of the flow-independent MRA technique can be compared to the contrast-enhanced studies to further validate the presented technique.

Summary

In this chapter, we demonstrate the feasibility of using dual-echo SSFP based sequence for breast MRA imaging. The characteristics of various sequence designs in the readout gradient are discussed. Results show that breast vasculature can be visualized from the thin-slab MIP images using the SSFP sequence combined with the two-point Dixon.

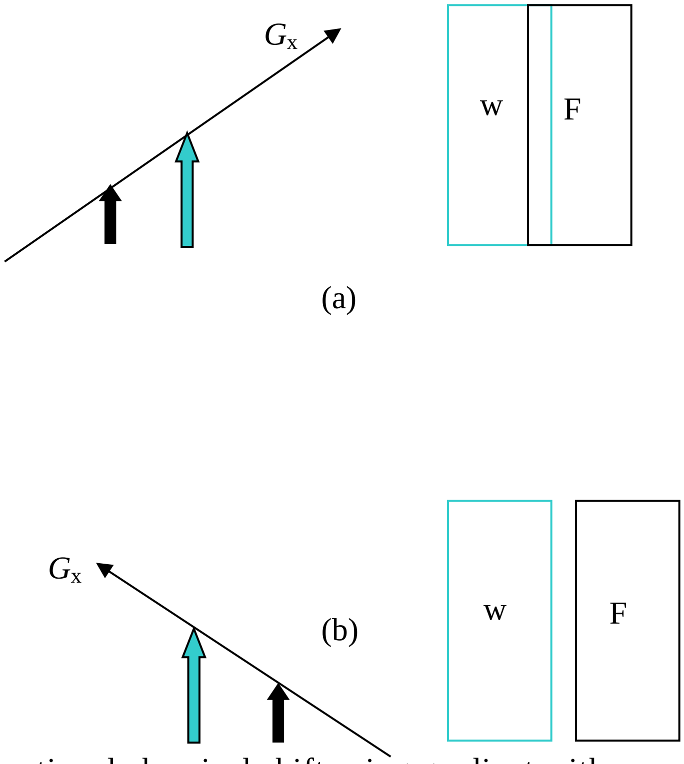

Figure 5.1. Bidirectional chemical shift using gradient with opposite polarities. (a) Relative chemical shift using readout gradient with one polarity; (b) relative chemical shift using readout gradient with the opposite polarity. In this demonstration, the imaging frequency is assumed to be centered on water, therefore the position of water component (blue) is fixed in (a) and (b). However, the shift of fat component (black) appears on opposite side relative to water.

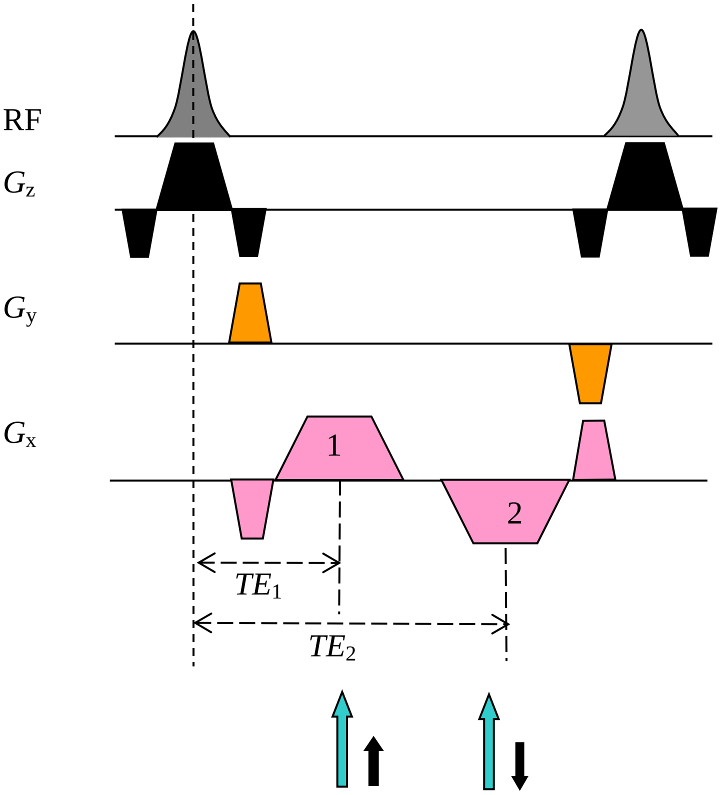

Figure 5.2. Schematic diagram of the dual-echo SSFP sequence with a bipolar gradient polarity. In-phase and out-of-phase images are acquired by choosing appropriate TEs, as explained in Eq. [5.8]. Blue and black arrows represent water and fat, respectively.

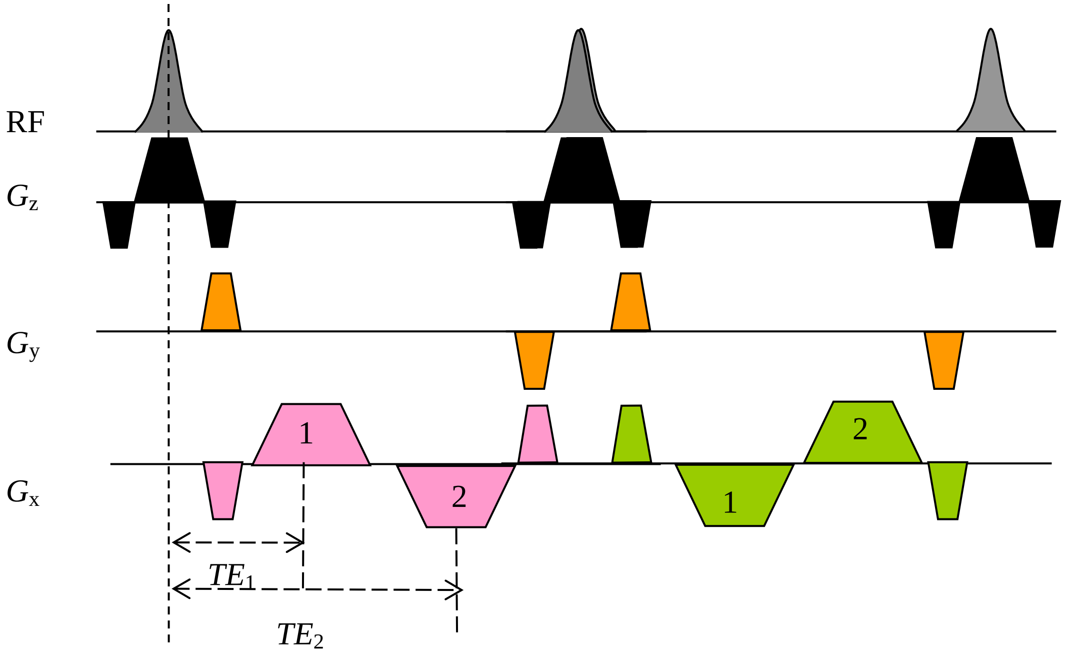

Figure 5.3. Schematic diagram of the dual-echo SSFP sequence with alternating bipolar readout gradients in an interleaved fashion.

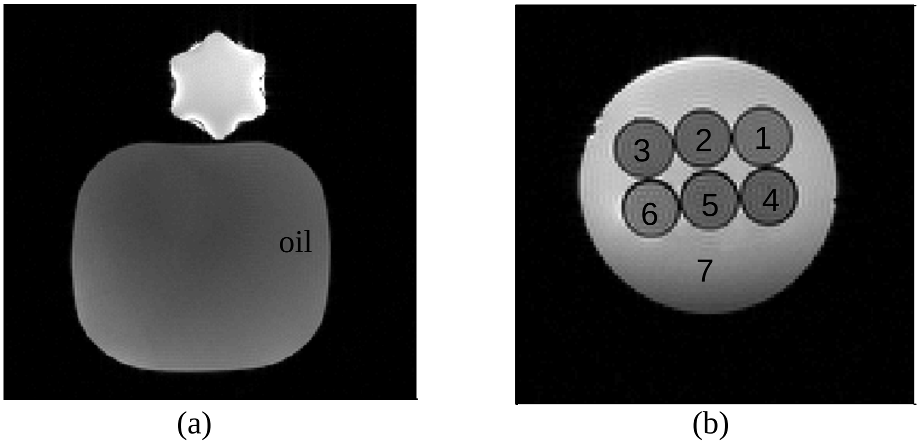

(a) (b)

Figure 5.4. Axial image of phantoms: (a) two bottles each filled with pure water and pure vegetable oil; (b) six vials with varying water/fat concentration in a water bath (#7). Vial #1–#5 contain 20%, 40%, 60%, 80% and 100% of mayonnaise, and vial #6 is filled with pure vegetable oil.

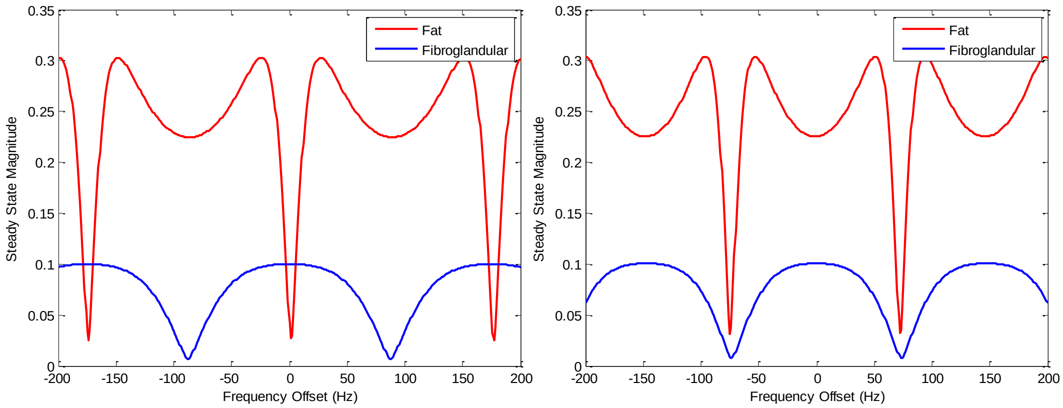

Figure 5.5. Simulated SSFP signal of fat and fibroglandular tissue as a function of frequency offset at (a) TR=5.7 and (b) TR=6.8ms. Signal of fat and fibroglandular tissue reach maximum value at the same time at TR=6.8ms, but not at TR=5.7ms.

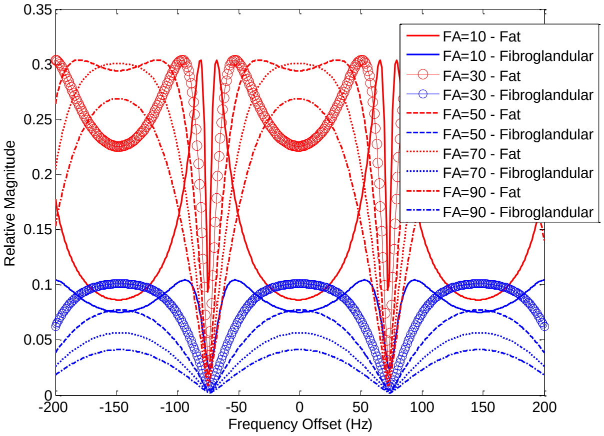

Figure 5.6. Simulated SSFP magnitude signal as a function of frequency offset for fat (red) and fibroglandular tissue (blue) at FA of 10°, 30°, 50°, 70°, 90°. *TR*= 6.8ms. Maximum fibroglandular signal is achieved at FA of 30°.

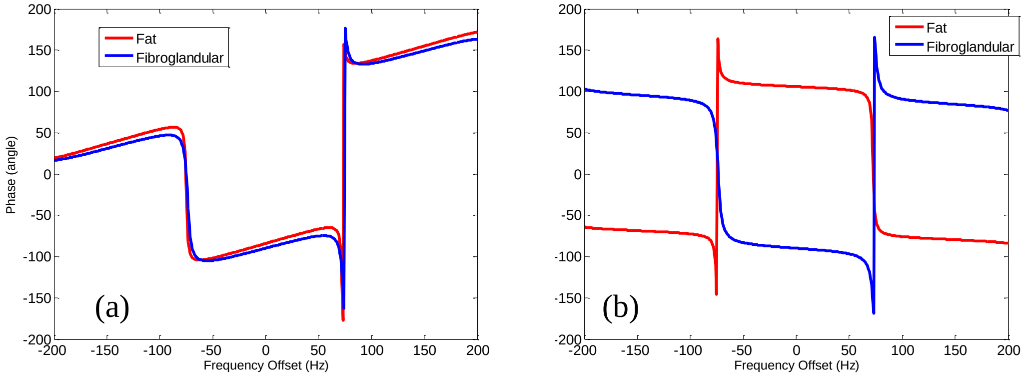

Figure 5.7. Simulated dual-echo SSFP (a) in-phase (TE_1 = 2.3ms) and (b) out-of-phase (TE_2 = 3.4ms) signal as a function of frequency offset.

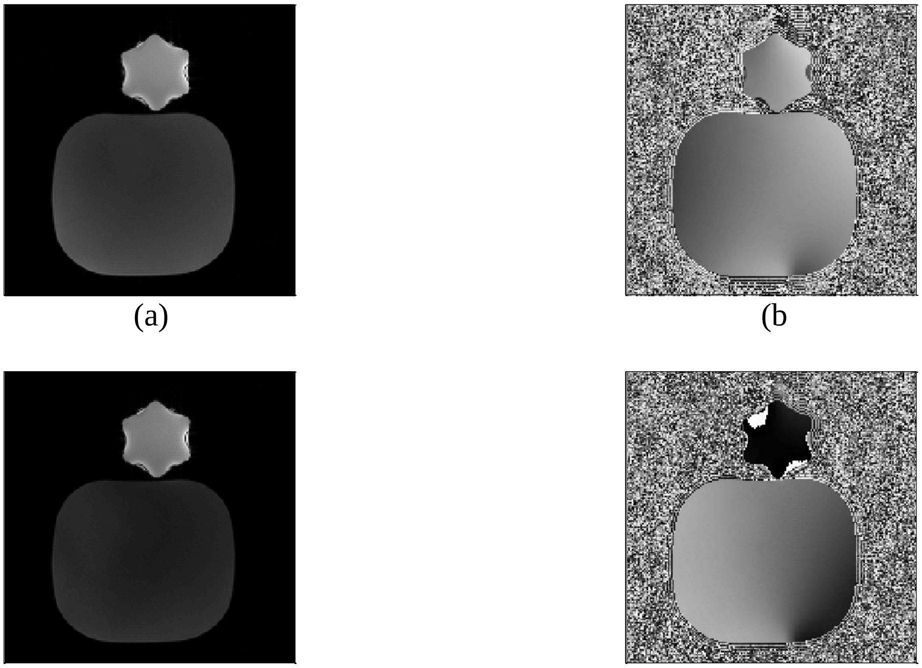
(a)

(b

Figure 5.8. An example image acquired using sequence 2—3D SSFP sequence with dual-echo bipolar readout. The magnitude and phase images for in-phase and out-of-phase are acquired at (a, b) TE_1 = 2.3ms and (c, d) TE_2 = 3.4ms, respectively.

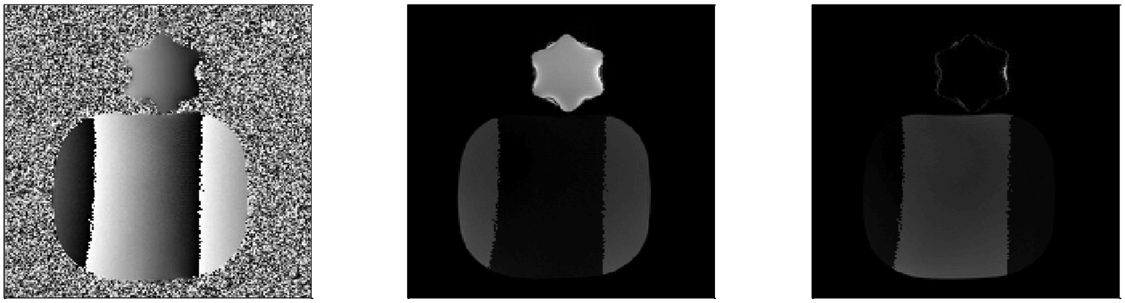
(a) (b) (c)

Figure 5.9. Two-point Dixon reconstruction without phase unwrapping processing, based on the source images given in Fig. 5.8. (a) Phase map, (b) fat-only and (c) water-only images. The phase map was calculated using Eq. [5.4].

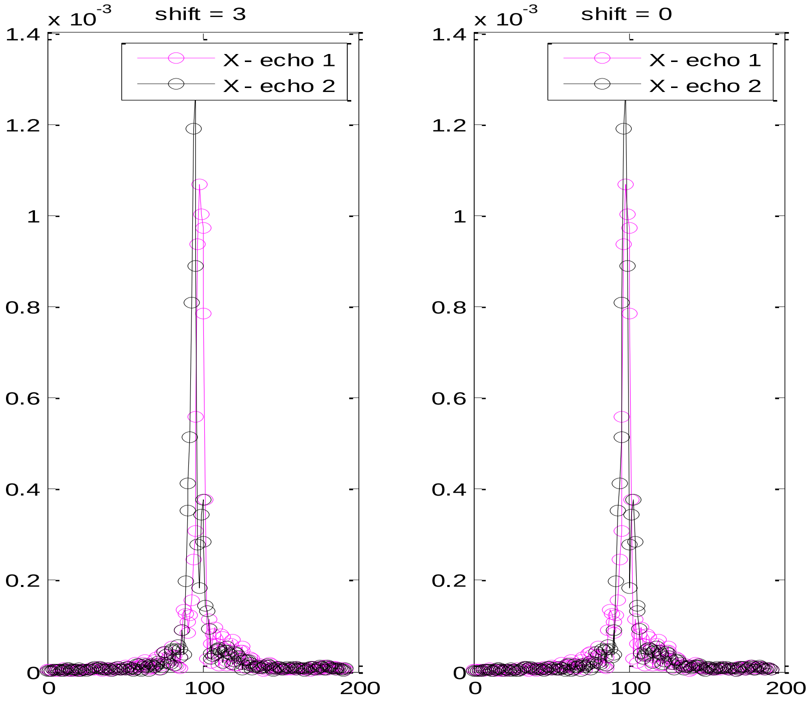

(a) (b)

Figure 5.10. A line profile of the center of the *k*-space from the two echoes acquired using 3D SSFP sequence with dual-echo bipolar readout. (a) Before *k*-space adjustment, there is a three-pixel shift between the *k*-space peaks; (b) after correcting the *k*-space misalignment, the *k*-space peak from the two echoes overlap.

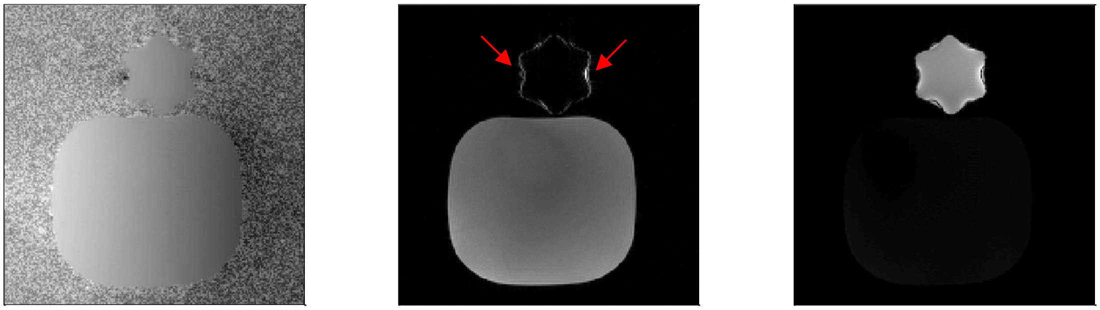

(a) (b) (c)

Figure 5.11. Two-point Dixon reconstruction based on the source images shown in Fig. 5.8, with *k*-space misalignment correction. (a) Phase difference, (b) fat-only and (c) water-only images. The imaging frequency is centered on fat. As pointed by the arrows, the edges of the water bottle were incorrectly separated as fat-only signal. The intrinsic error caused by the bidirectional chemical shift between fat and water using the bipolar readout gradient polarity.

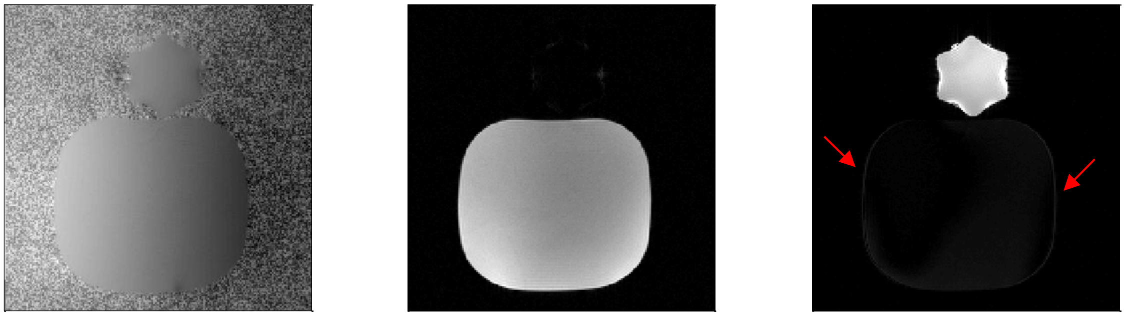

(a) (b) (c)

Figure 5.12. Two-point Dixon reconstruction using sequence 2, the 3D SSFP sequence with dual-echo bipolar readout. The imaging frequency is centered on water. (a) Phase difference, (b) fat-only and (c) water-only images. As pointed by the arrows, the edges of the fat bottle are incorrectly separated as water-only signal. The intrinsic error caused by the bidirectional chemical shift between fat and water using the bipolar readout gradient polarity.

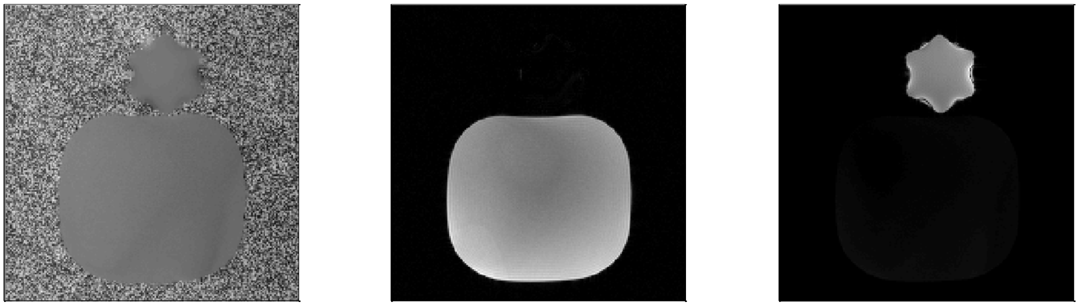

(a) (b) (c)

Figure 5.13. Two-point Dixon reconstruction using sequence 3, 3D SSFP sequence with alternating dual-echo bipolar readout polarity in adjacent TR. (a) Phase difference, (b) fat-only and (c) water-only images. The error caused by the bidirectional chemical shift as shown in Fig. 5.12 and Fig. 5.13 disappears.

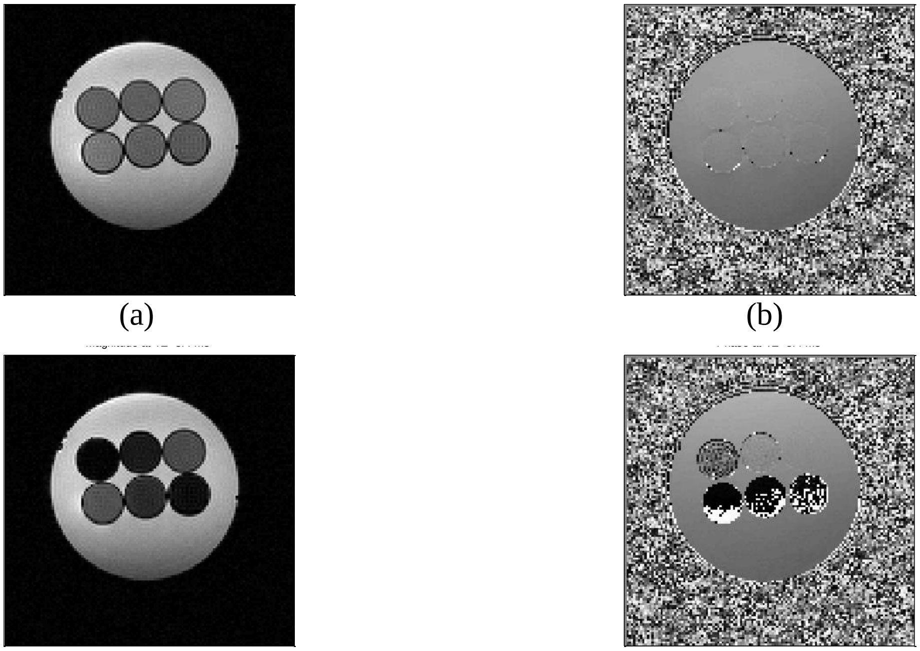

(a) (b)

(c) (d)

Figure 5.14. An example image acquired using sequence 1, 3D SSFP sequence with separate single-echo readout. The magnitude and phase images at (a, b) $TE_1 = 2.3ms$ and (c, d) $TE_2 = 3.4ms$ for in-phase and out-of-phase, respectively.

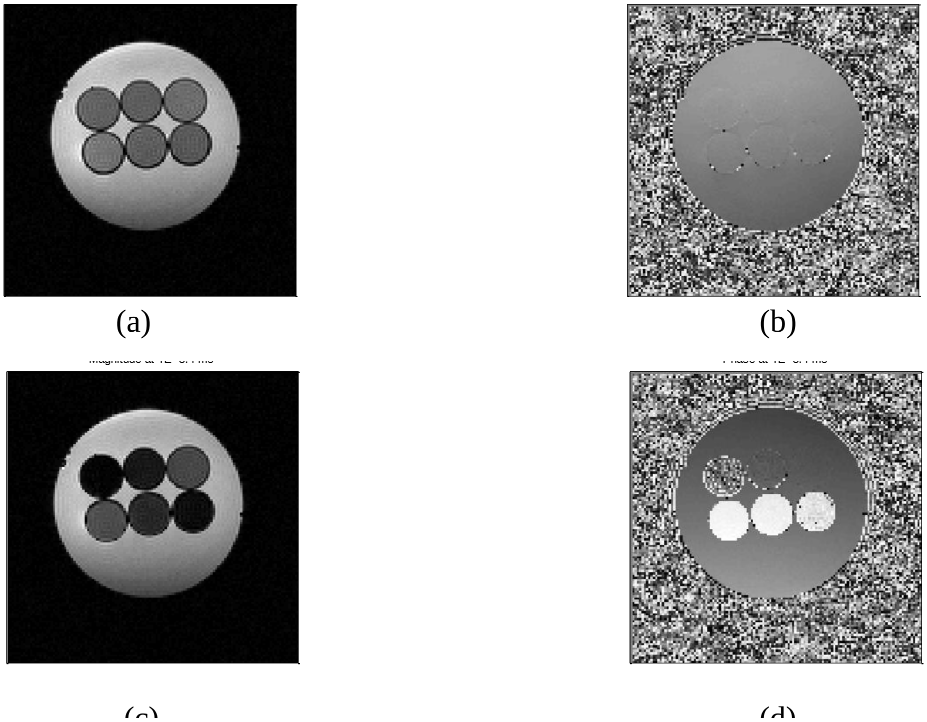
(a) (b)

(c) (d)

Figure 5.15. An example image acquired using sequence 2, 3D SSFP sequence with bipolar dual-echo readout. The magnitude and phase images acquired at (a, b) TE_1 = 2.3ms and (c, d) TE_2 = 3.4ms for in-phase and out-of-phase, respectively.

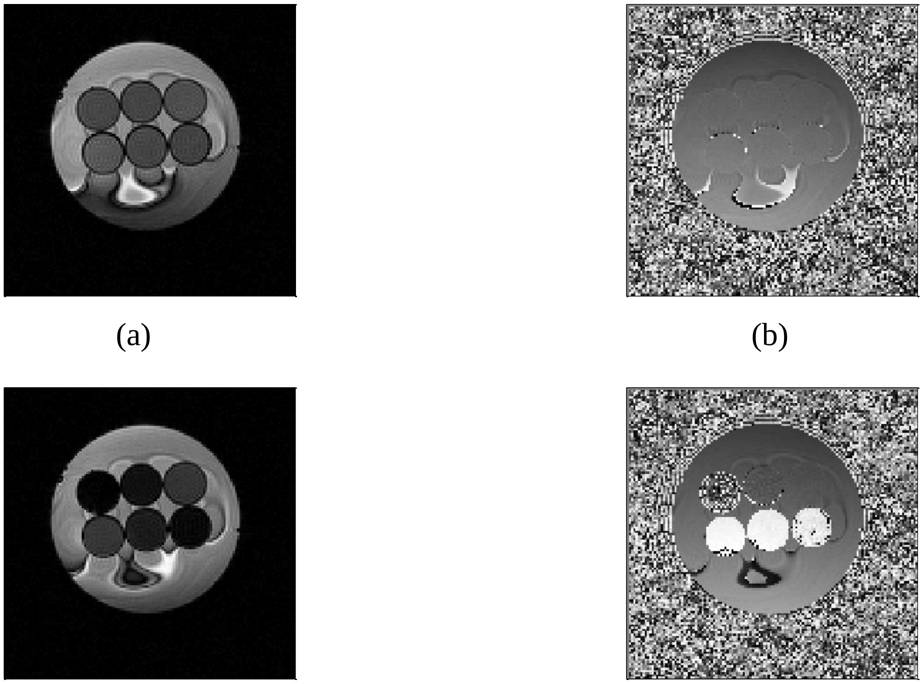

(a) (b)

(c) (d)

Figure 5.16. An example image acquired using sequence 3, 3D SSFP sequence with alternating dual-echo bipolar readout polarity in adjacent TR. The magnitude and phase images at (a, b) TE_1 = 2.3ms and (c, d) TE_2 = 3.4ms for in-phase and out-of-phase, respectively.

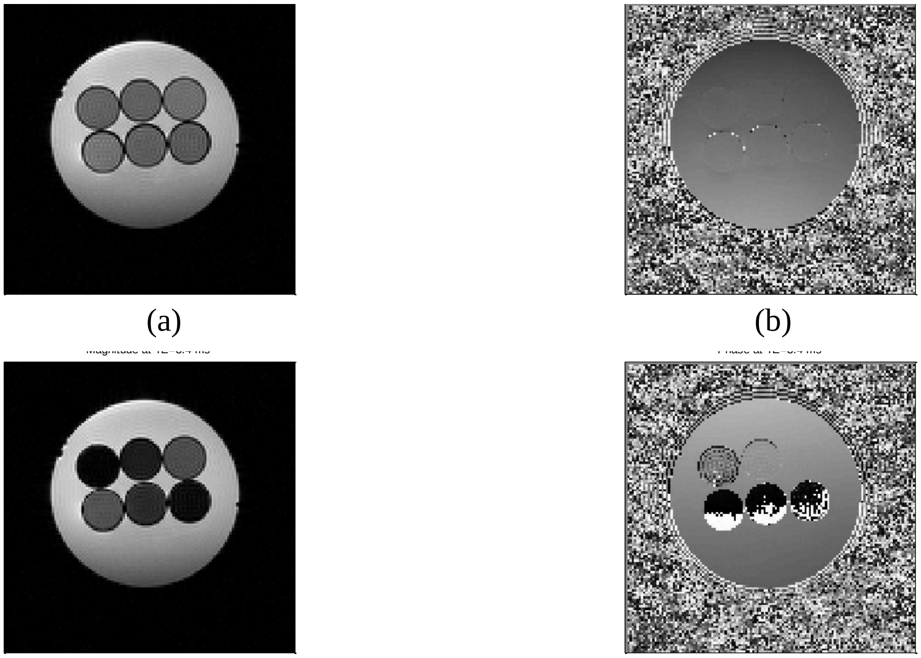

(a) (b)

(c) (d)

Figure 5.17. An example image acquired using sequence 4, 3D SSFP sequence with consecutive readout at one dual-echo bipolar polarity followed an opposite dual-echo bipolar polarity. The magnitude and phase images at (a, b) TE_1 = 2.3ms and (c, d) TE_2 = 3.4ms for in-phase and out-of-phase, respectively.

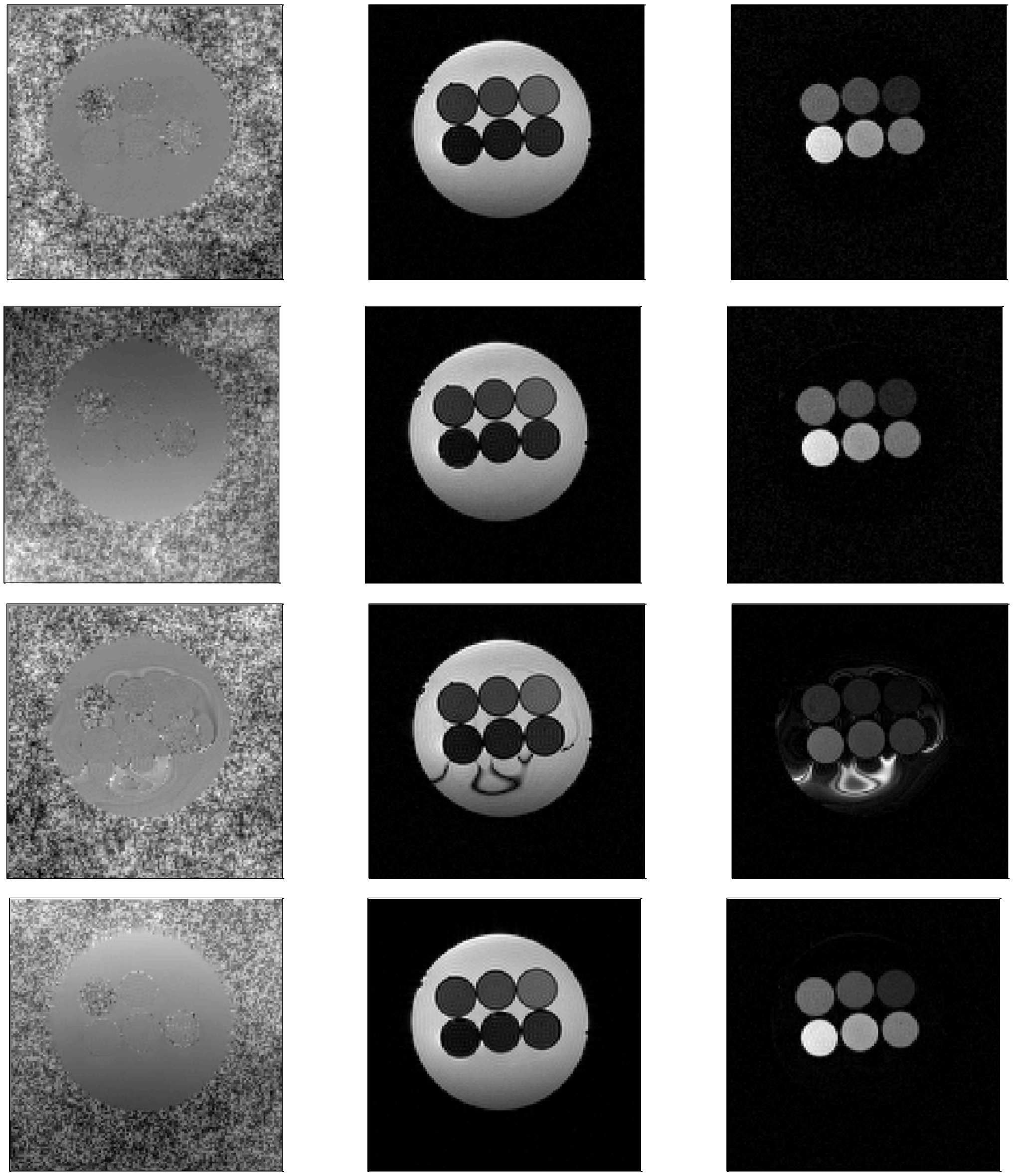

Figure 5.18. Two-point Dixon reconstruction based on the sources images given in (a) Fig. 5.14, (b) Fig. 5.15, (c) Fig. 5.16, and (d) Fig. 5.17, respectively. Phase maps, water-only images, and fat-only images are shown in the first, second and third column, respectively.

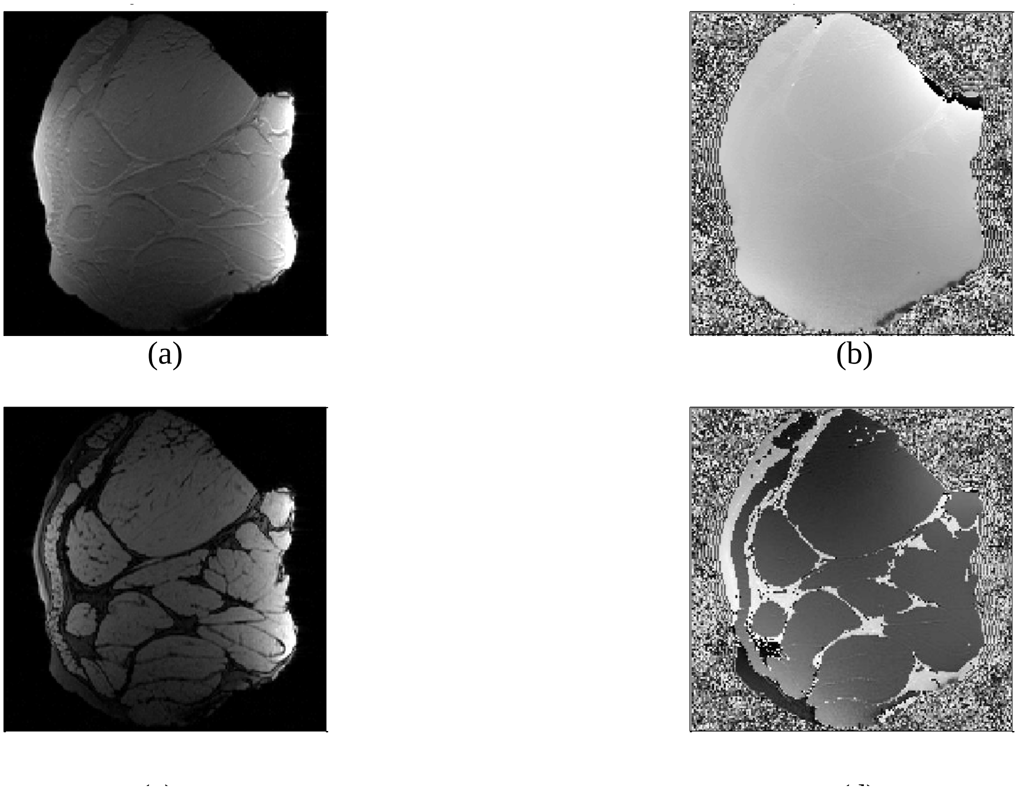

(a) (b)

Figure 5.19. Example magnitude and phase images of pork acquired at (a, b) TE_1 = 2.3ms and (c, d) TE_2 = 3.4ms for in-phase and out-of-phase, respectively.

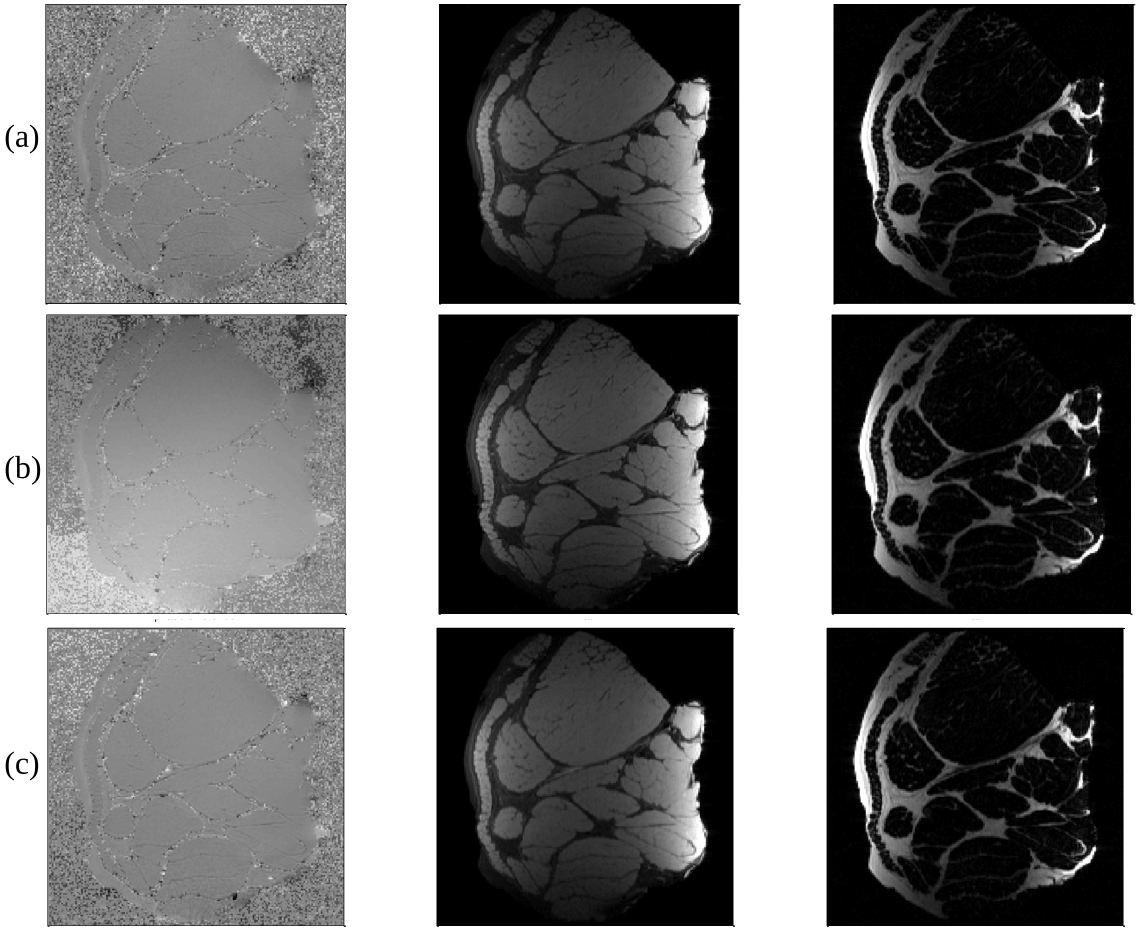

Figure 5.20. Two-point Dixon reconstruction based on the images acquired using (a) sequence 1, (b) sequence 2, and (c) sequence 4. The phase map, water-only and fat-only images are displayed in the first, second and third column, respectively.

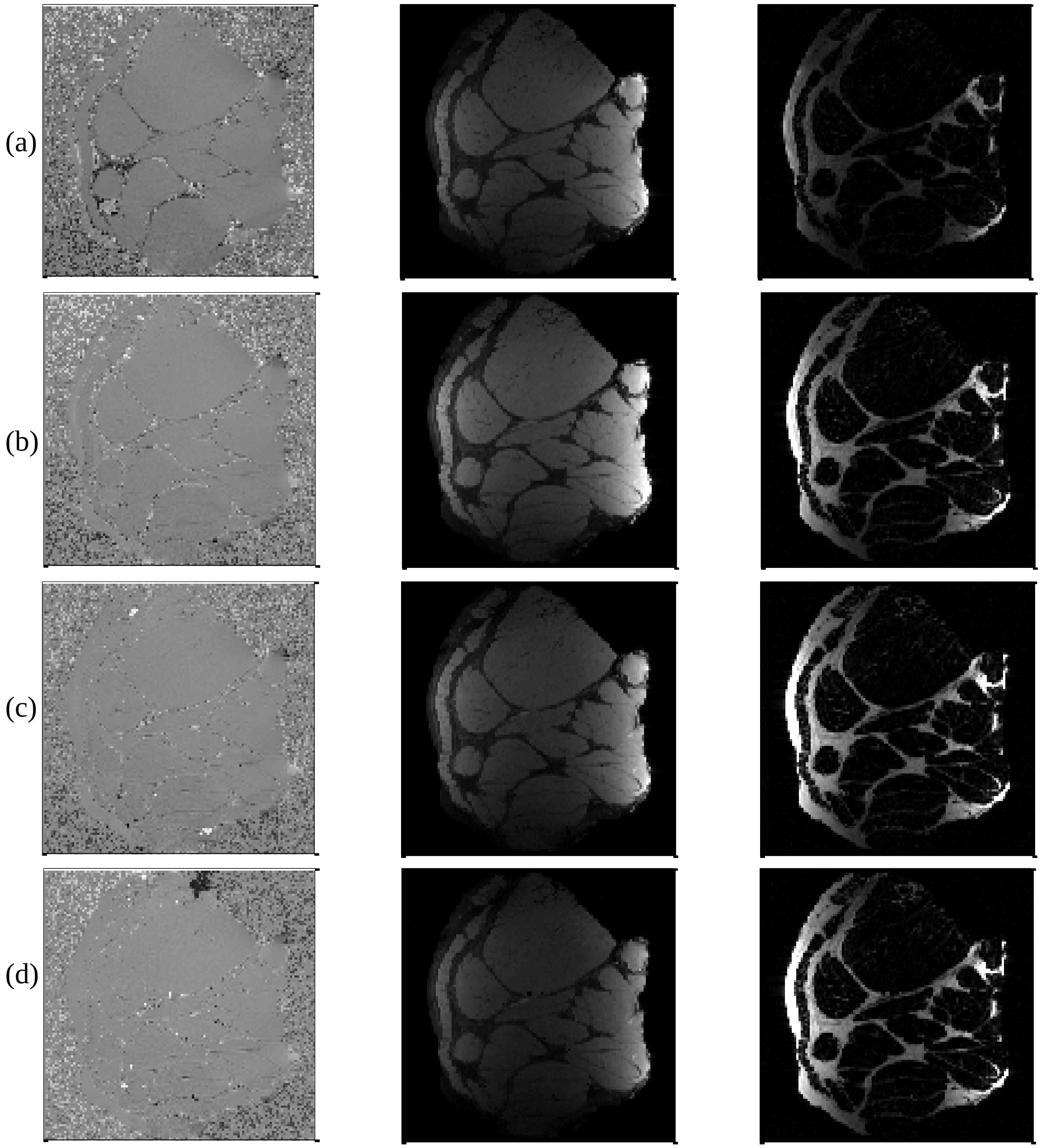

Figure 5.21. Two-point Dixon reconstruction based on the images acquired at FA of (a) 10º, (b) 30º, (c) 50º and (d) 70º. The phase map, water-only and fat-only images are displayed in the first, second and third column, respectively.

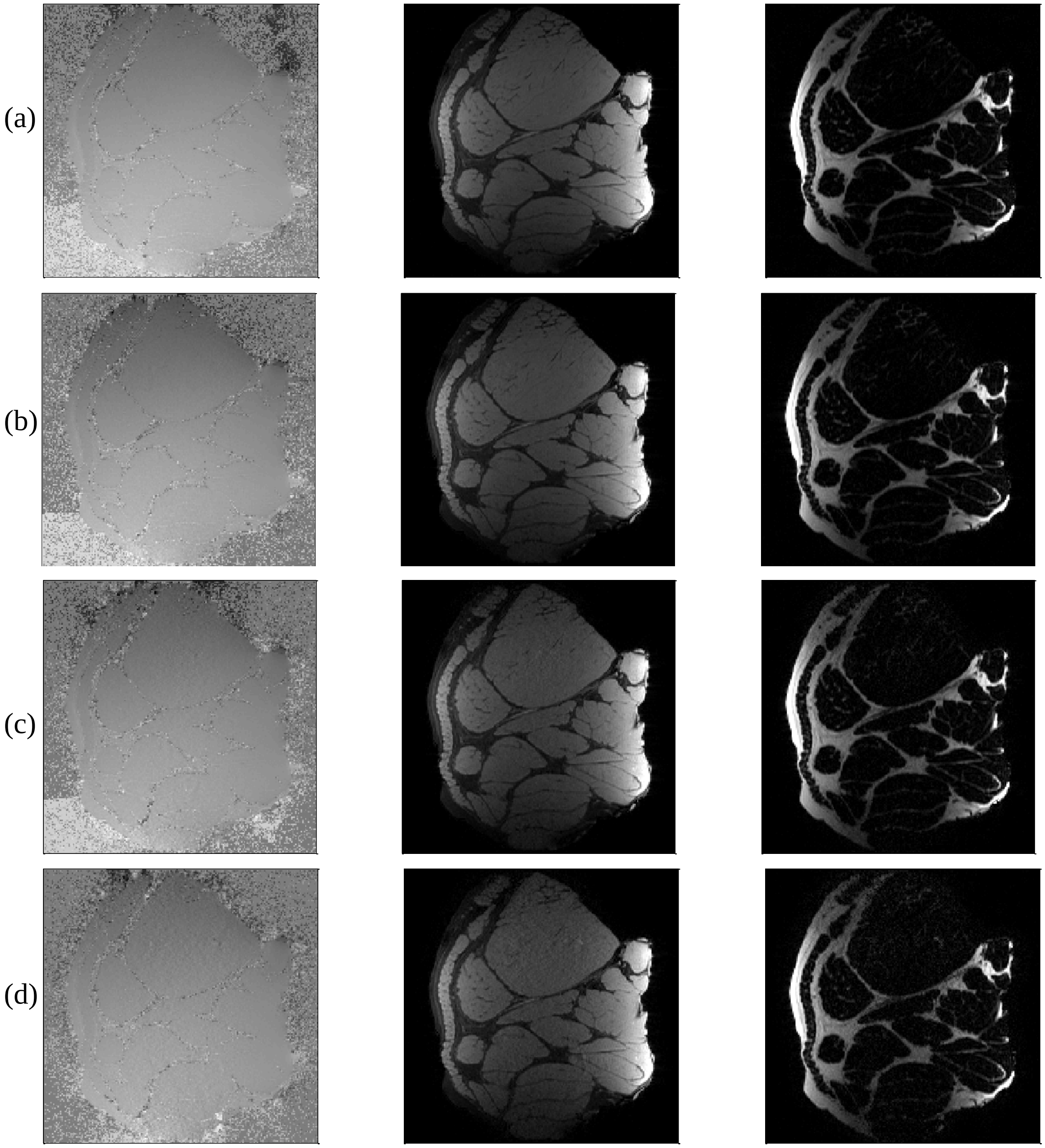

Figure 5.22. Two-point Dixon reconstruction based on the images acquired with a generalized autocalibrating partially parallel acquisition (GRAPPA) factor of (a) one, (b) two, (c) three and (d) four. The phase maps, water-only and fat-only images are displayed in the first, second and third column, respectively.

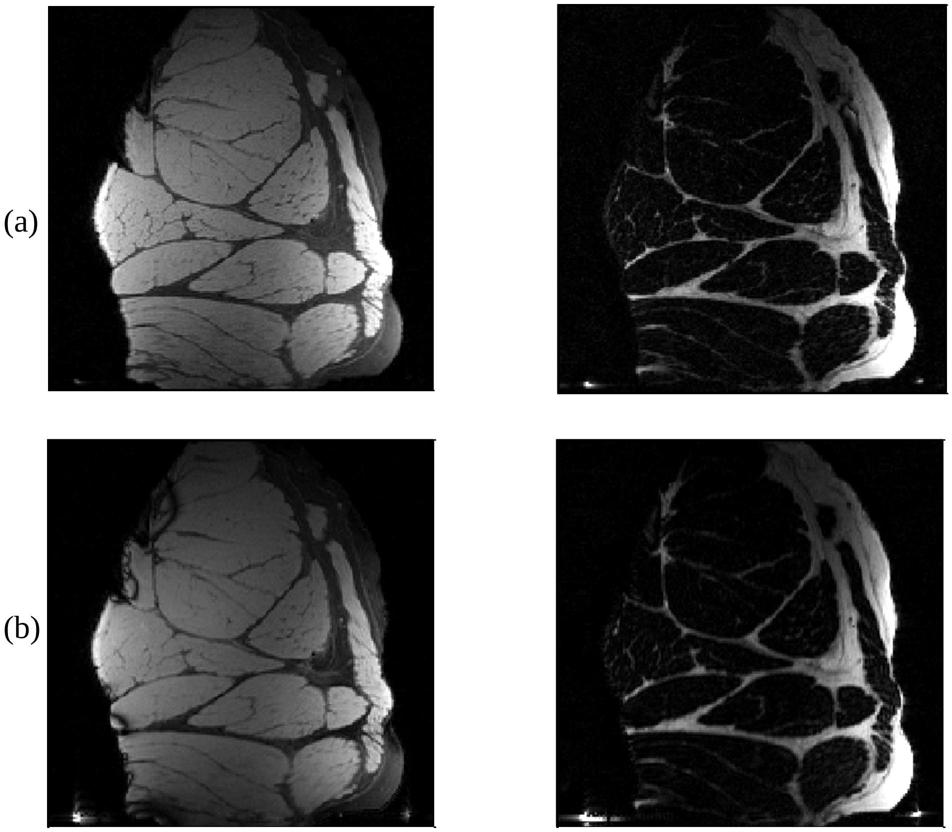

Figure 5.23. Comparison of fat-water separation from (a) GRE-based three-point Dixon and (b) SSFP-based two-point Dixon reconstruction. The water-only and fat-only images are displayed in the first and second column, respectively.

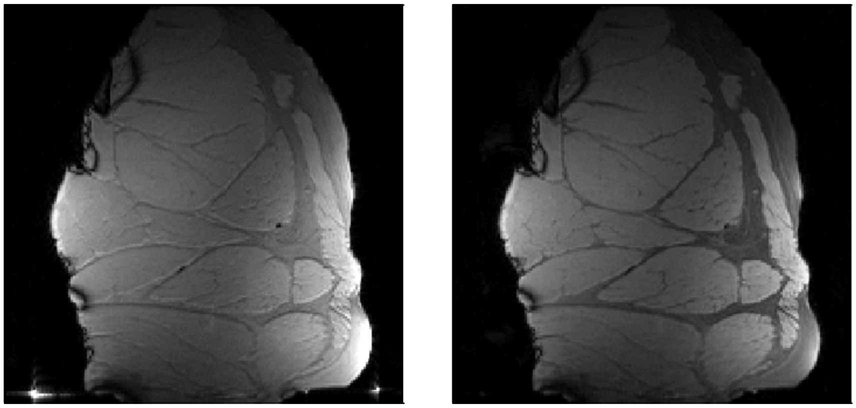

(a) (b)

Figure 5.24. An example SSFP image (a) without and (b) with the chemical selective fat saturation pulses.

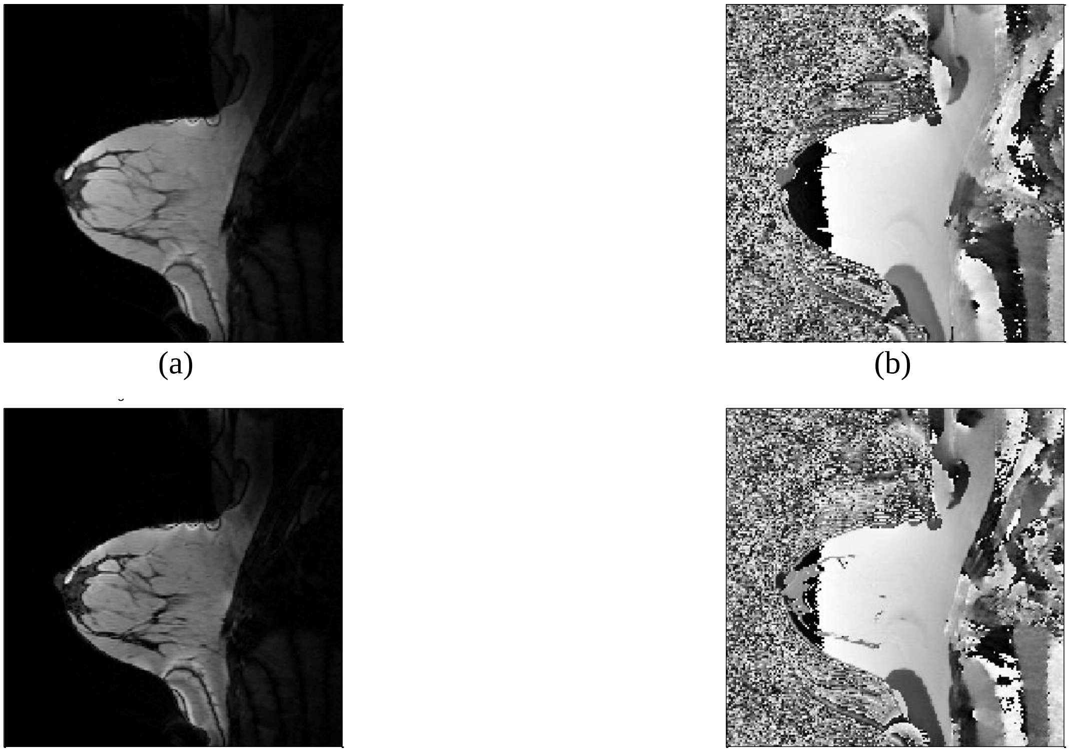
(a) (b)

(c) (d)

Figure 5.25. An example image acquired using sequence 1. The magnitude and phase images acquired at (a, b) TE_1 = 2.3ms and (c, d) TE_2 = 3.4ms for in-phase and out-of-phase, respectively.

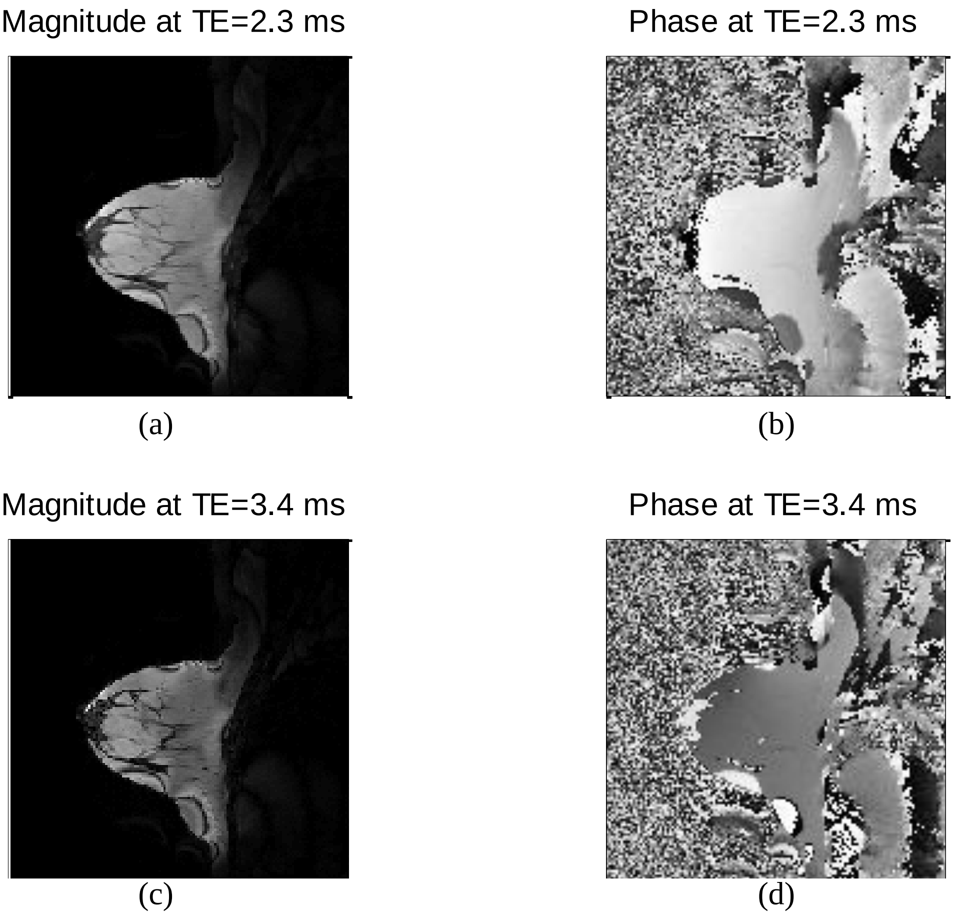

Magnitude at TE=2.3 ms

Phase at TE=2.3 ms

(a)

(b)

Magnitude at TE=3.4 ms

Phase at TE=3.4 ms

(c)

(d)

Figure 5.26. An example image acquired using sequence 2. The magnitude and phase images acquired at (a, b) TE_1 = 2.3ms and (c, d) TE_2 = 3.4ms for in-phase and out-of-phase, respectively.

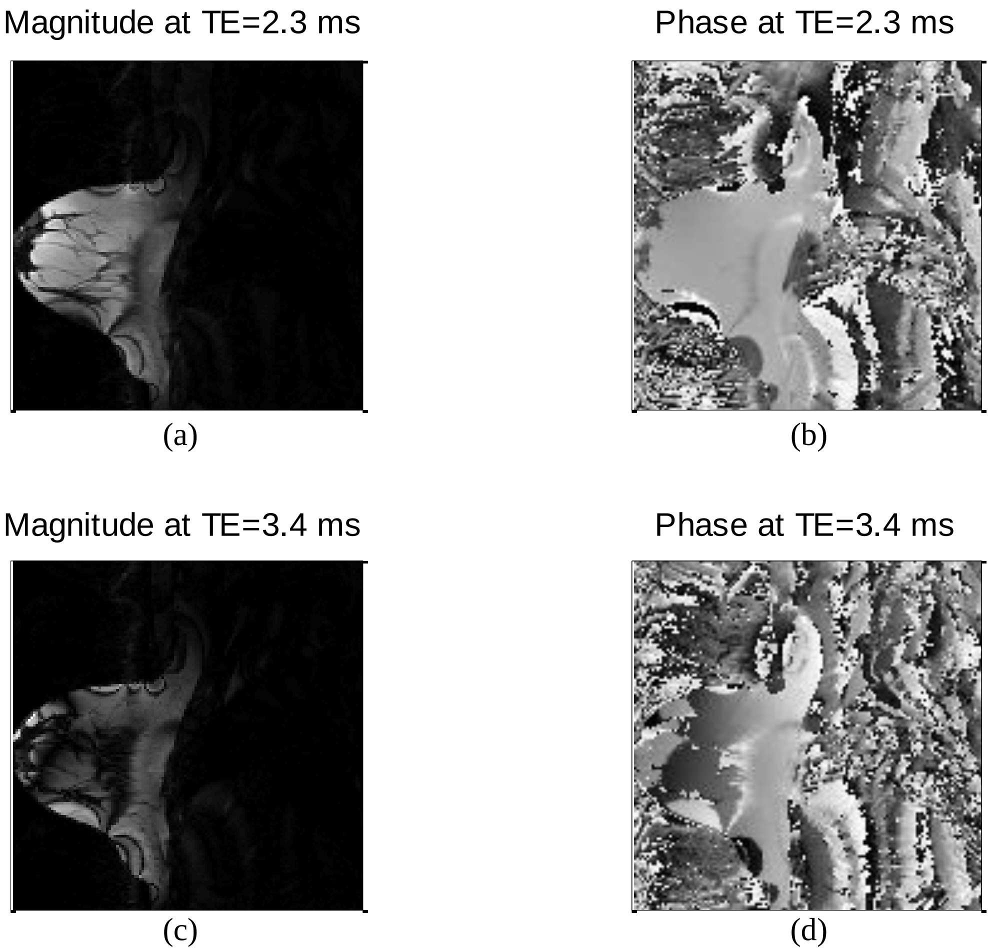

Figure 5.27. An example image acquired using sequence 3. The magnitude and phase images acquired at (a, b) TE_1 = 2.3ms and (c, d) TE_2 = 3.4ms for in-phase and out-of-phase, respectively.

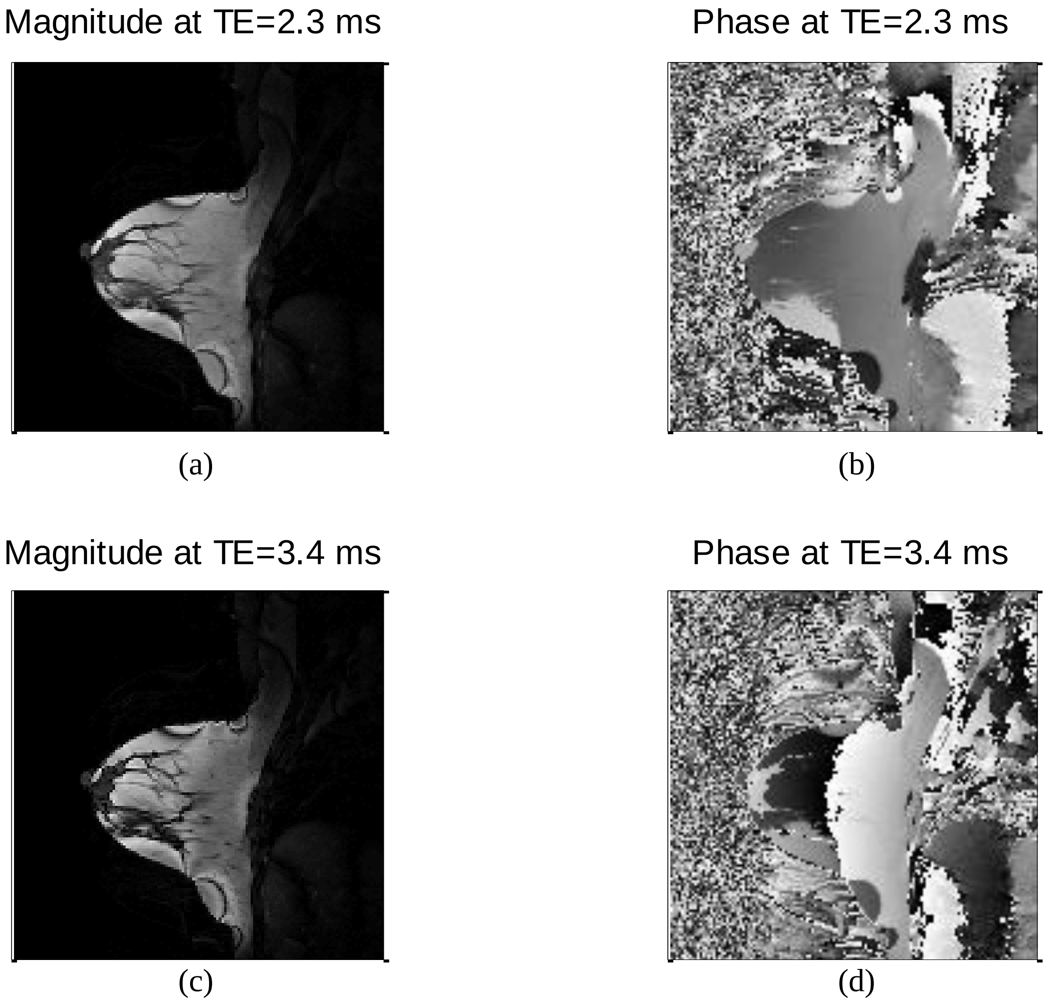

Magnitude at TE=2.3 ms

Phase at TE=2.3 ms

(a)

(b)

Magnitude at TE=3.4 ms

Phase at TE=3.4 ms

(c)

(d)

Figure 5.28. An example image acquired using sequence 4. The magnitude and phase images at (a, b) TE_1 = 2.3 ms and (c, d) TE_2 = 3.4 ms, corresponding to in-phase and out-of-phase, respectively.

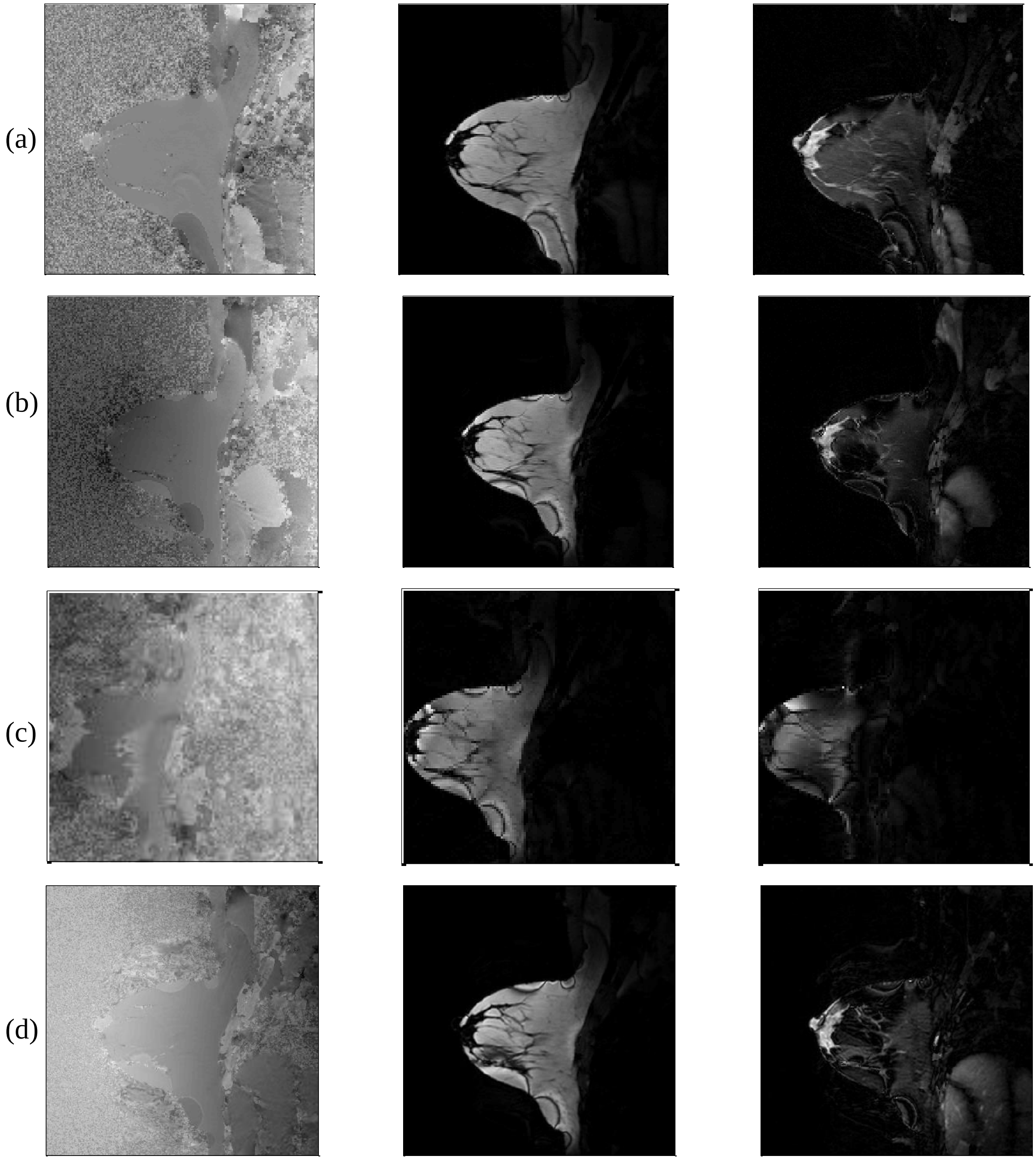

Figure 5.29. Two-point Dixon fat-water separation based on the sources images given in (a) Fig. 5.25, (b) Fig. 5.26, (c) Fig. 5.27 and (d) Fig. 5.28. The phase maps, fat-only and water-only images are shown in the first, second and third column, respectively.

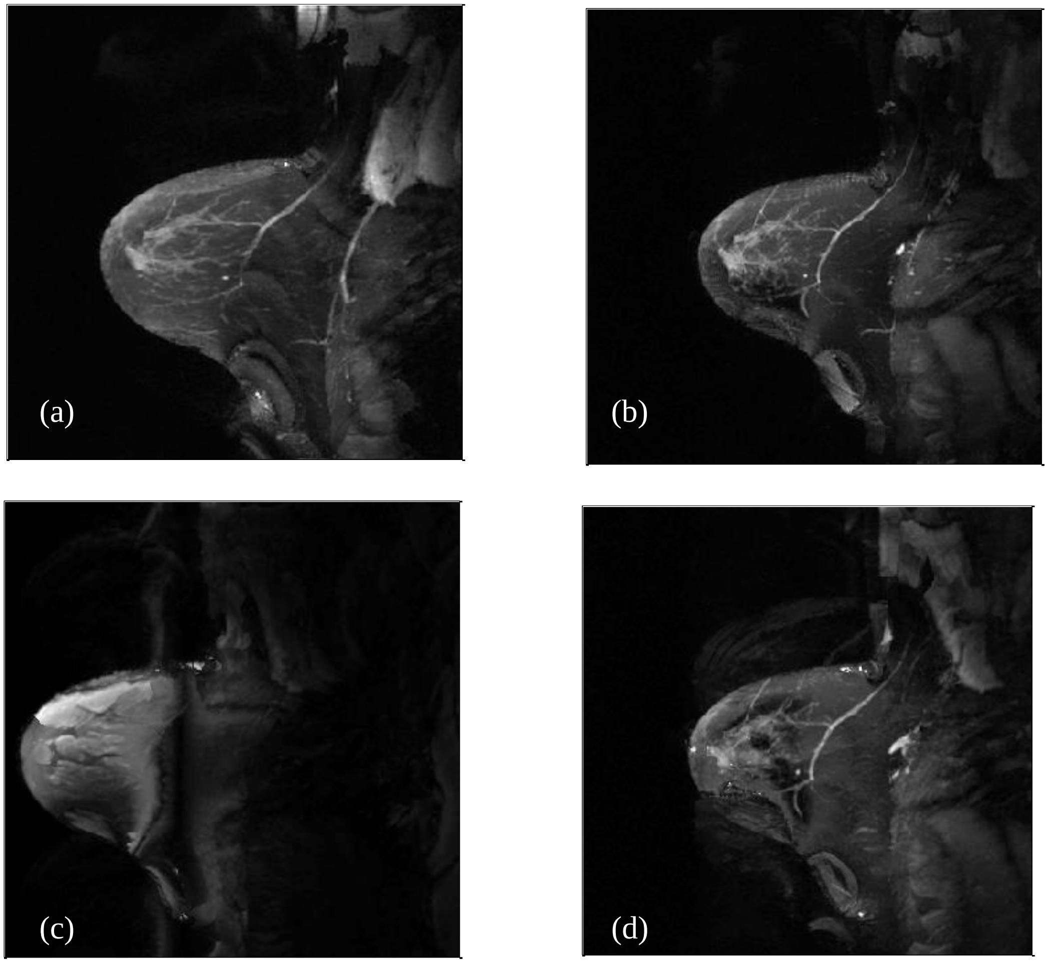

Figure 5.30. Thin-slab MIP of the water-only images acquired using (a) sequence 1, (b) sequence 2, (c) sequence 3 and (d) sequence 4. Slices with the same anatomical coverage were chosen for the MIP display.

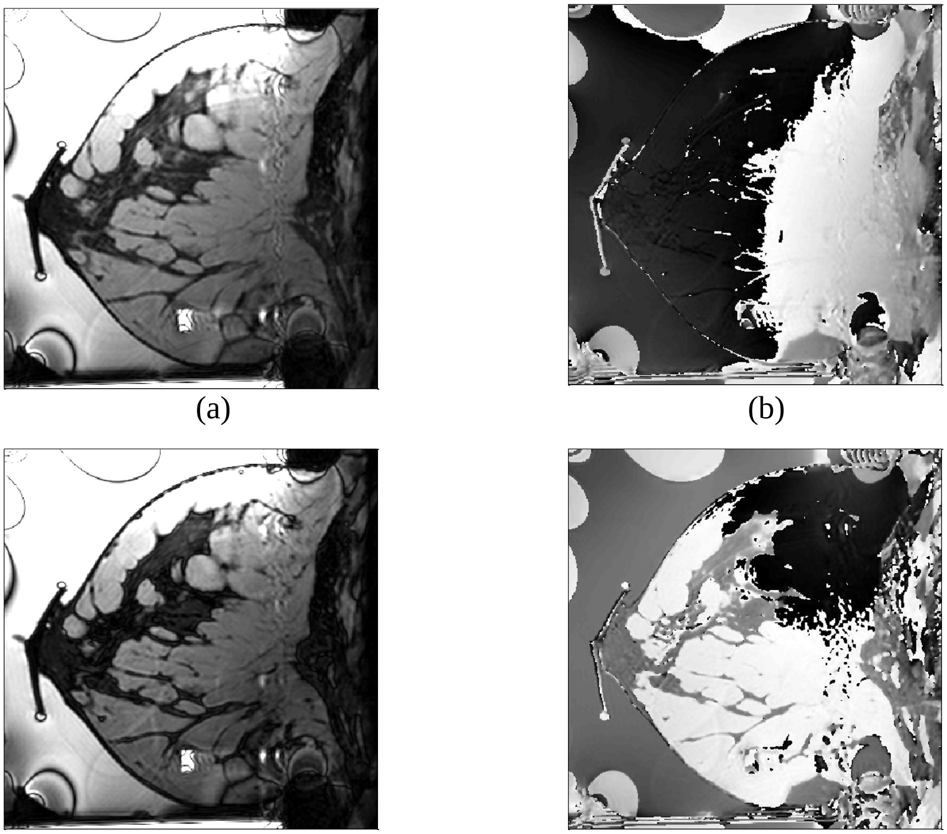

(a) (b)

(c) (d)

Figure 5.31. An example image acquired using sequence 2—3D SSFP sequence with bipolar dual-echo readout. The magnitude and phase images acquired at (a, b) TE_1 = 2.3ms and (c, d) TE_2 = 3.4ms for in-phase and out-of-phase, respectively.

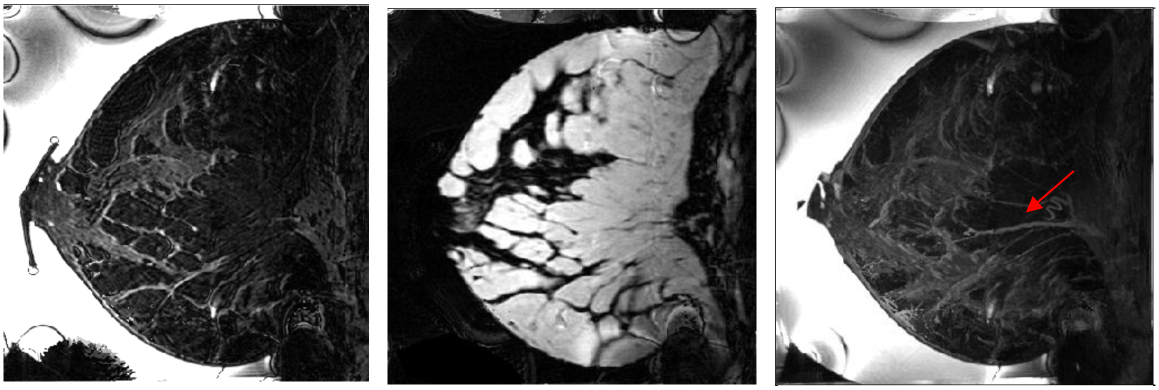
(a) (b) (c)

Figure 5.32. Two-point Dixon reconstruction based on the source images shown in Fig. 5.31, (a) water-only image, (b) fat-only image and (c) thin-slab MIP of water-only images. The bright signal in the background shown in (a) and (c) comes from water which is used for acoustic coupling. A tensioning device was attached to the nipple for stabilizing the breast.

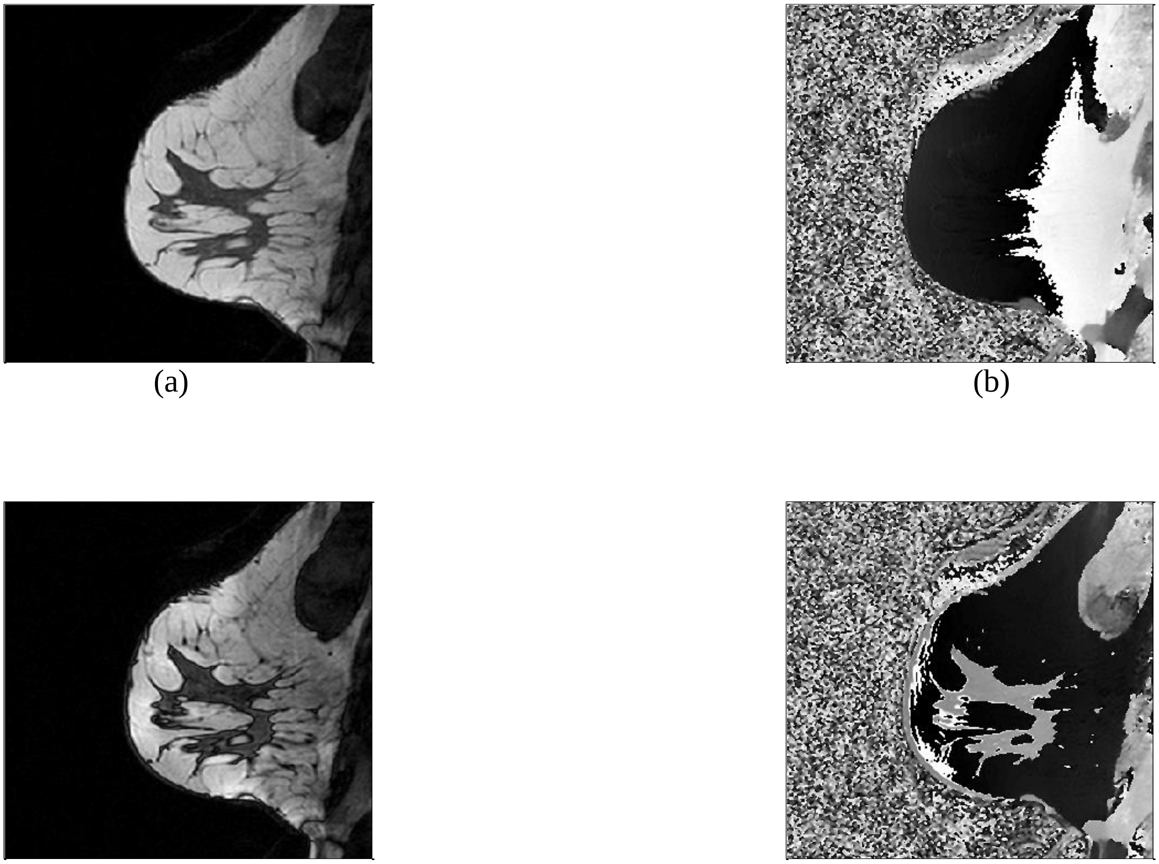
(a) (b)

(c) (d)

Figure 5.33. An example image acquired using sequence 2—3D SSFP sequence with bipolar dual-echo readout. The magnitude and phase images acquired at (a, b) TE_1 = 2.3ms and (c, d) TE_2 = 3.4ms for in-phase and out-of-phase, respectively.

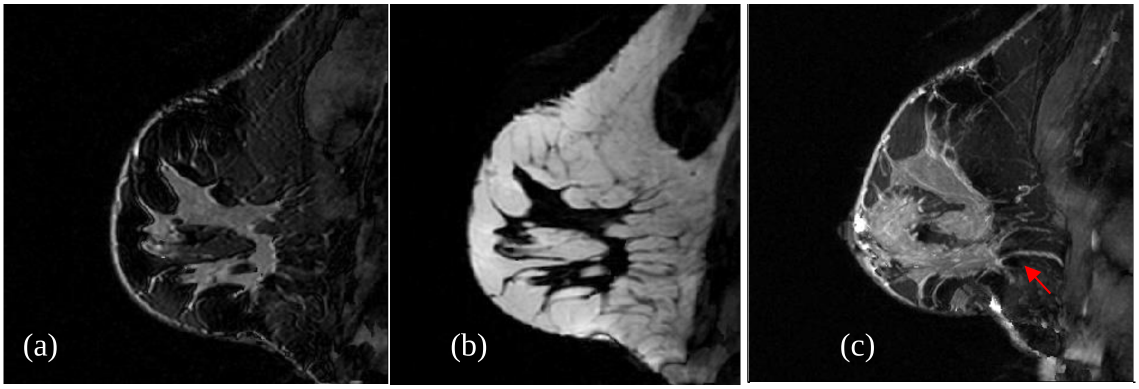

Figure 5.34. Two-point Dixon reconstruction based on the sources images shown in Fig. 5.33, (a) water-only image, (b) fat-only image, and (c) thin-slab MIP of the water-only images.

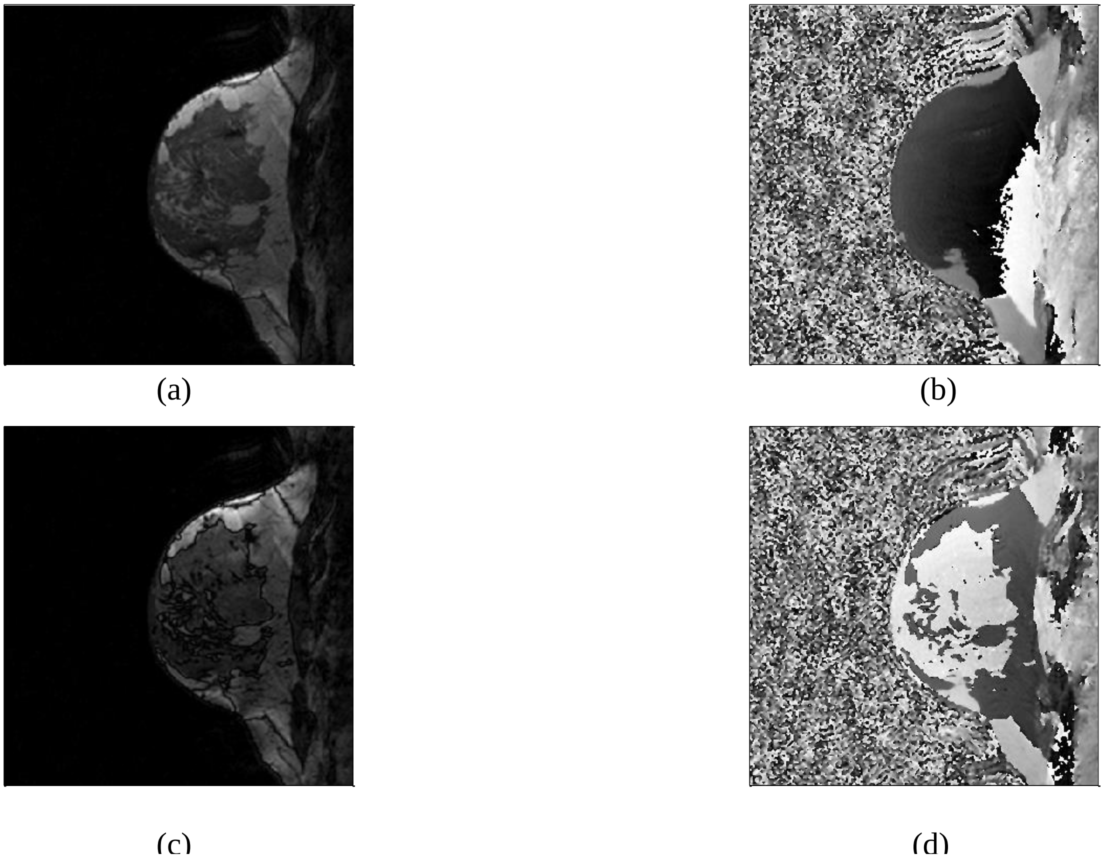
(a) (b)

(c) (d)

Figure 5.35. An example image acquired using sequence 2—3D SSFP sequence with bipolar dual-echo readout. The magnitude and phase images acquired at (a, b) $TE_1 = 2.3$ms and (c, d) $TE_2 = 3.4$ms for in-phase and out-of-phase, respectively.

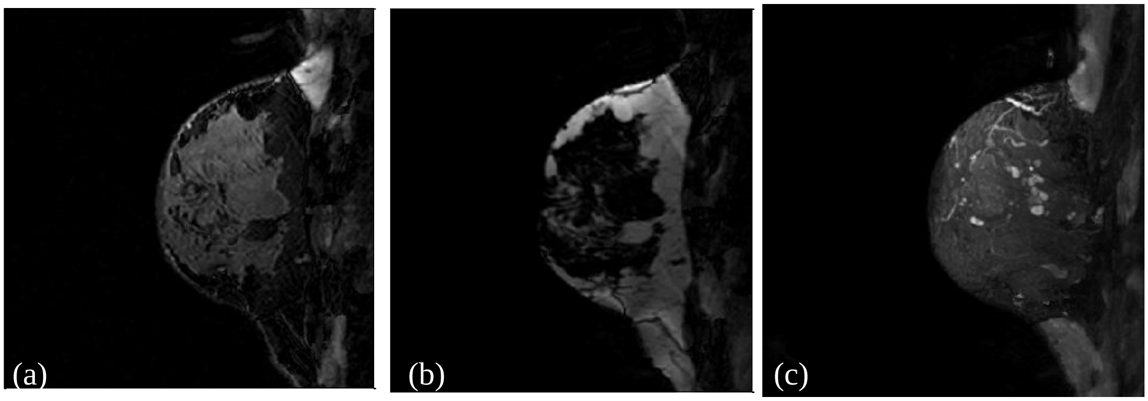

Figure 5.36. Two-point Dixon reconstruction based on the sources images shown in Fig. 5.35, (a) water-only image, (b) fat-only image, and (c) thin-slab MIP of the water-only images

CHAPTER 6

CONCLUSION

Scientific contributions

This dissertation focuses on developing advanced MRI techniques for determining tissue parameters that can assist in MRgHIFU therapy for breast cancer treatment. The identified tissue parameters — volumetric segmented tissue models, the blood vasculature and the perfusion rate — can be beneficial to various stages of the thermal therapies, including patient pretreatment planning, treatment optimization, and posttreatment evaluation.

Before initiation of an MRgHIFU therapy, it is essential to perform pretreatment planning where ultrasound beam trajectory is predicted using individual patient information. In this dissertation, the proposed hierarchical SVM-based algorithm provides 3D volumetric breast tissue models, which can then be fed to the ultrasound beam simulation to determine the optimal treatment plan for each individual patient. As part of the tissue classification workflow, the importance of multiparametric MR contrast inputs and coil sensitivity correction are demonstrated. Comparing with conventional segmentation algorithms FCM and SVM, the presented technique offers classification performance with highest accuracy. The consistency of the segmentation results along both the sagittal and axial orientations indicates the stability of the proposed segmentation routine. This suggests that the proposed algorithm could be applied for longitudinal follow-up studies to detect tissue changes, e.g., the change of breast density in breast cancer risk assessment, and posttreatment evaluation of neoadjuvant chemotherapy.

In MRgHIFU thermal therapies, local temperature distribution can be greatly influenced by the tissue-dependent property — blood perfusion. Unique MR imaging sequence designs are presented in this dissertation to visualize blood vessels and also estimate the blood perfusion rates. With these MR properties, it is possible to compensate for the dissipative effects of the flowing blood and ultimately improve the efficacy of the MRgHIFU therapies. The developed contrast-agent-free MR techniques allow multiple measurements before, during and after the treatment without the limitation of washout of the injected contrast agent.

A 3D dual-echo SSFP sequence based two-point Dixon technique is presented in this dissertation to image blood vessels in the breasts. The success of the noncontrast-enhanced breast vasculature imaging relies heavily on the suppression of the fat signal. Hence, the performances of the fat-water separation with various dual-echo readout gradient designs are evaluated on the water/oil phantom, *ex vivo* pork and *in vivo* breast. In particular, *k*-space misalignment and bidirectional chemical shift induced misregistration artifacts are discussed. As demonstrated in Chapter 5, the maximum intensity projection of the water-only images reveal details of the blood vessels that would otherwise be obscured by the bright signal from fat.

Flow quantification is achieved using an ASL magnetization-prepared turbo-

FLASH sequence with a Look-Locker-like readout scheme. Such sequence design enables estimation of the blood perfusion rates based on the time course of the perfusion-weighted signals; meanwhile, it overcomes the intrinsic low signal efficiency associated with the conventional ASL techniques. Experimental validation on the hemodialyzer indicates that the proposed pulse sequence design can be used to measure the average velocity of fluid flowing through an imaging plane. As implemented, this technique is designed to assess all flow passing through the slice, including vessels of all sizes down to capillary beds, unlike other techniques that use a pre-acquisition spoiler gradient pulse to suppress the flow signal from large vessels. By including all types of flow through the slice, the perfusion value obtained with this technique should match the perfusion term used in the Pennes' BHTE. It is possible that MRgHIFU could use measurements from this imaging technique in thermal modeling based on the Pennes' equation. Moreover, this method is independent of MR thermometry, decoupling the blood flow measurement from the MR temperature maps, allowing the perfusion changes to be monitored throughout the thermal therapy session.

Future work

The tissue classification algorithm presented in Chapter 3 provides a segmented breast tissue model composed of fat, fibroglandular tissue, skin and lesions. Because flowing blood could carry heat away from the heated volume, it would be ideal to include blood vessel as another tissue type in the model. Using the 3D dual-echo SSFP sequence proposed in Chapter 5, blood vasculature information is retrieved from the two-point Dixon reconstructed water-only images. However, the presence of fibroglandular tissue hinders the direct usage of these water-only images in the segmentation routine. In order to incorporate blood vessel in a segmented breast tissue model, suppression of the signal from the fibroglandular tissue is thus necessary. This can be achieved by applying background suppression where nonselective inversion pulses are used to null the background tissue (112).

In addition to the blood vasculature, the two-point Dixon reconstructed fat-only and water-only images can also serve as input to the tissue segmentation routine, as presented in Chapter 3. One major advantage of the two-point SSFP imaging technique over the three-point GRE-based method is its fast image acquisition speed. However, the signal loss caused by the banding artifact can lead to error in simulating the interactions of the ultrasound with tissue, due to the large difference in ultrasound attenuation between breast fat and fibroglandular tissue. This banding artifact can be reduced by combining images acquired with multiple phase cycling (111). Furthermore, the blood vessel images obtained from the dual-echo SSFP sequence need to be compared with the DCE-MRI scan for validation purposes.

Presently, the ASL flow quantification technique is only demonstrated on brain imaging. The flow assessment on the breast tissue is less successful, even though the original intention was to develop the ASL technique for the breast. This might be due to the intrinsic low perfusion rates (less than 1.5 kg/m^3/s) of the breast tissue (113). In order to improve the SNR of the perfusion-weighted signal, a pseudo-continuous ASL (pCASL) labeling strategy can be employed to achieve continuous labeling of the blood (114).

REFERENCES

1. Landis SH, Murray T, Bolden S, Wingo PA. Cancer statistics, 1999. CA Cancer J Clin 1999;49(1):8-31, 31.

2. Kaiser WA, Pfleiderer SO, Baltzer PA. MRI-guided interventions of the breast. J Magn Reson Imaging 2008;27(2):347-355.

3. Furusawa H, Namba K, Thomsen S, Akiyama F, Bendet A, Tanaka C, Yasuda Y, Nakahara H. Magnetic resonance-guided focused ultrasound surgery of breast cancer: reliability and effectiveness. J Am Coll Surg 2006;203(1):54-63.

4. Huber PE, Jenne JW, Rastert R, Simiantonakis I, Sinn HP, Strittmatter HJ, von Fournier D, Wannenmacher MF, Debus J. A new noninvasive approach in breast cancer therapy using magnetic resonance imaging-guided focused ultrasound surgery. Cancer Res 2001;61(23):8441-8447.

5. Jacobs MA, Barker PB, Bluemke DA, Maranto C, Arnold C, Herskovits EH, Bhujwalla Z. Benign and malignant breast lesions: diagnosis with multiparametric MR imaging. Radiology 2003;229(1):225-232.

6. Wang CM, Mai XX, Lin GC, Kuo CT. Classification for breast MRI using support sector machine. 2008; Washington, DC, USA. p 6.

7. Yang SC, Wang CM, Hsu HH, Chung PC, Hsu GC, Juan CJ, Lo CS. Contrast enhancement and tissues classification of breast MRI using Kalman filter-based linear mixing method. Comput Med Imaging Graph 2009;33(3):187-196.

8. Chen W, Giger ML, Bick U. A fuzzy c-means (FCM)-based approach for computerized segmentation of breast lesions in dynamic contrast-enhanced MR images. Acad Radiol 2006;13(1):63-72.

9. Nie K, Chen JH, Chan S, Chau MK, Yu HJ, Bahri S, Tseng T, Nalcioglu O, Su MY. Development of a quantitative method for analysis of breast density based on three-dimensional breast MRI. Med Phys 2008;35(12):5253-5262.

10. Dragonu I, de Oliveira PL, Laurent C, Mougenot C, Grenier N, Moonen CT, Quesson B. Non-invasive determination of tissue thermal parameters from high

intensity focused ultrasound treatment monitored by volumetric MRI thermometry. NMR Biomed 2009;22(8):843-851.

11. Hariharan P, Myers MR, Banerjee RK. HIFU procedures at moderate intensities--effect of large blood vessels. Phys Med Biol 2007;52(12):3493-3513.

12. Beaney RP, Lammertsma AA, Jones T, McKenzie CG, Halnan KE. Positron emission tomography for in-vivo measurement of regional blood flow, oxygen utilisation, and blood volume in patients with breast carcinoma. Lancet 1984;1(8369):131-134.

13. Eby PR, Partridge SC, White SW, Doot RK, Dunnwald LK, Schubert EK, Kurland BF, Lehman CD, Mankoff DA. Metabolic and vascular features of dynamic contrast-enhanced breast magnetic resonance imaging and (15)O-water positron emission tomography blood flow in breast cancer. Acad Radiol 2008;15(10):1246-1254.

14. Niklason LT, Kopans DB, Hamberg LM. Digital breast imaging: tomosynthesis and digital subtraction mammography. Breast Dis 1998;10(3-4):151-164.

15. Furman-Haran E, Schechtman E, Kelcz F, Kirshenbaum K, Degani H. Magnetic resonance imaging reveals functional diversity of the vasculature in benign and malignant breast lesions. Cancer 2005;104(4):708-718.

16. Wu F, Chen WZ, Bai J, Zou JZ, Wang ZL, Zhu H, Wang ZB. Tumor vessel destruction resulting from high-intensity focused ultrasound in patients with solid malignancies. Ultrasound Med Biol 2002;28(4):535-542.

17. Wang Y, Morrell G, Heibrun ME, Payne A, Parker DL. 3D multi-parametric breast MRI segmentation using hierarchical support vector machine with coil sensitivity correction. Acad Radiol 2013;20(2):137-147.

18. Gunther M, Bock M, Schad LR. Arterial spin labeling in combination with a look-locker sampling strategy: inflow turbo-sampling EPI-FAIR (ITS-FAIR). Magn Reson Med 2001;46(5):974-984.

19. Wang Y, Kim SE, Parker DL. High resolution 3D MR angiography using arterial spin labeling. 2009; Honolulu, Hawaii. p 94.

20. Wang Y, Kim SE, DiBella EV, Parker DL. Flow measurement in MRI using arterial spin labeling with cumulative readout pulses--theory and validation. Med Phys 2010;37(11):5801-5810.

21. Wang Y, Minalga E, Payne A, Morrell G, Parker DL. Two-point Dixon fat and water separation using dual-echo SSFP sequence in breast imaging. 2012; Melbourne, Australia. p 4167.

22. Purcell EM, Torrey HC, Pound RV. Resonance absorption by nuclear magnetic moments in a solid. Phys Rev 1946;69(1-2):37-38.

23. Bloch F, Hansen WW, Packard M. Nuclear induction. Phys Rev 1946;69(3-4):127-127.

24. Lauterbur PC. Image formation by induced local interactions. Examples employing nuclear magnetic resonance. 1973. Clin Orthop Relat Res 1989(244):3-6.

25. Kumar A, Welti D, Ernst RR. NMR Fourier zeugmatography. 1975. J Magn Reson 2011;213(2):495-509.

26. Haccke EM, Brown RW, Thompson MR, Venkatesan R. Magnetic resonance imaging: physical principles and sequence design. New York: Wiley-Liss; 1999.

27. Bernstein MA, King KF, Zhou ZJ. Handbook of MRI pulse sequences. Amsterdam; Boston: Academic Press; 2004.

28. Bloch F. Nuclear induction. Phys Rev 1946;70(7-8):460-474.

29. Vlaardingerbroek MT, den Boer KA. Magnetic resonance imaging: theory and Practice. Berlin: Springer-Verlag; 1996.

30. Zur Y, Stokar S, Bendel P. An analysis of fast imaging sequences with steady-state transverse magnetization refocusing. Magn Reson Med 1988;6(2):175-193.

31. Detre JA, Wang J, Wang Z, Rao H. Arterial spin-labeled perfusion MRI in basic and clinical neuroscience. Curr Opin Neurol 2009;22(4):348-355.

32. Williams DS, Detre JA, Leigh JS, Koretsky AP. Magnetic resonance imaging of perfusion using spin inversion of arterial water. Proc Natl Acad Sci U S A 1992;89(1):212-216.

33. Liu TT, Brown GG. Measurement of cerebral perfusion with arterial spin labeling: Part 1. Methods. J Int Neuropsychol Soc 2007;13(3):517-525.

34. Sinha S, Sinha U. Recent advances in breast MRI and MRS. NMR Biomed 2009;22(1):3-16.

35. Weatherall PT, Evans GF, Metzger GJ, Saborrian MH, Leitch AM. MRI vs. histologic measurement of breast cancer following chemotherapy: comparison with x-ray mammography and palpation. J Magn Reson Imaging 2001;13(6):868-875.

36. Lee NA, Rusinek H, Weinreb J, Chandra R, Toth H, Singer C, Newstead G. Fatty and fibroglandular tissue volumes in the breasts of women 20-83 years old: comparison of X-ray mammography and computer-assisted MR imaging. AJR Am J Roentgenol 1997;168(2):501-506.

37. Bhooshan N, Giger ML, Jansen SA, Li H, Lan L, Newstead GM. Cancerous breast lesions on dynamic contrast-enhanced MR images: computerized characterization for image-based prognostic markers. Radiology 2010;254(3):680-690.

38. Ertas G, Gulcur HO, Osman O, Ucan ON, Tunaci M, Dursun M. Breast MR segmentation and lesion detection with cellular neural networks and 3D template matching. Comput Biol Med 2008;38(1):116-126.

39. Ertas G, Gulcur HO, Tunaci M. Improved lesion detection in MR mammography: three-dimensional segmentation, moving voxel sampling, and normalized maximum intensity-time ratio entropy. Acad Radiol 2007;14(2):151-161.

40. Gilhuijs KG, Giger ML, Bick U. Computerized analysis of breast lesions in three dimensions using dynamic magnetic-resonance imaging. Med Phys 1998;25(9):1647-1654.

41. Nie K, Chen JH, Yu HJ, Chu Y, Nalcioglu O, Su MY. Quantitative analysis of lesion morphology and texture features for diagnostic prediction in breast MRI. Acad Radiol 2008;15(12):1513-1525.

42. Nie K, Chen JH, Chan S, Chau MK, Yu HJ, Bahri S, Tseng T, Nalcioglu O, Su MY. Development of a quantitative method for analysis of breast density based on three-dimensional breast MRI. Med Phys 2008;35(12):5253-5262.

43. Lin M, Chan S, Chen JH, Chang D, Nie K, Chen ST, Lin CJ, Shih TC, Nalcioglu O, Su MY. A new bias field correction method combining N3 and FCM for improved segmentation of breast density on MRI. Med Phys 2011;38(1):5-14.

44. Wang CM, Mai XX, Lin GC, Kuo CT. Classification for breast MRI using support sector machine. Proceedings of the 2008 IEEE 8th International Conference on Computer and Information Technology 2008:362-367.

45. Heywang SH, Bassermann R, Fenzl G, Nathrath W, Hahn D, Beck R, Krischke I, Eiermann W. MRI of the breast--histopathologic correlation. Eur J Radiol 1987;7(3):175-182.

46. Meyer CR, Bland PH, Pipe J. Retrospective correction of intensity inhomogeneities in MRI. IEEE Trans Med Imaging 1995;14(1):36-41.

47. Guillemaud R, Brady M. Estimating the bias field of MR images. IEEE Trans Med Imaging 1997;16(3):238-251.

48. Brey WW, Narayana PA. Correction for intensity falloff in surface coil magnetic resonance imaging. Med Phys 1988;15(2):241-245.

49. McVeigh ER, Bronskill MJ, Henkelman RM. Phase and sensitivity of receiver coils in magnetic resonance imaging. Med Phys 1986;13(6):806-814.

50. Bezdek JC. Pattern recognition with fuzzy objective function algorithms. New York: Plenum Press; 1981. xv, 256 p. p.

51. Chen W, Giger ML, Bick U. A fuzzy c-means (FCM)-based approach for computerized segmentation of breast lesions in dynamic contrast-enhanced MR images. Acad Radiol 2006;13(1):63-72.

52. Barck KH, Willis B, Ross J, French DM, Filvaroff EH, Carano RA. Viable tumor tissue detection in murine metastatic breast cancer by whole-body MRI and multispectral analysis. Magn Reson Med 2009;62(6):1423-1430.

53. Yang SC, Wang CM, Hsu HH, Chung PC, Hsu GC, Juan CJ, Lo CS. Contrast enhancement and tissues classification of breast MRI using Kalman filter-based linear mixing method. Comput Med Imaging Graph 2009;33(3):187-196.

54. Chung PC, Wang CM, Yang SH, Hsu HH. Tissues classification for breast MRI contrast enhancement using spectral signature detection approach. IEEE International Conference on Systems, Man and Cybernetics 2006:3917-3921.

55. Du YP, Parker DL, Davis WL, Cao G. Reduction of partial-volume artifacts with zero-filled interpolation in three-dimensional MR angiography. J Magn Reson Imaging 1994;4(5):733-741.

56. Glover GH, Schneider E. Three-point Dixon technique for true water/fat decomposition with B0 inhomogeneity correction. Magn Reson Med 1991;18(2):371-383.

57. Bernstein MA, King KF, Zhou ZJ. Handbook of MRI pulse sequences. Amsterdam; Boston: Academic Press; 2004. xxii,1017.

58. Moon-Ho Song S, Napel S, Pelc NJ, Glover GH. Phase unwrapping of MR phase images using Poisson equation. IEEE Trans Image Process 1995;4(5):667-676.

59. Nie K, Chang D, Chen JH, Shih TC, Hsu CC, Nalcioglu O, Su MY. Impact of skin removal on quantitative measurement of breast density using MRI. Med Phys 2010;37(1):227-233.

60. Canny J. A computational approach to edge detection. IEEE Trans Pattern Anal Mach Intell 1986;8(6):679-698.

61. Vemuri P, Kholmovski EG, Parker DL, Chapman BE. Coil sensitivity estimation for optimal SNR reconstruction and intensity inhomogeneity correction in phased array MR imaging. Inf Process Med Imaging 2005;19:603-614.

62. Roemer PB, Edelstein WA, Hayes CE, Souza SP, Mueller OM. The NMR phased array. Magn Reson Med 1990;16(2):192-225.

63. Cortes C, Vapnik V. Support-vector networks. Machine Learning 1995;20(3):273-297.

64. Chang CC, Lin CJ. LIBSVM: a library for support vector machine. ACM Transactions on Intelligent Systems and Technology 2011;2(27):1-27.

65. Casasent D, Wang YC. A hierarchical classifier using new support vector machines for automatic target recognition. Neural Netw 2005;18(5-6):541-548.

66. Williams DS, Detre JA, Leigh JS, Koretsky AP. Magnetic resonance imaging of perfusion using spin inversion of arterial water. Proc Natl Acad Sci U S A 1992;89(1):212-216.

67. Song CW, Rhee JG, Levitt SH. Blood flow in normal tissues and tumors during hyperthermia. J Natl Cancer Inst 1980;64(1):119-124.

68. Wu F, Chen WZ, Bai J, Zou JZ, Wang ZL, Zhu H, Wang ZB. Tumor vessel destruction resulting from high-intensity focused ultrasound in patients with solid malignancies. Ultrasound Med Biol 2002;28(4):535-542.

69. Detre JA, Leigh JS, Williams DS, Koretsky AP. Perfusion imaging. Magn Reson Med 1992;23(1):37-45.

70. Buxton RB, Frank LR, Wong EC, Siewert B, Warach S, Edelman RR. A general kinetic model for quantitative perfusion imaging with arterial spin labeling. Magn Reson Med 1998;40(3):383-396.

71. Edelman RR, Chen Q. EPISTAR MRI: multislice mapping of cerebral blood flow. Magn Reson Med 1998;40(6):800-805.

72. Edelman RR, Siewert B, Darby DG, Thangaraj V, Nobre AC, Mesulam MM, Warach S. Qualitative mapping of cerebral blood flow and functional localization with echo-planar MR imaging and signal targeting with alternating radio frequency. Radiology 1994;192(2):513-520.

73. Golay X, Stuber M, Pruessmann KP, Meier D, Boesiger P. Transfer insensitive labeling technique (TILT): application to multislice functional perfusion imaging. J Magn Reson Imaging 1999;9(3):454-461.

74. Wong EC, Buxton RB, Frank LR. Quantitative imaging of perfusion using a single subtraction (QUIPSS and QUIPSS II). Magn Reson Med 1998;39(5):702-708.

75. Kim SG. Quantification of relative cerebral blood flow change by flow-sensitive alternating inversion recovery (FAIR) technique: application to functional mapping. Magn Reson Med 1995;34(3):293-301.

76. Helpern JA, Branch CA, Yongbi MN, Huang NC. Perfusion imaging by un-inverted flow-sensitive alternating inversion recovery (UNFAIR). Magn Reson Imaging 1997;15(2):135-139.

77. Jahng GH, Weiner MW, Schuff N. Improved arterial spin labeling method: applications for measurements of cerebral blood flow in human brain at high magnetic field MRI. Med Phys 2007;34(11):4519-4525.

78. Gunther M, Bock M, Schad LR. Arterial spin labeling in combination with a look-locker sampling strategy: inflow turbo-sampling EPI-FAIR (ITS-FAIR). Magn Reson Med 2001;46(5):974-984.

79. Petersen ET, Lim T, Golay X. Model-free arterial spin labeling quantification approach for perfusion MRI. Magn Reson Med 2006;55(2):219-232.

80. Miyazaki M, Lee VS. Nonenhanced MR angiography. Radiology 2008;248(1):20-43.

81. Pell GS, Lewis DP, Ordidge RJ, Branch CA. TurboFLASH FAIR imaging with optimized inversion and imaging profiles. Magn Reson Med 2004;51(1):46-54.

82. Prasad PV, Kim D, Kaiser AM, Chavez D, Gladstone S, Li W, Buxton RB, Edelman RR. Noninvasive comprehensive characterization of renal artery stenosis by combination of STAR angiography and EPISTAR perfusion imaging. Magn Reson Med 1997;38(5):776-787.

83. Zhu DC, Buonocore MH. Breast tissue differentiation using arterial spin tagging. Magn Reson Med 2003;50(5):966-975.

84. Cavusoglu M, Pfeuffer J, Ugurbil K, Uludag K. Comparison of pulsed arterial spin labeling encoding schemes and absolute perfusion quantification. Magn Reson Imaging 2009;27(8):1039-1045.

85. Barbier EL, Silva AC, Kim SG, Koretsky AP. Perfusion imaging using dynamic arterial spin labeling (DASL). Magn Reson Med 2001;45(6):1021-1029.

86. Reeder SB, Atalay MK, McVeigh ER, Zerhouni EA, Forder JR. Quantitative cardiac perfusion: a noninvasive spin-labeling method that exploits coronary vessel geometry. Radiology 1996;200(1):177-184.

87. Mai VM, Hagspiel KD, Altes T, Goode AR, Williams MB, Berr SS. Detection of regional pulmonary perfusion deficit of the occluded lung using arterial spin labeling in magnetic resonance imaging. J Magn Reson Imaging 2000;11(2):97-102.

88. Roberts DA, Detre JA, Bolinger L, Insko EK, Lenkinski RE, Pentecost MJ, Leigh JS, Jr. Renal perfusion in humans: MR imaging with spin tagging of arterial water. Radiology 1995;196(1):281-286.

89. Noguchi T, Yoshiura T, Hiwatashi A, Togao O, Yamashita K, Kobayashi K, Mihara F, Honda H. Quantitative perfusion imaging with pulsed arterial spin labeling: a phantom study. Magn Reson Med Sci 2007;6(2):91-97.

90. Levy C, Laissy JP, Raveau V, Amarenco P, Servois V, Bousser MG, Tubiana JM. Carotid and vertebral artery dissections: three-dimensional time-of-flight MR angiography and MR imaging versus conventional angiography. Radiology 1994;190(1):97-103.

91. Gupta A, Frazer CK, Ferguson JM, Kumar AB, Davis SJ, Fallon MJ, Morris IT, Drury PJ, Cala LA. Acute pulmonary embolism: diagnosis with MR angiography. Radiology 1999;210(2):353-359.

92. Sardanelli F, Iozzelli A, Fausto A, Carriero A, Kirchin MA. Gadobenate dimeglumine-enhanced MR imaging breast vascular maps: association between invasive cancer and ipsilateral increased vascularity. Radiology 2005;235(3):791-797.

93. Grubstein A, Yepes M, Kiszonas R. Magnetic resonance imaging of breast vascularity in medial versus lateral breast cancer. Eur J Radiol 2010;75(2):e9-11.

94. Miyazaki M, Otto PM, Kanazawa H, Ichinose N, Sugiura S, Anderson R. Nonenhanced 3D breast MRA using FBI and time-SLIP. 2009; Honolulu, Hawaii. p 1.

95. Saranathan M, Bayram E, Lee C. Ultrafast near-isotropic spatial resolution 3D balanced-SSFP Dixon imaging in the breast. 2010; Stockholm, Sweden. p 4167.

96. Kuhl CK, Mielcareck P, Klaschik S, Leutner C, Wardelmann E, Gieseke J, Schild HH. Dynamic breast MR imaging: are signal intensity time course data useful for differential diagnosis of enhancing lesions? Radiology 1999;211(1):101-110.

97. Ersoy H, Rybicki FJ. MR angiography of the lower extremities. AJR Am J Roentgenol 2008;190(6):1675-1684.

98. Bangerter NK, Cukur T, Hargreaves BA, Hu BS, Brittain JH, Park D, Gold GE, Nishimura DG. Three-dimensional fluid-suppressed T2-prep flow-independent peripheral angiography using balanced SSFP. Magn Reson Imaging 2011;29(8):1119-1124.

99. Cukur T, Shimakawa A, Yu H, Hargreaves BA, Hu BS, Nishimura DG, Brittain JH. Magnetization-prepared IDEAL bSSFP: a flow-independent technique for noncontrast-enhanced peripheral angiography. J Magn Reson Imaging 2011;33(4):931-939.

100. Coombs BD, Szumowski J, Coshow W. Two-point Dixon technique for water-fat signal decomposition with B0 inhomogeneity correction. Magn Reson Med 1997;38(6):884-889.

101. Dixon WT. Simple proton spectroscopic imaging. Radiology 1984;153(1):189-194.

102. Glover GH, Schneider E. Three-point Dixon technique for true water/fat decomposition with B0 inhomogeneity correction. Magn Reson Med 1991;18(2):371-383.

103. Ma X, Holalkere NS, Kambadakone RA, Mino-Kenudson M, Hahn PF, Sahani DV. Imaging-based quantification of hepatic fat: methods and clinical applications. Radiographics 2009;29(5):1253-1277.

104. Moon-Ho Song S, Napel S, Pelc NJ, Glover GH. Phase unwrapping of MR phase images using Poisson equation. IEEE Trans Image Process 1995;4(5):667-676.

105. Lu W, Yu H, Shimakawa A, Alley M, Reeder SB, Hargreaves BA. Water-fat separation with bipolar multiecho sequences. Magn Reson Med 2008;60(1):198-209.

106. Li Z, Gmitro AF, Bilgin A, Altbach MI. Fast decomposition of water and lipid using a GRASE technique with the IDEAL algorithm. Magn Reson Med 2007;57(6):1047-1057.

107. Edden RA, Smith SA, Barker PB. Longitudinal and multi-echo transverse relaxation times of normal breast tissue at 3 Tesla. J Magn Reson Imaging 2010;32(4):982-987.

108. Minalga ES, Payne A, Morrill R, Dennis LP, Hadley R. Design & evaluation of RF coils for magnetic resonance guided high intensity focused ultrasound. 2011; Montreal, Canada. p 1.

109. Payne A, Merrill R, Minalga E, Vyas U, de Bever J, Todd N, Hadley R, Dumont E, Neumayer L, Christensen D, Roemer R, Parker D. Design and characterization of a laterally mounted phased-array transducer breast-specific MRgHIFU device with integrated 11-channel receiver array. Med Phys 2012;39(3):1552-1560.

110. Reeder SB, Wen Z, Yu H, Pineda AR, Gold GE, Markl M, Pelc NJ. Multicoil Dixon chemical species separation with an iterative least-squares estimation method. Magn Reson Med 2004;51(1):35-45.

111. Bangerter NK, Hargreaves BA, Vasanawala SS, Pauly JM, Gold GE, Nishimura DG. Analysis of multiple-acquisition SSFP. Magn Reson Med 2004;51(5):1038-1047.

112. Mani S, Pauly J, Conolly S, Meyer C, Nishimura D. Background suppression with multiple inversion recovery nulling: applications to projective angiography. Magn Reson Med 1997;37(6):898-905.

113. Mahoney K, Fjield T, McDannold N, Clement G, Hynynen K. Comparison of modelled and observed in vivo temperature elevations induced by focused ultrasound: implications for treatment planning. Phys Med Biol 2001;46(7):1785-1798.

114. Dai W, Garcia D, de Bazelaire C, Alsop DC. Continuous flow-driven inversion for arterial spin labeling using pulsed radio frequency and gradient fields. Magn Reson Med 2008;60(6):1488-1497.